

Phase-Resolved Imaging of Exciton Polaritons

THÈSE N° 5002 (2011)

PRÉSENTÉE LE 1^{ER} AVRIL 2011
À LA FACULTÉ SCIENCES DE BASE
LABORATOIRE D'OPTOÉLECTRONIQUE QUANTIQUE
PROGRAMME DOCTORAL EN PHOTONIQUE

ÉCOLE POLYTECHNIQUE FÉDÉRALE DE LAUSANNE

POUR L'OBTENTION DU GRADE DE DOCTEUR ÈS SCIENCES

PAR

Gaël NARDIN

acceptée sur proposition du jury:

Prof. O. Martin, président du jury
Prof. B. Deveaud-Plédran, directeur de thèse
Prof. C. Ciuti, rapporteur
Prof. S. Cundiff, rapporteur
Prof. J. Faist, rapporteur



ÉCOLE POLYTECHNIQUE
FÉDÉRALE DE LAUSANNE

Suisse
2011

Abstract

In this PhD thesis, new imaging techniques have been developed in order to explore the physics of semiconductor microcavities. In these structures, composite bosons called exciton polaritons are the result of strong coupling between the cavity mode and quantum well excitons. A spectroscopic imaging technique has been developed to image the eigenstates of polaritons confined in the traps of a patterned GaAs microcavity. Polariton probability densities have been reconstructed in three dimensions - two spatial dimensions and energy - allowing to retrieve two-dimensional probability density mappings of the eigenstates. In order to image the wave functions (and not the probability densities only), a phase-resolved imaging setup has been built. Interfering the near field or far field of the polariton emission with a reference laser beam allowed to retrieve the full information (amplitude and phase) of the polariton wave functions. This tool allowed to evidence the effect of trap ellipticity on the confined polariton wave functions. Polariton vortices were also identified as a superposition of eigenmodes of the elliptical traps, and a selective excitation method has been used to optically control the sign and value of the vortex charge. Combining phase-resolved imaging with ultrafast optics allowed to probe the time evolution of coherent superpositions of confined polariton states. In particular, Rabi oscillations between vortex and anti-vortex states have been observed. Eventually, the time and phase resolved imaging tools have been used to explore the physics of quantum fluids. The scattering of polariton wave packets on a structural defect has been studied. Different flow regimes have been identified, and, in particular, quantum turbulence has been observed in the form of quantized vortices nucleating in the wake of the defect. The nucleation conditions have been established in terms of local fluid velocity and density on the obstacle perimeter. The results were successfully reproduced by numerical simulations based on generalized Gross-Pitaevskii equations.

Keywords: III-V semiconductors, microcavities, polaritons, excitons, photoluminescence, quantum confinement, quantum optics, quantum fluids, ultra-fast optics, turbulence, non-equilibrium, vortices, digital holography, Bose gases, superfluidity

Résumé

Dans cette thèse de doctorat, de nouvelles techniques d'imagerie ont été développées afin d'explorer la physique des microcavités semiconductrices. Dans ces structures, des bosons composites, appelés polaritons excitoniques, sont le résultat du couplage fort entre le mode de cavité et les excitons de puits quantique. Une technique de spectroscopie résolue spatialement a été développée pour imager les états propres de polaritons confinés dans les pièges d'une microcavité en arsenure de gallium spécifiquement nanostructurée. Les densités de probabilité des polaritons ont été reconstruites en trois dimensions - en deux dimensions spatiales et en énergie - permettant d'extraire les images des densités de probabilités des états propres. Afin de pouvoir imager la fonction d'onde elle-même, et pas uniquement son carré, une expérience d'imagerie résolue en phase a été mise au point. En faisant interférer l'émission des polaritons avec un faisceau laser de référence dans le plan image ou le plan de Fourier, nous avons pu extraire l'information complète (amplitude et phase) de la fonction d'onde des polaritons. Cet outil a permis de mettre en évidence les effets de l'ellipticité des pièges sur la fonction d'onde des polaritons confinés. Des vortex de polaritons ont aussi été identifiés comme la superposition des états propres du piège elliptique. Une méthode d'excitation sélective a été utilisée pour contrôler optiquement le signe et la valeur de la charge topologique du vortex. En combinant l'imagerie résolue en phase et des impulsions optiques ultra-courtes, l'évolution temporelle d'une superposition cohérente d'état polaritoniques confinés a pu être sondée. En particulier, des oscillations de Rabi entre des états de vortex et d'anti-vortex ont été observées. Finalement, les outils d'imagerie résolus en temps et en phase ont été utilisés pour étudier la physique des fluides quantiques. La diffusion d'un paquet d'onde de polaritons sur un défaut structurel a été investiguée. Différents régimes d'écoulement ont été identifiés, et, en particulier, des turbulences quantiques ont été observées sous la forme de vortex quantifiés se formant dans le sillage du défaut. Les conditions de formation des vortex ont été établies en termes de vitesse et densité locale du fluide sur le périmètre de l'obstacle. Les résultats ont pu être reproduits avec succès par des simulations numériques basées sur les équations de Gross-Pitaevskii généralisées.

Mots-clés: semiconducteurs III-V, microcavités, polaritons, excitons, photoluminescence, confinement quantique, optique quantique, fluides quantiques, optique ultra-rapide, turbulences, systèmes hors-équilibre, vortex, holographie digitale, gaz de bosons, superfluidité

Contents

Introduction	1
Units	5
I Background: Physics of semiconductor microcavities	7
1 Exciton polaritons	9
1.1 Excitons in semiconductors	9
1.2 Semiconductor microcavities	10
1.3 Strong light-matter coupling in microcavities	13
1.4 Polaritonic nonlinearities	16
1.5 Generalized Gross-Pitaevskii equations	16
2 Polaritonic confinement in a patterned microcavity	19
2.1 Confining exciton polaritons	19
2.2 Sample: a patterned microcavity	20
II Spectroscopy and imaging of confined polaritons	25
3 Probability density tomography of confined polaritons	27
3.1 Motivations	27
3.2 Imaging spectroscopy setup	27
3.3 Tomography in quasi-cylindrical traps	29
3.4 Fourier space tomography	36
3.5 Tomography in exotic structures	37
3.6 Conclusion	40
4 Phase-resolved imaging of polariton states	43
4.1 Motivations	43
4.2 Phase-resolved imaging setup	43
4.3 Imaging the wavefunctions in elliptical traps	45
4.4 Mathieu equations and functions	50
4.5 Conclusion	53

5	Selective excitation of confined polariton vortices	55
5.1	Motivations	55
5.2	Poincaré sphere representation of the degenerate state	55
5.3	Excitation of vortex states	57
5.4	Higher angular orbital momentum states	59
5.5	Vortex non-linearities	60
5.6	Conclusion	61
6	Oscillations between vortex and anti-vortex states	63
6.1	Motivations	63
6.2	Time resolved homodyne imaging setup	63
6.3	Oscillations between vortex and anti-vortex states	65
6.4	Conclusion	66
III	Polariton fluid dynamics	69
7	Quantum Turbulence in a polariton fluid	71
7.1	Motivations	71
7.2	Framework	72
7.3	Setup and experimental conditions	76
7.4	Preliminary data: Time-integrated measurements	79
7.5	Population dynamics	81
7.6	Spatial dynamics	82
7.7	Determining experimental conditions for vortex nucleation	88
7.8	Numerical simulations based on the Gross-Pitaevskii equations	90
7.9	Towards Bénard-von Karman streets and full turbulence: preliminary results	95
7.10	Conclusion	96
IV	Perspectives	97
8	Experiment Proposals	99
8.1	Spatially resolved spectroscopy	99
8.2	Quantum fluidics...	100
8.3	Quantum optics	101
8.4	Miscellaneous	102
9	New sample design and fabrication	105
9.1	General design: comment on the number of quantum wells	105
9.2	Fabrication of the sample	107
	Conclusion	113

Introduction

For almost two decades, semiconductor microcavities in the strong light matter coupling regime have been attracting an ever growing interest. These structures, are rather simply described, though: two semiconductor distributed Bragg reflectors (DBR) sandwiching an active layer made of one or several quantum wells (QW). Nevertheless, since the first measurement of the normal mode splitting between the excitonic resonance of the QW and a GaAs-based microcavity optical mode by C. Weisbuch *et al.* [1] in 1992, thousands of publications have explored the extremely rich physics of these hybrid light matter waves.

The eigenmodes of the system, the *exciton polaritons* (also called *microcavity polaritons*, in order to differentiate them from bulk exciton polaritons) are indeed a very peculiar mixture¹. Partly excitonic, partly photonic, these two-dimensional quasi-particles are gathering advantages of their two components. From their light part, and a one-to-one coupling to the extra-cavity field, with conservation of in-plane momentum, energy and phase [2], exciton polaritons can be easily optically injected, manipulated, and detected. They also inherit the very small effective mass of the cavity photon. Through their excitonic part, polaritons can interact with each other, opening the way to non-linear and parametric processes. Eventually, exciton polaritons are composite bosons, as long as their excitonic oscillator strength is not screened.

The first demonstration of the potential of polaritons came with the parametric amplifier [3, 4, 5], which exploited at the same time the polariton-polariton interaction for scattering from a pump state into a pair of signal and idler state, and the bosonic stimulation to spectacularly amplify a weak probe pulse resonant with the signal state. This kind of experiment allowed to evidence quantum degeneracy with up to 10^5 polariton in the signal state. The strong non-linearities inherited from the exciton component were also exploited to evidence optical bistability, under resonant optical excitation of the polariton modes [6].

Under non-resonant excitation (i.e. creating hot electron-hole pairs above the photonic band gap of the DBR), several works reported stimulated relaxation mechanisms towards the bottom of the polariton dispersion [7, 8]. In 2006, stimulated relaxation towards the macroscopically occupied lowest energy state was shown to be accompanied with the appearance of long range order within the polariton gas in a CdTe microcavity [9], allowing to identify the process as a phase transition to a non-equilibrium Bose-Einstein condensate (BEC). This phase transition differs

¹The fact that light and matter can no longer be considered as separated entities would certainly be of interest for philosophers as well, but the philosophical aspect of the strong light matter coupling is not treated in the present work

from atomic condensates by its non-equilibrium nature: the coupling of cavity polaritons with extra-cavity photons yielding to a polariton lifetime of the order of $10ps$, the condensate needs to be constantly replenished by the laser pump. The other main difference, which is a major experimental advantage, comes from the very small polariton effective mass, allowing for the phase transition to be observed at cryogenic temperatures. Numerous interesting works have followed the demonstration of polariton BEC, like the observation of quantized vortices in the condensed phase [10, 11], or the demonstration of spontaneous coherent oscillations in coupled polariton condensates [12].

Beside these works under non-resonant excitation, where the coherence of the condensed phase spontaneously appears with the phase transition, it has been shown that coherent macroscopic polariton populations can be injected using a resonant laser field [13]. If the coherence of the quantum degenerate state is in this case inherited from the driving field, the created polariton gas can nevertheless be treated as a coherently driven weakly interacting boson gas, and described in the framework of Gross-Pitaevskii equations (GPE) [14]. The coherent polariton gas, formally similar to an atomic BEC (except for its two-dimensional geometry and its non-equilibrium properties), is thus an ideal tool for the study of quantum fluids effects such as superfluidity [15]. Far from being a drawback, the non-equilibrium nature of the polariton gas not only provides a direct optical access to the polariton field, but also yields to a very rich and unexplored physics. The recent demonstration of superfluidity and Čerenkov-like radiations in a polariton fluid [16] showed the enormous potential of polaritons for fundamental physics experiments.

On the side of applications, theoretical works have proposed to use polaritons for the generation of single photons [17, 18], or for new kind of logical elements exploiting the polarization (or spin) degree of freedom of the polariton field [19, 20]. These proposals require particular lateral confinement shapes and sizes. The most established technique for the lateral confinement of polaritons is the etching of micropillars [21], which led to the demonstration of polariton lasing [22]. An alternative confinement mechanism using shallow mesas has been developed in our group [23]. The high quality of the confinement in these structures led to the recent demonstration of spinor multistability and efficient spin switches [24], a required building block for subsequent optical memory devices.

All the experiments performed in GaAs or CdTe based microcavities must be conducted at cryogenic temperatures, as the exciton binding energy E_B is in the order of $10meV$ in GaAs [25], and $25meV$ in CdTe [26], to be compared to the thermal energy $k_B T$ at room temperature ($\sim 25meV$) and liquid helium temperature ($\sim 0.5meV$). If cryogenic temperatures are much more comfortable than the nanokelvins required for atomic BEC, they hinder the implementation of practical devices, though. The development of high exciton binding energy materials holds therefore great promises for the practical implementation of polaritonic devices. Let us mention in this respect microcavities based on GaN ($E_B \sim 40meV$) [27], ZnO ($E_B \sim 60meV$) [28, 29] or organic materials ($E_B \sim 0.2 - 0.5eV$) [30, 31]. Moreover, these materials feature a large exciton oscillator strength, which is essential for the robustness of the strong coupling regime. Eventually, let us also mention that incoherent pumping has recently been demonstrated by means of electrical injection

[32, 33, 34], which is an other step towards practical applications.

The central theme of this thesis is the imaging of exciton polaritons. Various spectroscopic and imaging techniques allow to explore several aspects of the physics of polaritons.

- Part I of the manuscript is an introductory part. In Chapter 1 we review the basics of the physics of semiconductor microcavities. In Chapter 2, we describe the confinement of polaritons in patterned microcavities, and present the sample which is used in the experiments of this thesis.
- In Part II, we present several experiments involving spectroscopy and phase-resolved imaging in order to characterize and manipulate the polariton modes confined in the traps of a patterned microcavity. In Chapter 3 we show a spatially resolved spectroscopy method which allows to fully characterize the distribution of polariton modes in traps of different sizes and shapes. In Chapter 4, it is demonstrated how the eigenstates of elliptical traps can be selectively excited using a resonant laser field. Phase-resolved images of their emission patterns are successively compared to the analytical solutions of the Helmholtz equation on an elliptical domain. In Chapter 5, it is shown how the driving laser field can be tuned to selectively excite different types of superpositions of the trap eigenstates. In particular, the excitation of integer orbital angular momentum states (or vortices) is demonstrated, with control over the vortex topological charge. In Chapter 6 we present a time and phase resolved imaging setup, and use it to image the free evolution of a coherent superposition of confined polariton states on a picosecond time scale. The observed dynamics features an oscillation between vortex and anti-vortex states, remarkably well described within the Poincaré sphere representation of a state containing orbital angular momentum.
- In Part III, we address the physics of quantum fluids by studying the propagation of a polariton wavepacket in the microcavity plane. Using our time and phase resolved imaging setup we probe the scattering of the polariton wavepacket on an obstacle, for several wavepacket velocities and densities. Several flow regime are characterized, and, in particular, the hydrodynamic nucleation of polariton quantized vortex pairs is observed in the wake of the obstacle. A quantitative analysis of the nucleation conditions in terms of local fluid velocity and density on the perimeter of the obstacle is presented.
- Perspectives and outlook of the present work are presented in Part IV. Proposals of short-term experiments on the same patterned microcavity sample and direct follow-ups of this work are presented in Chapter 8. In Chapter 9, a prospective work on the design, growth and characterization of future patterned microcavity samples is presented.

Eventually, a conclusion summarizes the main results of this thesis, and outline some perspectives for polariton physics.

Units

Throughout this work we generally use “natural” units which are scaled to the processes we are looking at. Energies are given in meV , lengths in μm and times in ps . Masses are then given in units of $meV \cdot ps^2 \cdot \mu m^{-2}$. In these units the universal constants are

$$\begin{aligned}\hbar &= 0.658 \quad meV \cdot ps \\ k_B &= 8.6 \cdot 10^{-2} \quad meV \cdot K^{-1} \\ c &= 300 \quad \mu m \cdot ps^{-1}\end{aligned}$$

Part I

Background: Physics of semiconductor microcavities

Chapter 1

Exciton polaritons

In this chapter we describe the different elements which constitute a semiconductor microcavity, and how the strong light matter coupling leads to the formation of “quasi-particles” called exciton polaritons. Examples will be given using a *GaAs*-based microcavity, such as the one which is used in the experimental work of this thesis. However, the concepts developed in this chapter can be applied to all other direct gap semiconductors, such as *GaN* or *CdTe*.

1.1 Excitons in semiconductors

1.1.1 Bulk excitons

In direct gap semiconductors, the promotion of an electron to the conduction band leaves a hole in the valence band. Coulombic interaction between the oppositely charged electron and hole leads to the formation of a bound state called exciton. This elementary excitation appears as a new line in the absorption spectrum, separated from the band gap E_g by the exciton binding energy E_b . The exciton can be seen as a hydrogenic quasi-particle, whose binding energy is analogous to the hydrogen Rydberg energy (although much smaller [35]). Semiconductor excitons are generally of the Wannier type, meaning that the electron-hole relative wavefunction is delocalized over many lattice sites. The exciton dispersion is given by

$$E_X(k) = E_g - E_b + \frac{\hbar^2 k^2}{2m_X} \quad (1.1)$$

where $\hbar k$ is the momentum of the exciton center of mass. The exciton effective mass m_X is given by the combination of electron and hole effective masses m_e and m_h as $\frac{1}{m_X} = \frac{1}{m_e} + \frac{1}{m_h}$. In *GaAs*, the exciton effective mass is typically 20 times smaller than the free electron mass [35].

1.1.2 Excitons in quantum wells

Semiconductor quantum wells (QWs) consist in a thin layer of semiconductor material, inserted between an other semiconductor material of higher band gap, e.g. 10nm of *In_{0.05}Ga_{0.95}As* inserted in bulk *GaAs*. Excitations are then confined in

one direction (that we call z), forming a two-dimensional system in the QW plane. Localization of electron and holes in the QW leads to an enhanced exciton binding energy [36, 37]. An other consequence of the QW confinement is that a QW exciton, which has a given momentum in the QW plane, is coupled to a continuum of photons which have the same in-plane component of momentum. It is therefore possible to compute an intrinsic exciton lifetime τ_X using the Fermi golden rule [38], and a corresponding homogeneous linewidth $\gamma_X = \frac{\hbar}{\tau_X}$. This latter is proportional to the exciton *oscillator strength* f_{osc} , which characterizes the strength of the excitonic transition (or the probability for a photon of given polarization to be absorbed and to create an exciton). However, the measured linewidth γ_X^* is essentially inhomogeneous, due to imperfections of the QW layer.

1.1.3 Coupling with light

The coupling of light with QW excitons must of course satisfy conservation laws for energy and in-plane momentum. Emission and absorption must also conserve the angular momentum. Excitons can be of two kinds, depending if their are constituted of a heavy hole or a light hole¹. In QWs, the confinement along the growth direction leads to a degeneracy lifting of the heavy and light hole bands. The resulting lowest energy transition occurs with the heavy hole band, whose projection of the total angular momentum on the growth axis is $m_z = \pm 3/2$. On the other hand, for the conduction band, the value of m_z is $\pm 1/2$. The total value of the projection of the angular momentum on the growth axis for the exciton is obtained from the sum of the electron and hole momentums. The four possibilities are $+2, +1, -1, -2$. The $+1$ and -1 excitons can be coupled to circularly polarized σ^+ and σ^- photons, respectively, and are therefore called *bright* excitons. The $+2$ and -2 excitons are optically inactive, as they can not satisfy the conservation of angular momentum with light, and are consequently called *dark* excitons.

1.2 Semiconductor microcavities

1.2.1 Distributed Bragg reflectors

A distributed Bragg reflector (DBR) is a periodical succession of layers of two materials with different refractive indexes. Reflection by the structure is based on an interferometric principle. The optical thickness of every layer is matched to be a quarter of the desired reflected wavelength λ_0 , so as the reflections on every interface constructively interfere. The result is the opening of a photonic band gap, centered at λ_0 , within which propagation is forbidden in the direction perpendicular to the layers (called z direction). It can be seen as a one-dimensional photonic crystal, and results in a very high quality reflector. Figure 1.1 shows typical reflectivity spectra

¹The reader can refer to Ref. [35] for more details on the influence of spin-orbit coupling on the valence band, on the heavy and light holes, or on the band mixing phenomenon that appears in QWs in the framework of Luttinger theory. The value of the effective hole mass is not so important for microcavities in the strong coupling regime, where the mass of polaritons is dominated by the cavity photon effective mass

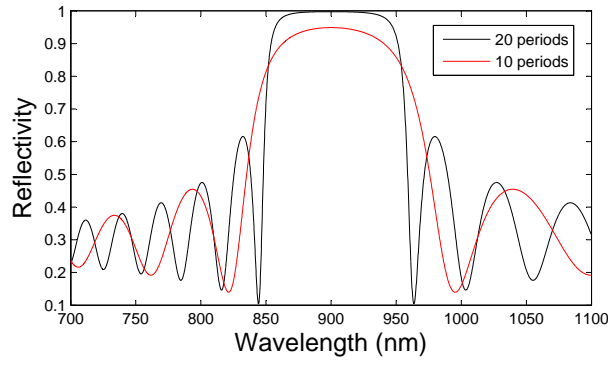


Figure 1.1: DBR reflectivity spectrum, computed using a transfer matrix method for $\lambda_0 = 900\text{nm}$, with 10 periods of *GaAs*/*AlAs* (red line) and 20 periods of *GaAs*/*AlAs* (black line). The layer thicknesses correspond to $\frac{\lambda_0}{4n}$, where the refractive indexes have been taken to be $n_{\text{GaAs}} = 3.5$ and $n_{\text{AlAs}} = 3$. Note that band gap absorption and wavelength dependence of the refractive index have not been taken into account here.

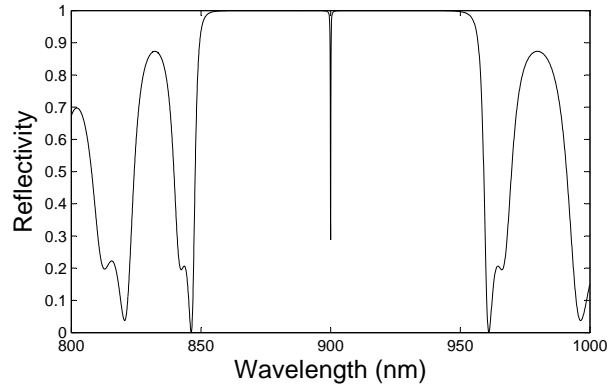


Figure 1.2: Microcavity reflectivity spectrum, computed using a transfer matrix method for $\lambda_0 = 900\text{nm}$, with two DBRs of 20 periods of *GaAs*/*AlAs* each, around a *GaAs* spacer of length $\frac{\lambda_0}{n_{\text{GaAs}}}$. Note that band gap absorption and wavelength dependence of the refractive index have not been taken into account here.

for alternate layers of refractive indexes corresponding to those of *GaAs* and *AlAs*. This example shows that increasing the number of *GaAs*/*AlAs* pairs increases the reflectivity on the photonic band gap.

1.2.2 Microcavities

When two DBRs are placed face to face around a spacer, they form a Fabry-Pérot resonator. In this structure, electromagnetic waves are confined in the z direction, but are still free to propagate in the in-plane directions, forming thus a two-dimensional system. The only optical modes admitted in the cavity are those satisfying the boundary conditions of the resonator. These modes will be allowed to be transmitted through the resonator. In this way, the microcavity spacer acts as an impurity in the one-dimensional photonic crystal [39]. A typical reflectivity spectrum is presented in Figure 1.2, for a λ -cavity. A computed intensity plot of the cavity field is presented in Figure 1.3.

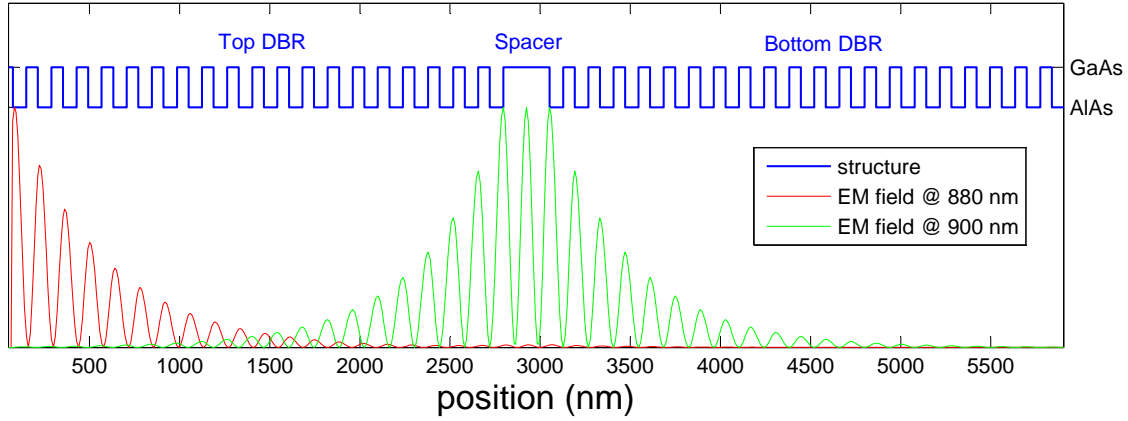


Figure 1.3: Transfer matrix simulation of the λ -microcavity EM field intensity (normalized), with a *GaAs* spacer. The blue line shows the succession of *GaAs* and *AlAs* layers. The green line corresponds to the cavity mode, which forms a standing wave pattern in the cavity. Anti-nodes of the field are formed at the *GaAs* spacer boundaries, due to the reflexion of a lower index material. The red line shows a wavelength which is not admitted in the cavity, and thus gets reflected on the top DBR.

The finite width of the cavity mode γ_C is proportional to the cavity photon escape rate, or inversely proportional to the photon lifetime in the cavity τ_C . The *quality factor* Q of the cavity depends therefore of the quality of the mirrors, and is given by $Q = \frac{E}{\gamma_C}$, where E is the emission energy. Depending on the area of measurement, the measured cavity linewidth γ_C^* can be inhomogeneous due to thickness variations of the cavity spacer and DBRs [40].

1.2.3 Photonic mode dispersion

Let us define $\mathbf{k} = (k_z, k_x, k_y)$ the cavity field wave-vector and $\mathbf{k}_{//} = (k_x, k_y)$ the cavity field in-plane wave-vector, where z is the confinement direction and (x, y) the directions in the plane of the layers. The optical modes allowed in the Fabry-Pérot resonator correspond to

$$N\pi = k_z L_c \quad (1.2)$$

where N is an integer, L_c is, in first approximation², the thickness of the cavity spacer, and $k_z = \frac{2\pi n}{\lambda_0}$, with n the cavity spacer refractive index. The in-plane photonic dispersion is then given for small $k_{//}$ by

$$E_C(k_{//}) = \frac{\hbar c}{n} \sqrt{k_z^2 + k_{//}^2} \cong \frac{\hbar c}{n} k_z \left(1 + \frac{k_{//}^2}{2k_z^2}\right) = \underbrace{\frac{\hbar c}{n} k_z}_{\frac{\hbar c}{\lambda_0}} + \frac{\hbar c}{2n k_z} k_{//}^2, \quad (1.3)$$

where k_z is linked to the cavity parameters by equation 1.2. This allows to define a

²In fact, the effective cavity length depends also of the DBRs composition, due to the finite penetration length of the cavity field in the DBRs, as can be seen on Figure 1.3.

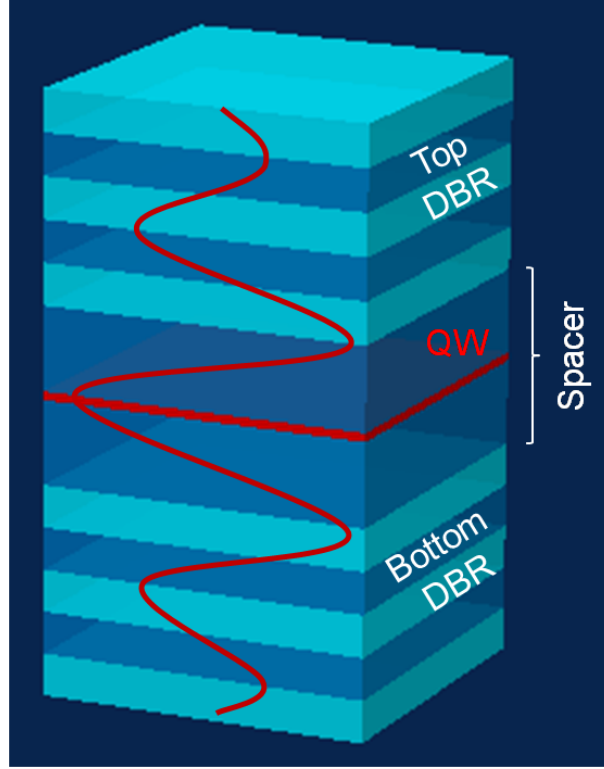


Figure 1.4: Scheme of the semiconductor microcavity, with one embedded quantum well. Only a few DBR periods are shown.

cavity photon effective mass:

$$m_C^* = \frac{\hbar k_z n}{c} = \frac{\hbar n^2}{c \lambda_0}. \quad (1.4)$$

For a *GaAs* λ -cavity, with $\lambda_0 = 835\text{nm}$, we find $m_C^* = \frac{\hbar n^2}{c \lambda_0} \cong 0.2\text{meV} \cdot \text{ps}^2 \cdot \mu\text{m}^{-2}$.

1.3 Strong light-matter coupling in microcavities

1.3.1 Exciton-photon coupling

In the cavity spacer are embedded one or several QWs (see Figure 1.4), whose excitonic resonance will interact with the microcavity optical mode. As the QW exciton and the microcavity electromagnetic field are both two-dimensional (2D) objects, there is a one-to-one coupling, with conservation of in-plane momentum and energy, between photons and excitons. As explained in section 1.1.3, there is also a one-to-one correspondence between the exciton spin and the photon polarization. Light-matter coupling in the microcavity can thus be modeled by two coupled oscillators [2]. The light-matter coupling Hamiltonian for a given in-plane momentum $k_{//}$ reads then :

$$\mathcal{H}_0(k_{//}) = E_C(k_{//})a_{k_{//}}^\dagger a_{k_{//}} + E_X(k_{//})b_{k_{//}}^\dagger b_{k_{//}} + \frac{\hbar\Omega}{2} (a_{k_{//}}^\dagger b_{k_{//}} + a_{k_{//}} b_{k_{//}}^\dagger) \quad (1.5)$$

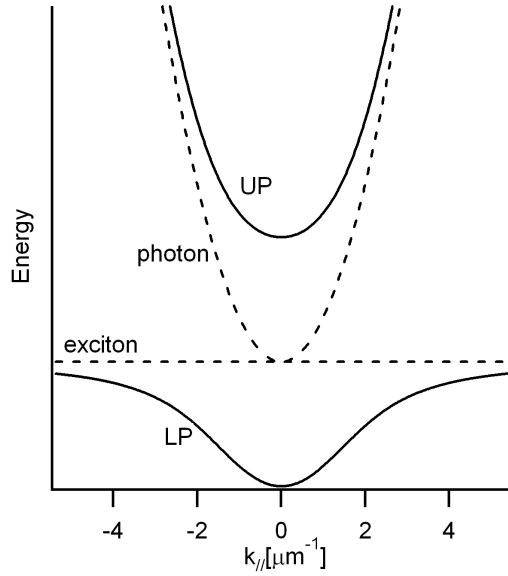


Figure 1.5: Polariton dispersions for $\delta(k_{//} = 0) = 0$. Bare exciton and photon modes are indicated with dashed lines. The eigenmodes are the lower polariton (LP) and upper polariton (UP) branches, indicated with plain lines.

where $a_{k_{//}}^\dagger$ and $a_{k_{//}} are the creation and annihilation operators for a cavity photon of given in-plane momentum $k_{//}$ and polarization, $b_{k_{//}}^\dagger$ and $b_{k_{//}} the creation and annihilation operators for the corresponding QW exciton and $\frac{\hbar\Omega}{2}$ is the exciton-photon coupling energy. In the matrix form, the Hamiltonian reads :$$

$$M(k_{//}) = \begin{pmatrix} E_C(k_{//}) & \frac{\hbar\Omega}{2} \\ \frac{\hbar\Omega}{2} & E_X(k_{//}) \end{pmatrix}. \quad (1.6)$$

Diagonalizing \mathcal{H}_0 allows to find the normal modes of the system:

$$\mathcal{H}_0(k_{//}) = E_-(k_{//})p_{k_{//}}^\dagger p_{k_{//}} + E_+(k_{//})u_{k_{//}}^\dagger u_{k_{//}} \quad (1.7)$$

where $p_{k_{//}}^\dagger$ and $u_{k_{//}}^\dagger$ are the creation operators for the lower polariton (LP) and upper polariton (UP), respectively. These normal modes are the new eigenmodes of the system, while the bare exciton and photon modes are not stationary solutions any more. The energies of the polariton branches can be found by diagonalizing $M(k_{//})$:

$$E_\pm(k_{//}) = \frac{E_X(k_{//}) + E_C(k_{//})}{2} \pm \frac{1}{2} \sqrt{\delta^2(k_{//}) + \hbar^2 |\Omega|^2} \quad (1.8)$$

where $\delta(k_{//}) = E_C(k_{//}) - E_X(k_{//})$ is the detuning of the excitonic resonance with respect to the cavity field. Figure 1.5 shows the polariton in-plane dispersion, for $\delta(0) = 0$.

As the exciton effective mass is much larger than the photon's, it appears constant on this wavevector range. At zero exciton-photon detuning, the energy splitting is given by $\hbar\Omega$, and is called the *vacuum Rabi splitting*, by analogy with atomic

optics. The first measurement of this splitting was performed by Weisbuch *et al.* in 1992 [1], by taking advantage of the varying E_C along the microcavity sample wedge. A further work by Houdré *et al.* [41] allowed to measure the polariton dispersion through angle-resolved photoluminescence measurements. Due to in-plane momentum conservation, the polariton wavevector $k_{//}$ is simply related to the extra cavity photon emission angle θ and wavelength λ_0 by $k_{//} = \frac{2\pi}{\lambda_0} \sin \theta$.

Hopfield coefficients The transfer matrix from the exciton-photon basis to the polariton basis is given by:

$$\begin{pmatrix} u_{k_{//}} \\ p_{k_{//}} \end{pmatrix} = \begin{pmatrix} -C_{k_{//}} & X_{k_{//}} \\ X_{k_{//}} & C_{k_{//}} \end{pmatrix} \begin{pmatrix} a_{k_{//}} \\ b_{k_{//}} \end{pmatrix} \quad (1.9)$$

where $X_{k_{//}}$ and $C_{k_{//}}$ are called the *Hopfield coefficients*, in memory of the first treatment of strong coupling by J.J. Hopfield for bulk excitons [42] in 1958. These coefficients satisfy

$$X_{k_{//}}^2 + C_{k_{//}}^2 = 1, \quad (1.10)$$

with $X_{k_{//}}^2$ and $C_{k_{//}}^2$ representing the excitonic and photonic contents of the lower polariton, respectively. For zero exciton-photon detuning, $X_{k_{//}}^2 = C_{k_{//}}^2 = \frac{1}{2}$.

Polariton effective mass For small in-plane wavevectors polariton dispersions can be approximated by parabolas, allowing to define an effective mass for the polaritons. Neglecting the curvature of the excitonic dispersion, effective masses for the lower and upper polaritons are given for small $k_{//}$ by

$$m_{LP} = \frac{m_C^*}{C_0^2} \quad (1.11)$$

$$m_{UP} = \frac{m_C^*}{X_0^2}. \quad (1.12)$$

We can therefore calculate the polariton effective mass for a *GaAs* λ -cavity, with $\lambda_0 = 835nm$, for zero exciton-photon detuning: $m_{LP,UP} = 2m_C^* \cong 0.4meV \cdot ps^2 \cdot \mu m^{-2}$. This effective mass is four orders of magnitude smaller than the exciton effective mass, and five orders of magnitude smaller than the free electron mass.

1.3.2 Strong and weak coupling

If polaritons are eigenstates of the system, bare exciton and photon states are not stationary solutions any more. In the exciton-photon basis, a polariton state corresponds to a periodical energy exchange between photon and exciton, at the Rabi frequency Ω . If one now consider the cavity photon and exciton lifetimes τ_C and τ_X , one can identify two regimes: if the Rabi period is shorter than τ_X and τ_C , the system is in the strong coupling regime; if, on the other hand, the Rabi period is longer than τ_X and τ_C , the system is said to be in the weak coupling regime. In the energy domain, the strong coupling condition reads :

$$\hbar\Omega > \gamma_C, \gamma_X. \quad (1.13)$$

The finesse of the cavity and quality of the QW layer are therefore of crucial importance, as well as the value of the exciton-photon coupling. This latter is proportional to [41]

$$\Omega \propto \sqrt{\frac{f_{osc} N_{QW}}{L_c}}, \quad (1.14)$$

where f_{osc} is the QW exciton oscillator strength, N_{QW} is the number of QWs in the cavity, and L_c is the cavity length. This shows that the strong coupling can be saturated when the exciton oscillator strength is saturated (see next section). The exciton-photon coupling is also proportional to the overlap integral between the QW excitons wavefunction and the cavity electromagnetic field [43]. One has then to make sure to position the QWs at anti-nodes of the cavity field, in order to maximize the coupling.

1.4 Polaritonic nonlinearities

Polaritonic nonlinearities arise from their excitonic component. The exciton-exciton interactions are due to elastic coulomb scattering, a process which is dominated by the inter-exciton exchange of carriers [44]. The Hamiltonian term describing the elastic scattering processes of two excitons with initial wavevectors k and k' , respectively, reads [45] :

$$H_{X-X} = \frac{1}{2} \sum_{k,k',q} V_{X-X} b_{k+q}^\dagger b_{k'-q}^\dagger b_k b_{k'}, \quad (1.15)$$

where V_{X-X} is the effective interaction potential. The main consequence of this interaction is a blue-shift of the polariton energy. Another source of nonlinearities is the bleaching of the exciton-photon coupling due to a screening of the exciton oscillator strength [46]. This nonlinear effect is expected at high exciton densities ($n_{sat} \sim 10^{11} \text{cm}^{-2}$ for InGaAs QWs) [47, 48]. In the polariton basis, these two contributions (exciton-exciton interaction and saturation) can be merged into an effective interaction term for the LP branch [3, 45], providing a repulsive interaction between co-circularly polarized polaritons³.

1.5 Generalized Gross-Pitaevskii equations

The most successful way of simulating the behavior of a coherent polariton gas is the framework of the mean field theory, which consider fully coherent excitonic and photonic fields $\psi_{C(X)}(\mathbf{r}, t) = |\psi_{C(X)}(\mathbf{r}, t)| e^{i\phi(\mathbf{r}, t)}$. The time evolution of the mean polariton and exciton fields ψ_C and ψ_X , in the presence of a resonant pump field $F_{p,C}(\mathbf{r}, t) = |F_{p,C}| e^{i(\mathbf{k}_p \cdot \mathbf{x} - \omega_p t)}$ (where $\hbar\omega_p$ and $\hbar\mathbf{k}_p$ are the driving laser field energy and momentum, respectively) is described by the two coupled equations [15, 14]:

³The value and sign of the effective interaction potential between cross-circularly polarized polaritons is currently subject to debate and investigation in the polariton community [49, 24].

$$\begin{aligned}
i\hbar \frac{d}{dt} \begin{pmatrix} \psi_X(\mathbf{r}, t) \\ \psi_C(\mathbf{r}, t) \end{pmatrix} &= \begin{pmatrix} 0 \\ F_{p,C}(\mathbf{r}, t) \end{pmatrix} \\
&+ \begin{pmatrix} \hbar\omega_{k,X} + V_X(\mathbf{r}) + g_X|\psi_X|^2 - i\frac{\gamma_X}{2} & \frac{\hbar\Omega}{2} \\ \frac{\hbar\Omega}{2} & \hbar\omega_{k,C} + V_C(\mathbf{r}) - i\frac{\gamma_C}{2} \end{pmatrix} \begin{pmatrix} \psi_X(\mathbf{r}, t) \\ \psi_C(\mathbf{r}, t) \end{pmatrix}
\end{aligned} \tag{1.16}$$

where $\hbar\omega_{k,X}$ is the exciton energy (considered as constant in the small wavevector limit), $\hbar\omega_{k,C}$ is the cavity photon energy, as defined in eq. 1.3, g_X is the exciton-exciton interaction constant, $\hbar\Omega$ is the vacuum Rabi energy, and $\frac{\gamma_{C(X)}}{\hbar}$ is the photonic (excitonic) decay rate. The excitonic and photonic potential landscapes are defined by $V_X(\mathbf{r})$ and $V_C(\mathbf{r})$, respectively. The excitonic landscape can be due to growth inhomogeneities of the QW layer. The photonic landscape can be due to disordered thickness variations of the cavity spacer or to disorder in the DBRs. More interestingly, it can be engineered, as it will be shown in the next chapters. If the excitation conditions are such that only the LP branch is excited, this set of equation can be restricted to a single equation for the LP branch ψ :

$$\begin{aligned}
i\hbar \frac{d}{dt} \psi(\mathbf{r}, t) &= (-i\frac{\gamma}{2} + \hbar\omega_k + g|\psi(\mathbf{r}, t)|^2) \psi(\mathbf{r}, t) \\
&+ V\psi(\mathbf{r}, t) + F_p(\mathbf{r}, t),
\end{aligned} \tag{1.17}$$

where $\hbar\omega_k = \frac{\hbar^2 k_{LP}^2}{2m_{LP}}$ is the lower polariton energy. The other parameters can be expressed through the Hopfield coefficients C and X : $g = g_X|X|^4$, $\frac{\gamma}{\hbar} = \frac{\gamma_X|X|^2 + \gamma_C|C|^2}{\hbar}$ is the polariton decay rate, and $F_p = F_{p,C}|C|^2$. Similarly, $V(\mathbf{r})$ is the effective potential landscape for the polaritons. This equation is formally a Gross-Pitaevskii equation, plus pump and decay terms. It describes therefore a non-equilibrium gas of weakly interacting bosons. Except for the non-equilibrium nature, we can therefore expect to observe the same physics in the coherent polariton gas than in a two-dimensional atomic BEC¹. Moreover the non-equilibrium character of the polariton field can be taken as an advantage. Indeed, under a *cw* pump field, the steady state solution of the polariton field inherits the pump field energy and wavevector. The polariton field energy, velocity and density can therefore be controlled by the driving field. Eventually, the decay of polaritons into extra-cavity photons allows to optically access the polariton field.

¹As long as the exciton oscillator strength is not screened due to phase space filling by the fermionic components of the exciton (see section 1.4).

Chapter 2

Polaritonic confinement in a patterned microcavity

In this chapter we explain why and how exciton polaritons are confined in semiconductor nanostructures. In particular, we detail the polaritonic confinement in a patterned microcavity. Eventually, we describe the (up to now only one) patterned microcavity sample, on which all the experimental work of this thesis has been performed.

2.1 Confining exciton polaritons

2.1.1 Why confining exciton polaritons?

Research on the lateral confinement of exciton exciton polaritons has been triggered by the quest of polariton Bose-Einstein condensation (BEC) in microcavities. Formally forbidden in uniform two-dimensional gases, BEC is allowed in spatially confined systems, which feature discrete energy levels (see Savona & Sarchi in [50]). The role of confinement by disorder landscape has indeed been highlighted for the condensation experiments in CdTe microcavities [51, 52]. Other experimental works have demonstrated the role of confinement in this perspective, using local strain on the sample [53], a metallic grid on the sample surface [54] or by etching micro-pillars [22]. In case of stimulated relaxation towards the discrete states of fully confined system, as in Ref. [22], one talks about *polariton lasing* rather than condensation, as long range order cannot be defined for zero-dimensional (0D) objects.

Polaritonic confinement can however be exploited for many other purposes, as shown by numerous theoretical and experimental works. For the study of fundamental physics, let us mention the proposals for controlled Josephson oscillations [55] and fermionized photons in coupled cavity arrays [56], or the study of one-dimensional interacting quantum gases [57].

On the side of applications, polaritonic confinement is expected to facilitate the generation of entangled photon pairs, due to the relaxation of the momentum conservation condition [58, 59]. The exploitation of few-confined-states structures for quantum blockade and single photon emission has also been proposed [17, 60]. Recent theoretical works also proposed specific lateral confinement geometries in

order to perform logical operations [19, 20]. In this scope, the realization of shape controlled polaritonic confinement is required.

Eventually, a very interesting aspect of lateral confinement is the increase of the cavity quality factor, as confinement allows to get rid of lateral inhomogeneities. An increase of the quality factor by a factor of three has been measured in micro-pillars microcavities [61].

2.1.2 State of the art

The most established technique for polaritonic confinement is definitely the etching of micro-pillar microcavities [21]. In these structures, polariton lasing [22], parametric luminescence [62] and oscillation [63], and condensation in a one-dimensional guide [57] were demonstrated. Other interesting lateral confinement techniques have been developed in different groups. The deposition of a metallic pattern on the microcavity sample surface [54, 64] allows to confine polaritons by perturbing the boundary condition of the cavity resonance. Strain induced by the pressure of a needle on the sample [53, 65] confines polaritons by shifting the excitonic resonance. Eventually, a very promising technique using surface acoustic waves has been reported recently [66]. In our group, a different approach has been developed, consisting in patterning the microcavity. This technique is presented in the following section.

2.2 Sample: a patterned microcavity

2.2.1 Confinement in a patterned microcavity

The growth of patterned microcavities is done in two steps (the whole process is described in detail in Ounsi El Daïf's thesis [67]). The bottom DBR and GaAs cavity spacer, including the QW, are grown first by molecular beam epitaxy (MBE). The structure is then taken out of the MBE machine and brought to the clean room. A mask is deposited on the sample surface using photolithography, and a selective wet etching (controlled with etch-stops made of thin AlAs layers) of the structures is realized. After a standard cleaning of the surface, the patterned structure is reinserted in the MBE chamber, where an *in-situ* hydrogen plasma cleaning of the patterned surface is realized, before the growth of the top DBR.

The result is a patterned microcavity, where the confining structures are local extensions of the cavity spacer thickness (or *mesas*), as shown in Figure 2.1 (a). The local extension of the spacer length provides a slightly longer cavity resonance, and therefore a lower local electromagnetic field energy. When the optical modes confined in this potential well are strongly coupled to the QW exciton, they give rise to confined polariton modes for the upper and lower polariton branch (Figure 2.1 (b)). The main particularity of this kind of structure is the coexistence of the confined polariton states with the two-dimensional polaritons, still present around the traps. The lithographic method allows the realization of traps of virtually any shape.

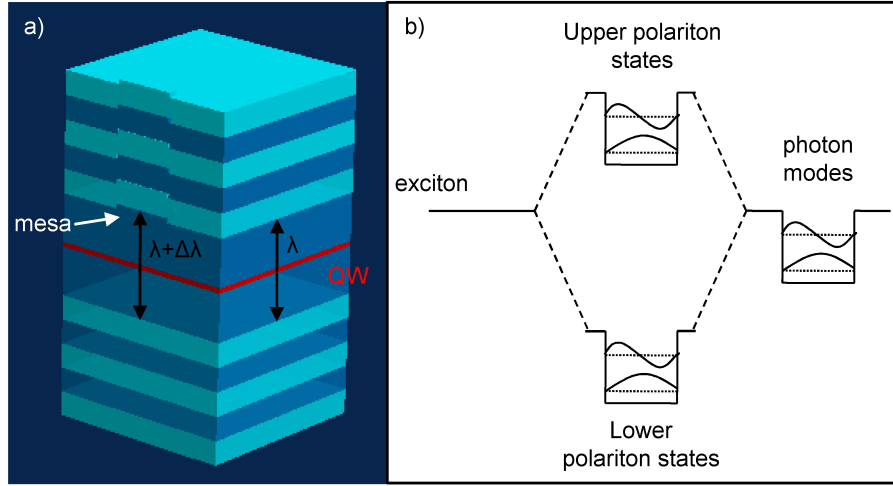


Figure 2.1: (a) Scheme of the lateral confinement structure using *mesas*, which provide a local extension of the cavity length of $\Delta\lambda = 6nm$, providing a confinement potential of $9meV$ for the photonic mode. (b) Scheme of the normal mode splitting (or Rabi splitting) arising from the strong coupling between the quantum well excitonic resonance and the confined photonic modes. It results in discrete confined states for the upper and the lower polariton branches. The excitonic component of the polariton is by this way confined as well, through the strong-exciton photon coupling.

2.2.2 Sample description

The sample under scrutiny is the only one patterned microcavity realized so far [23]. It consists in a GaAs cavity spacer with one embedded $8nm$ thick InGaAs QW, sandwiched between two semiconductor Al/GaAs DBRs made of 22 and 21 pairs for the bottom and top DBR respectively. The QW exciton emission wavelength is $835.15nm$ at liquid helium temperature ($T \leq 10K$), corresponding to an energy of $E_x = 1.4845eV$. The exciton (inhomogeneous) linewidth is measured to be $\gamma_X^* = 500\mu eV$. The cavity mode FWHM is measured at large exciton-photon detuning to be $\gamma_C^* = 220\mu eV$, corresponding to a quality factor of $Q = 7 \cdot 10^3$. On the other hand, confinement in the mesas allows to get rid of most of the inhomogeneous broadening due to photonic disorder, and FWHM of the confined photonic modes are measured down to $70\mu eV$, corresponding to a quality factor of $Q = 2.1 \cdot 10^4$. The sample features a thickness wedge (mainly on the GaAs component), providing an optical resonance varying along the radius of the wafer. It is made such that the exciton can be in resonance with either the two-dimensional fundamental photon mode λ , either with the confined photonic modes, depending on the position on the sample. Two-dimensional and confined polaritons at zero exciton-photon detuning are thus present on the same sample. Anticrossing between the photonic and excitonic modes, signature of the strong exciton-photon coupling can be measured along the sample wedge. A Rabi splitting of $3.5meV$ has been measured for the two-dimensional polaritons, and of $3.35meV$ for the confined polariton modes. The major advantage of using InGaAs QWs is that their emission energy is smaller than the GaAs band gap. Resonant optical excitation of the polariton modes can therefore very conveniently be performed from the back side of the sample, through

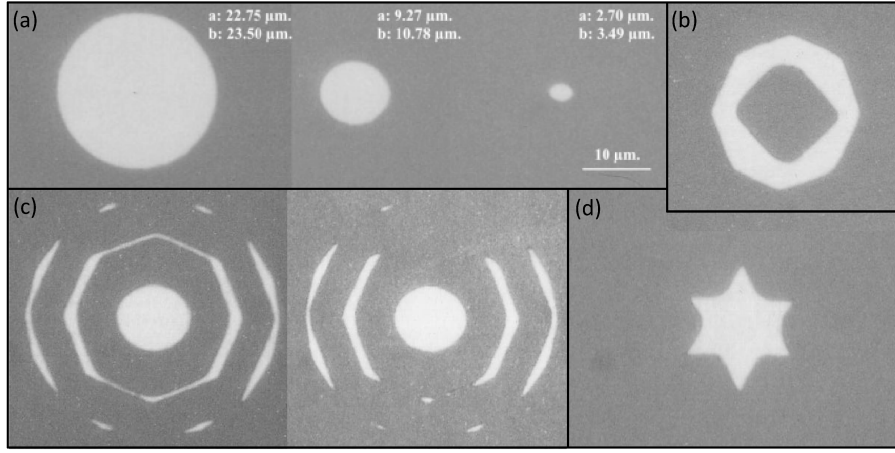


Figure 2.2: Photographs of the mask used for the photolithographic process. Different confinement geometries are shown. (a) Intended to be circular, these traps are actually elliptical. The measured length of the minor and major axis are indicated on the picture. (b) to (d) Exotic shapes.

the GaAs substrate. The detection can then be performed from the front side, in a transmission configuration, without being dazzled by the laser light reflected on the DBR.

Confinement geometries The height of the confining structures is $\Delta\lambda = 6nm$, providing a confinement potential of $9meV$ for the photonic mode. The resulting effective confining potential for the polariton depends then on the exciton-photon detuning. Various trap shapes have been etched on the sample. Photographs of the mask used for the photolithography are shown in Figure 2.2. The structures that will be used for the experiments presented in Chapters 3, 4, 5 and 6 are mainly the one of Figure 2.2 (a). Intended to be circular traps, they are slightly elliptical due to an asymmetry of the laser used to write the mask. The consequences of this ellipticity will be widely discussed in the next chapters. Their mean diameters are $3\mu m$, $10\mu m$ and $22\mu m$ respectively. Other structures, such as rings (Figure 2.2 (b)) or more exotic structures which were primarily intended to facilitate relaxation of the polaritons into the traps, are shown in Figure 2.2 (c) and (d). All of them suffered from the mask asymmetry. Moreover, it can be seen that the writing of the mask was not totally uniform, and slight differences can be observed between structures that were intended to be identical, like those shown in Figure 2.2 (c). In addition to this, variations from structure to structure must be accounted for due to the non-homogeneous deposition of the photoresist on which the mask is imprinted during the photolithography, and to crystal defects and sample aging. The images of the mask shown in Figure Figure 2.2 represent therefore the average shape of the actual confining potentials found on the microcavity sample. We will present in Chapter 3 a method that allows to characterize the effective confinement geometry of individual structures.

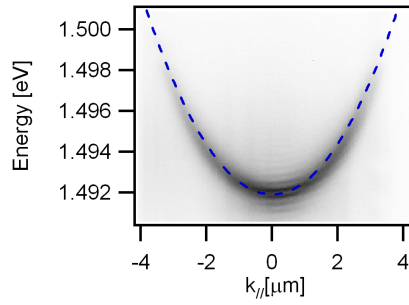


Figure 2.3: Experimentally measured dispersion of the cavity mode of the patterned microcavity sample (see section 3.4 for the experimental method). The fit (blue dashed line) allows to determine the cavity photon effective mass. We find $m_C^* = 0.35 \text{ meV} \cdot \text{ps}^2 \cdot \mu\text{m}^{-2}$.

Measurement of polariton effective mass The value of the cavity photon effective mass m_C^* can be measured from the photonic dispersion (measured at large exciton-photon detuning) $E_{ph} = \frac{\hbar^2 k^2}{2m_C^*}$. This dispersion is measured using Fourier space imaging spectroscopy (see section 3.4 for details), and shown in Figure 2.3. The fit of the curve allows to extract a cavity photon effective mass of $0.35 \text{ meV} \cdot \text{ps}^2 \cdot \mu\text{m}^{-2}$ (corresponding to a polariton effective mass at zero exciton-photon detuning of $0.7 \text{ meV} \times \text{ps}^2 \times \mu\text{m}^{-2}$, according to eq. 1.11). This measured photon effective mass is of the order of the theoretical value of $0.2 \text{ meV} \cdot \text{ps}^2 \cdot \mu\text{m}^{-2}$ found in section 1.2.3. At this stage we do not have an explanation for the small discrepancy between the theoretical and measured values.

2.2.3 Previous works on the sample

Several works were already published on the patterned microcavity sample which is used in this thesis. The polaritonic confinement in the nearly circular mesas was demonstrated with the measurement of the multiple anti-crossing (i.e. anticrossing of each confined states with the excitonic resonance, measured along the sample wedge on a series of periodically aligned similar mesas) [23, 68].

Angle-resolved spectra and preliminary measurements of spatially resolved spectra were measured in traps of various sizes [69], allowing to show different confinement cases, from full confinement (with few, well separated confined states) in the $3 \mu\text{m}$ diameter mesas, to a quasi-continuum of states in the large $20 \mu\text{m}$ diameter mesas. These spectra were successfully reproduced by a model that considered the strong coupling of the confined photonic modes with excitons [69, 70].

Studies of the non-linear emission of the confined states were also conducted. Under non-resonant pumping, non-linear emission in the form of a quadratic dependence to pump power was observed in the strong coupling regime [71], but no stimulated relaxation could be obtained, due to a bleaching of the strong coupling before reaching the condensation or polariton lasing threshold. This was attributed to a saturation of the active medium (excitonic transition - see sections 1.3.2 and

1.4), due to the presence of only one QW in the cavity ¹². A transition to standard lasing on the confined photon modes was observed instead. In a parametric configuration (using three confined states of the lower polariton branch as pump, signal and idler states), a quadratic regime -sign of polariton-polariton interactions- followed by an optical limiter regime, was also reported [72]. Although no stimulated relaxation could be observed in this sample, the confinement has been demonstrated to enhance the thermalization and linear relaxation mechanisms (through scattering with phonons) towards the low energy states of the traps [73].

¹The subsequent achievement of polariton lasing in micropillar microcavities [22] was realized with 21 embedded QWs.

²Under non-resonant excitation, the saturation is enhanced due to the presence of hot electron-hole pairs, which contribute to the screening of the exciton oscillator strength [46], but not to the final state population

Part II

Spectroscopy and imaging of confined polaritons

Chapter 3

Probability density tomography of confined polaritons

3.1 Motivations

Probing wavefunctions or probability densities (PDs) of confined carriers in semiconductor nanostructures is a very elegant way of retrieving textbook solutions of quantum confinement. Moreover, it can be of practical importance to precisely determine the spatial and energetic extensions of the confined states in a particular structure, in order, for example, to evaluate the coupling between different nanostructures. In the past, sophisticated techniques such as the insertion of probe layers [74, 75] have been developed to reconstruct the spatial variation of confined carrier PDs in the growth (vertical) direction of a quantum well (QW). Nevertheless, such techniques are dedicated to the study of PDs along a single confinement axis. They cannot be applied in the case of 2D or 3D confining potentials. The study of the in-plane (lateral) spatial extension of electronic wavefunctions is generally restricted to metallic surfaces and films, using scanning tunneling microscopy [76, 77]. In the following chapter, we demonstrate a technique that allows to image the probability density of laterally confined polariton states. Taking advantage of the strong coupling regime, we can image the light-matter waves confined in micrometer-scale traps, above the resolution of optical microscopy. Moreover, as intra-cavity polaritons are directly coupled to extra-cavity photons, with energy and momentum conservation [2], polaritonic states can be directly imaged through optical detection of the polariton emission at the surface of the sample. This technique will be used to characterize different confining structures of the patterned microcavity described in section 2.2. The work presented in this chapter corresponds to the following publications [78, 79].

3.2 Imaging spectroscopy setup

The sample is held in a cold finger cryostat at liquid helium temperature. We excite non-resonantly the system using a Ti:Sapphire *cw* laser, tuned at a far higher energy than the confined polariton states. The laser is focused on the sample with an excitation spot of $30\mu m$ diameter. This hot excitation creates electron hole pairs

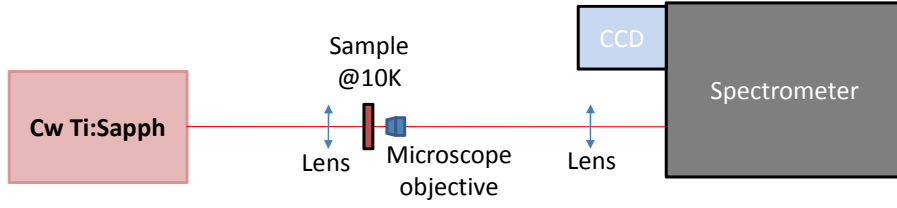


Figure 3.1: Imaging spectroscopy setup. The sample is held in a liquid helium cryostat (not shown).

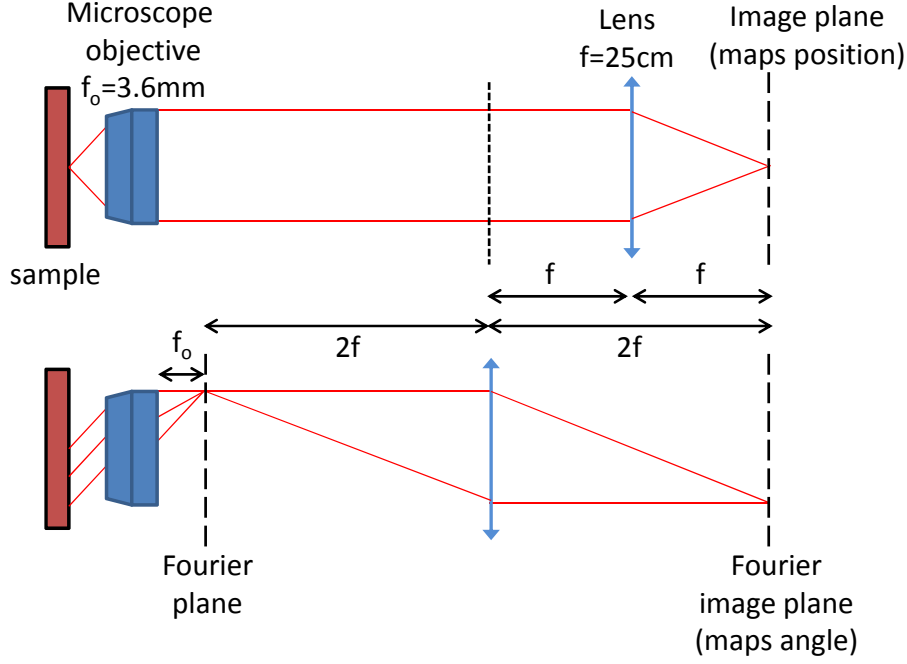


Figure 3.2: $2f-2f$ configuration. The imaging lens, of focal length $f = 25\text{cm}$ can easily be positioned in order to image real space or Fourier space emission patterns. In the second configuration, a Fourier plane is formed at a distance f_o of the microscope objective, where f_o is the microscope objective focal distance.

which relax to the confined and delocalized polariton states [23, 73]. Then, due to the coupling with extra-cavity photons, the eigenmodes emit photoluminescence (PL), which is collected with a 0.5 NA microscope objective and imaged on the slit of a spectrometer using a lens of $f = 25\text{cm}$ focal length, with a diffraction limited spatial resolution (see Fig. 3.1). Using a $2f-2f$ imaging configuration, we can conveniently image the near or the far field emission pattern (see Fig. 3.2). At the output of the spectrometer, a liquid nitrogen cooled CCD camera records images of the PL with one spectral dimension and one spatial dimension. The magnification of the setup is given by the ratio of the microscope objective effective focal length ($f_o = 3.6\text{mm}$) and the imaging lens focal length: $M \approx 70\times$. The spectral resolution of the spectrometer is $\sim 25\mu\text{eV}$. We keep a low excitation power in order to prevent non-linear effects to take place. Examples of spatially resolved spectra, as well as the “tomography” process, are detailed in the next section for quasi-cylindrical polaritonic traps of various sizes.

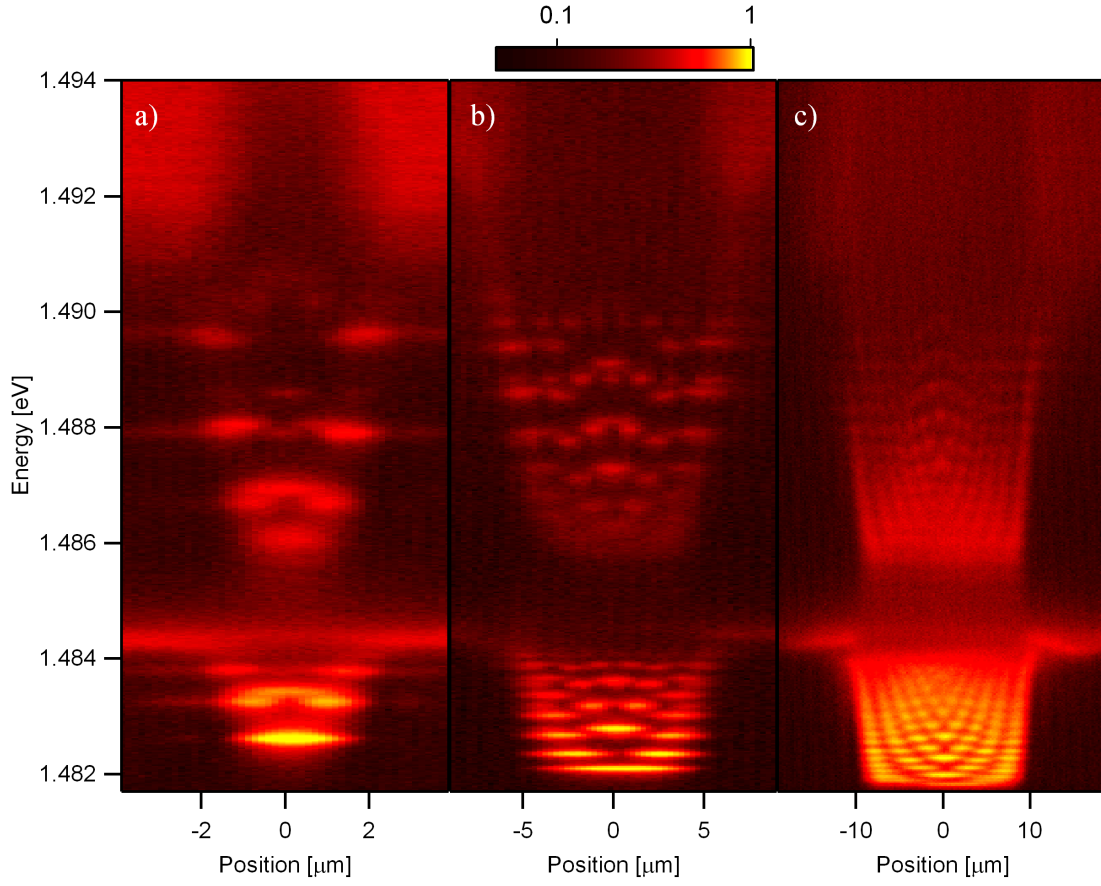


Figure 3.3: Spatially resolved photoluminescence (PL) spectra of polaritons confined in quasi-cylindrical cylindrical traps of different sizes (approximatively (a) $3\mu m$, (b) $10\mu m$, and (c) $20\mu m$ diameter). The PL intensity is plotted in a normalized log color scale. Confined lower polariton states are visible below $1.484eV$. Confined upper polariton states are found between $1.485eV$ and $1.490eV$. The two-dimensional excitonic-like lower polariton energy is $1.4845eV$, and the two-dimensional photonic-like upper polariton is visible above $1.492eV$.

3.3 Tomography in quasi-cylindrical traps

3.3.1 Experimental results

Spatially resolved PL spectra are presented in Fig 3.3, for the three different trap sizes detailed in Fig. 2.2 (approximatively $3\mu m$ (a), $10\mu m$ (b), and $20\mu m$ (c) diameter). These images allow to see discrete states for the lower and upper polariton branches. The traps are surrounded by two-dimensional (2D) polaritons at $1.4845eV$ for the lower 2D polariton (excitonic-like at this detuning), and above $1.492eV$ for the upper 2D polariton (photonic-like). The number of confined states depends on the trap size. The $3\mu m$ diameter trap contains only a few, well defined confined states [Fig 3.3 (a)]. The larger traps house more states, which tend to form a quasi-continuum in the largest trap of $20\mu m$ diameter [Fig 3.3 (c)]. The linewidth of the confined states is measured to be $80\mu eV$. Such spectra already allow to observe the PD distribution for all eigenstates along one spatial direction, which is the direction

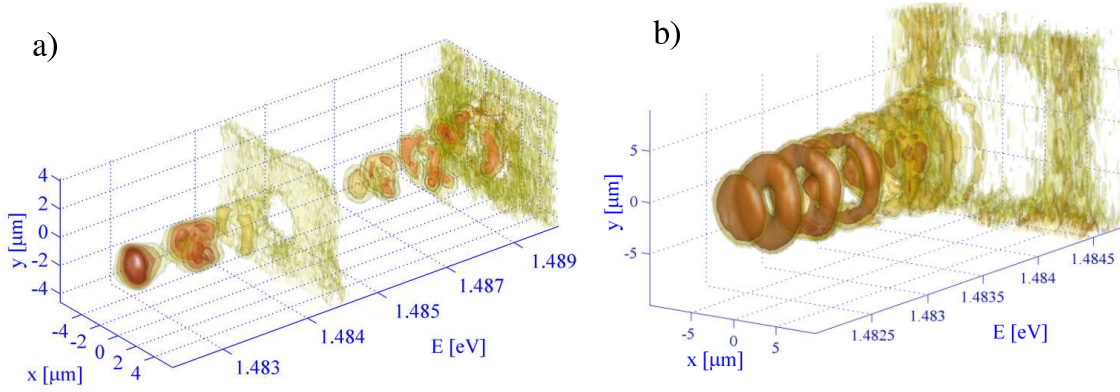


Figure 3.4: (x,y,E) view of the photoluminescence intensity of the system, for a trap of (a) $3\mu\text{m}$ and (b) $10\mu\text{m}$ (only lower polariton states are shown in (b)). Isosurfaces of same intensity are plotted, allowing to map the 2D spatial PD distribution of every confined and extended state for the upper and lower polaritons at the same time. For the sake of visibility, the energy scale is stretched on the lower polariton energy range. To observe easily all confined states PDs, the PL intensity at every energy was multiplied by a Boltzmann factor with $T = 30\text{K}$ for (a) and $T = 70\text{K}$ for (b), in order to compensate for the quasi thermal intensity distribution.

of the spectrometer slit. Indeed, the image of the polariton traps being larger than the spectrometer slit opening, the polariton emission is filtered by the slit. On Fig. 3.3, we have centered the image of the trap on the slit, in order to select a diameter of the trap. In this case, the spatial resolution provides a direct access to the radial part of the probability density.

The variations of emission intensity between the different confined states in Figure 3.3 (a), (b) and (c) are due to the different photonic fraction of the confined states and to thermalization towards the lower energy states [73]. Reference [73] shows as well that relaxation mechanisms and thermalization are enhanced as the trap size decreases.

In order to perform a full tomography of the system, i.e. to obtain a 2D mapping of the PL at all energies in the same set of data, we shifted the position of the imaging lens perpendicularly to the optical axis. By this way we scanned the collected PL across the slit of the spectrometer, thus providing the second spatial dimension. We obtain in this way a 3-dimensional mapping (x,y,energy) of the PL intensity, which is presented in a 3D contour plot for the $3\mu\text{m}$ trap in Figure 3.4 (a) and for the lower polariton of a $10\mu\text{m}$ trap in Fig. 3.4 (b). For the sake of visibility, we corrected the PL intensity at each energy by a Boltzmann factor, in order to counterbalance the thermalization towards the lower energy states. On Fig. 3.4 (a), all confined states of the upper and lower polaritons are visible, as well as the extended 2D polaritons, at a glance. For both the $3\mu\text{m}$ trap and the $10\mu\text{m}$ trap, one can clearly observe that the luminescence of the 2D polaritons vanishes at the exact position of the mesa. This feature is particularly meaningful for the lower 2D polariton, as it is nearly 100% excitonic at this position. It is a straightforward experimental demonstration that, although the confinement is initially acting on the photonic modes only, the excitonic component (and *a fortiori* the entire polariton) is eventually confined as well, thanks to the strong coupling between the light and the matter wave.

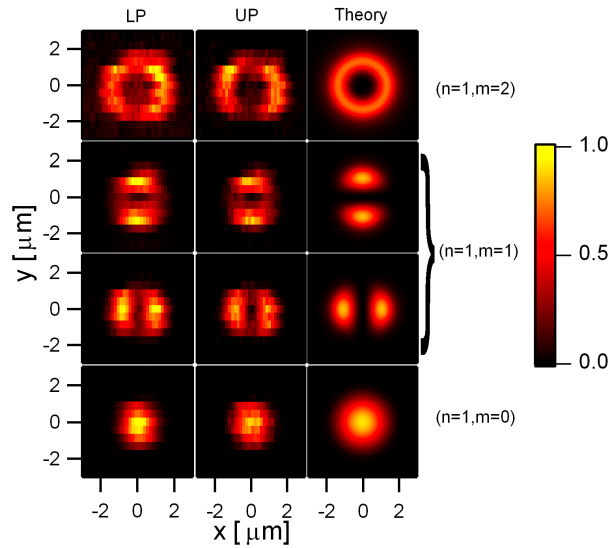


Figure 3.5: Two-dimensional PL mappings at different energies in a $3\mu\text{m}$ diameter trap, in a normalized linear color scale. These mappings provide the probability density patterns for lower polariton states (left column) and upper polariton states (central column). Corresponding solutions of the wave equation for a cylindrical confinement are displayed in the right column. The lower row shows a $(n = 1, m = 0)$ state pattern. The two central rows show two $(n = 1, m = 1)$ state patterns, the symmetry breaking being due to the elliptical shape of the trap. The upper row shows a $(n = 1, m = 2)$ state pattern. An angular variation of the type $\cos(m\phi)$ has been manually added in the computation of the $(n = 1, m = 1)$ doublet state in order to reproduce the effect of the symmetry breaking.

By cutting slices in the (x, y) plane of this set of data we can retrieve 2D mappings of the probability distribution $\|\Psi(r, \theta)\|^2$ of any eigenstate. These are plotted for the $3\mu\text{m}$ diameter trap in Fig. 3.5 for the ground state and first two excited states of both the lower (left column) and upper (central column) polaritons. We can see that lower and upper confined states have similar PD patterns.

In order to understand these patterns, let us consider in first approximation the traps as circular. We will see further on the effect of the deviations from cylindrical symmetry on the spectrum and the wavefunctions. In polar coordinates (r, ϕ) , the wavefunction can be written as

$$\Psi_{n,m}(r, \phi) = R_{n,m} e^{\pm im\phi} \quad (3.1)$$

where $R_{n,m}$ is the radial part of the wavefunction, and $e^{\pm im\phi}$ is an angular phase term. The radial part is a Bessel function inside the trap, and a modified Bessel function outside the trap. The confined states are labeled by two quantum numbers (n, m) , with $n = 1, 2, 3 \dots$ and $m = 0, 1, 2 \dots$. In polar coordinates, n gives the number of lobes of the wavefunction in the radial direction. For a perfect cylindrical symmetry, $+m$ and $-m$ states are degenerate. The $\Psi_{n,m}(r, \phi)$ are plotted in the last column of Fig. 3.5.

The bottom row of Fig. 3.5 shows a ground confined state pattern, with quantum numbers $(n = 1, m = 0)$. For this state, the experimental patterns corresponds to the solution of the wave equation in a cylindrical trap. Let us now consider the

PD patterns displayed on the two central lines of Figure 3.5. We must point out here that in principle in a system with a perfect cylindrical symmetry, $\pm m$ states are degenerate with no fixed phase relation between each other. In time integrated measurement of PL intensity of the eigenstates, this symmetry prevents one from observing any azimuthal variation of the wavefunction. This is obviously not the case for this ($n = 1, m = 1$) state, which is split into two. The two state patterns are featuring two lobes, aligned along two orthogonal axes. This is an unambiguous sign of symmetry breaking, already observed spectrally by El Daïf *et al.* [23], due to the elliptical shape of the mesa. This gives rise to a lift of the degeneracy for the $m = 1$ states. The two states are separated by an energy of $200\mu\text{eV}$ and exhibit lobes which are pinned along the main axes of the elliptical confinement potential. The breaking of the cylindrical symmetry mainly affects $m = 1$ states, because the perturbation on the confinement potential scales as $\cos(2\phi)$ (this point will be detailed further on in section 3.3.2). Indeed, for the ($n = 1, m = 2$) states displayed in the top row of Fig. 3.5, we do not observe lobes, neither a doublet structure.

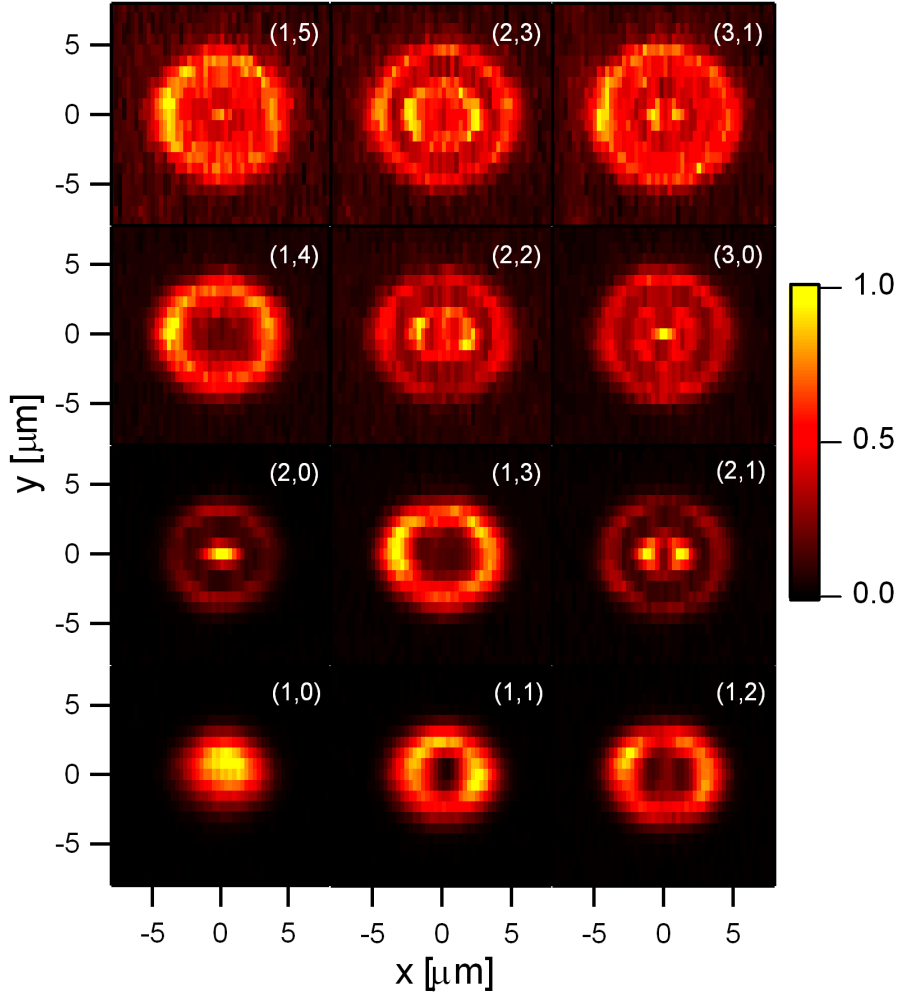


Figure 3.6: Two-dimensional PL mappings at different energies for the lower polariton states in a $10\mu\text{m}$ diameter trap, in a normalized linear color scale. These mappings provide the probability density patterns for different polariton states, whose quantum numbers (n, m) are indicated with white letters.

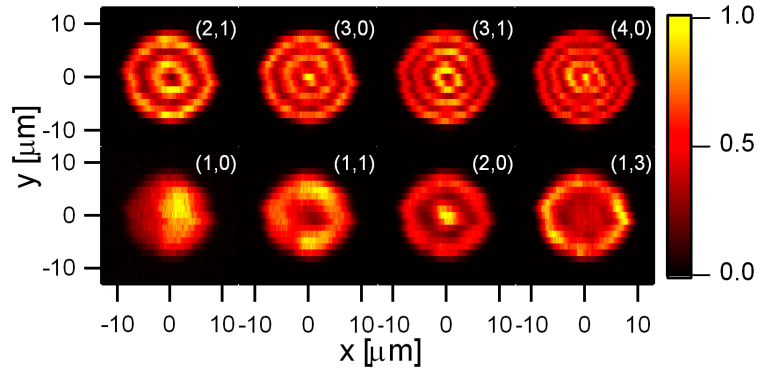


Figure 3.7: Two-dimensional PL mappings at different energies for the lower polariton states in a $20\mu\text{m}$ diameter trap, in a normalized linear color scale. These mappings provide the probability density patterns for different polariton states, whose quantum numbers (n, m) are indicated with white letters.

The ellipticity of the potential is less pronounced for the $10\mu\text{m}$ mesa. One can indeed see in Figure 3.6 that cylindrical symmetry is virtually respected for the confined states. However, comparing spatially resolved spectra for different positions allows to notice a very small degeneracy lift for the $(n = 1, m = 1)$ state. The splitting, of the order of $50\mu\text{eV}$ (with a spectral resolution of $25\mu\text{eV}$), is smaller than the linewidth ($\approx 80\mu\text{eV}$). The two split states can therefore not be imaged properly, as for the $3\mu\text{m}$ trap of Fig.3.5.

Eventually, Figure 3.7 shows the state patterns obtained for a $20\mu\text{m}$ trap. For this mesa size, the ellipticity is even less pronounced. This has for result that all confined states present a cylindrical symmetry, within our spectral resolution limit.

3.3.2 Computation of the spectrum

Approximation with a cylindrical trap

Approximating the traps as cylindrical, previous theoretical works [70, 69] were able to accurately reproduce the spectra and wavefunctions of the confined polaritons. It consisted in solving Maxwell equations for the confined electromagnetic modes, and then to strongly couple the obtained modes to the excitonic resonance. In order to intuitively understand the observed spectra in terms of a quasiparticle confined in a box, we are considering in the following a simpler approach.

We solve the linear time-independent Schrödinger equation for the polariton in a cylindrical finite potential. The polariton effective mass is given by eq. 1.11 and therefore depends of the exciton-photon detuning. Its value is $0.7\text{meV} \cdot \text{ps}^2 \cdot \mu\text{m}^{-2}$ at zero exciton-photon detuning, as measured in section 2.2. We use an effective potential barrier, which is different for upper and lower polaritons. We follow the method described by Leyronas & Combescot [80] in order to compute the eigenenergies and eigenstates of the cylindrical finite potential barrier. Figure 3.8 shows the the comparison between measured and computed spectra for a $3\mu\text{m}$ trap. We have assumed the exciton-photon detuning to be zero, as it is the case for the confined ground state.

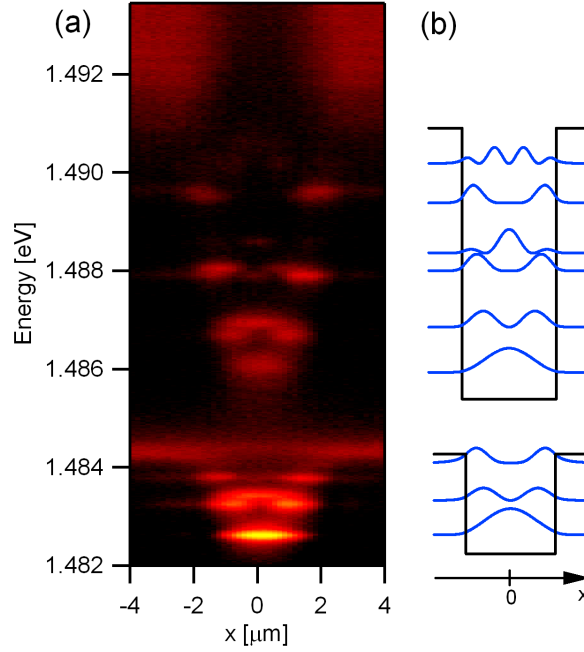


Figure 3.8: Comparison between (a) experimental spectrum, and (b) spectrum computed using the linear time-independent Schrödinger equation, for a $3\mu\text{m}$ diameter trap. In (b), we have assumed the exciton-photon coupling to be zero, and therefore used a polariton effective mass of $0.7\text{meV} \cdot \text{ps}^2 \cdot \mu\text{m}^{-2}$.

In this example, the overall agreement is good. The most obvious discrepancy is the splitting of the $(n = 1, m = 1)$ state, due to the breaking of the cylindrical symmetry. One can however also notice discrepancies for the energies of the high energy states. This is explained by the fact that there is a different exciton-photon detuning for these states, and therefore a different effective mass. This shows the limit of this simple model. In particular, it is not able to predict accurately the number of confined states for larger traps, as those traps contain numerous high energy states.

Deviations from cylindrical symmetry

When the cylindrical symmetry is broken due to the ellipticity of the trap, $\Psi_{n,m}(r, \phi) = R_{n,m}e^{\pm im\phi}$ are no longer the eigenstates of the trap. Let us consider the effect of the ellipticity on the angular part of the wavefunction $\psi_{\pm m} = e^{\pm im\phi}$. The symmetry breaking introduces off-diagonal matrix elements that are coupling ψ_{+m} and ψ_{-m} states. We express the confinement potential as $V(r, \phi) = V_0(r) + \delta V(r, \phi)$, where $\delta V(r, \phi)$ is the elliptical perturbation of the potential. The characteristic coupling energy is given by the perturbation matrix elements $W_{m,m'}$, whose azimuthal components are given by

$$W_{m,m'}(\phi) = \langle \psi_m | \delta V(\phi) | \psi_{m'} \rangle = \int \delta V(\phi) e^{i(m'-m)\phi} d\phi \quad (3.2)$$

which is nothing but the Fourier transform of the angular variation of the potential with respect to the transform variable $(m - m')/2\pi$. The angular perturbation

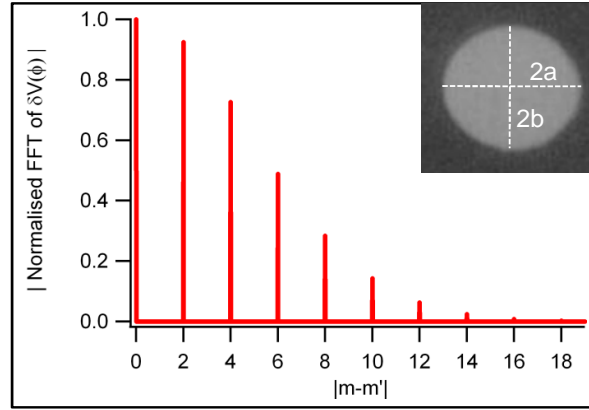


Figure 3.9: Absolute value of the fast Fourier transform (FFT) of the the angular expression of the elliptical confinement potential $\delta V^n(\phi)$ (defined in equation (3.3), with $n = 100$, and using a and b as measured for a $10\mu m$ trap). The FFT is plotted with respect to the parameter $|m - m'|$ in order to express the coupling between states ψ_m and $\psi_{m'}$. We can see that the coupling is non-zero only for states satisfying $|m - m'| = 2u$, where $u \in \mathbb{N}$, and that it is monotonically decreasing over this set of values. The amplitude of the FFT is normalized to its cw component. *Inset:* Picture of the mask used for the photolithography of the $10\mu m$ polariton traps. We measured the elliptical major and minor axes $2a$ and $2b$ to be $2a = 10.78\mu m$ and $2b = 9.27\mu m$.

of the potential δV can be evaluated in the following way: let us describe, as an example, the confinement potential as an infinite elliptic potential well $V(r, \phi) = \lim_{n \rightarrow \infty} \left(\frac{r}{r_\phi} \right)^n V^*$, where r_ϕ is the azimuthal dependence of the potential radius, given by $r_\phi = \frac{ab}{\sqrt{(a \sin \phi)^2 + (b \cos \phi)^2}}$ (with a and b the semimajor and semiminor axes of the elliptical confinement), and V^* has the dimension of energy. It is then possible to express the perturbation of the confining potential as

$$\begin{aligned} \delta V(r, \phi) &= V^* \lim_{n \rightarrow \infty} \left[\left(\frac{r}{r_\phi} \right)^n - \left(\frac{r}{\frac{a+b}{2}} \right)^n \right] \\ &= V^* \lim_{n \rightarrow \infty} \left[r^n \underbrace{\left\{ r_\phi^{-n} - \left(\frac{a+b}{2} \right)^{-n} \right\}}_{\equiv \delta V^n(\phi)} \right] \end{aligned} \quad (3.3)$$

The Fourier transform of the angular variation of the confinement potential $\delta V^n(\phi)$ is presented in Fig. 3.9¹, for $n = 100$, and a, b measured from the photolithographic mask used for a $10\mu m$ trap. It shows that the coupling is non-zero only for states satisfying $|m - m'| = 2u$, where $u \in \mathbb{N}$, and that it is monotonically decreasing over this set of values. Therefore, the most important coupling occurs between states with quantum numbers satisfying $|m - m'| = 2$. This simple analysis allows us to understand why the most significant coupling is observed between the $m = +1$

¹The absolute value of the fast Fourier transform (FFT) has to be taken because of a numerical artifact of the FFT algorithm, which gives successively positive and negative values, whereas only positive values are expected for this Fourier transform.

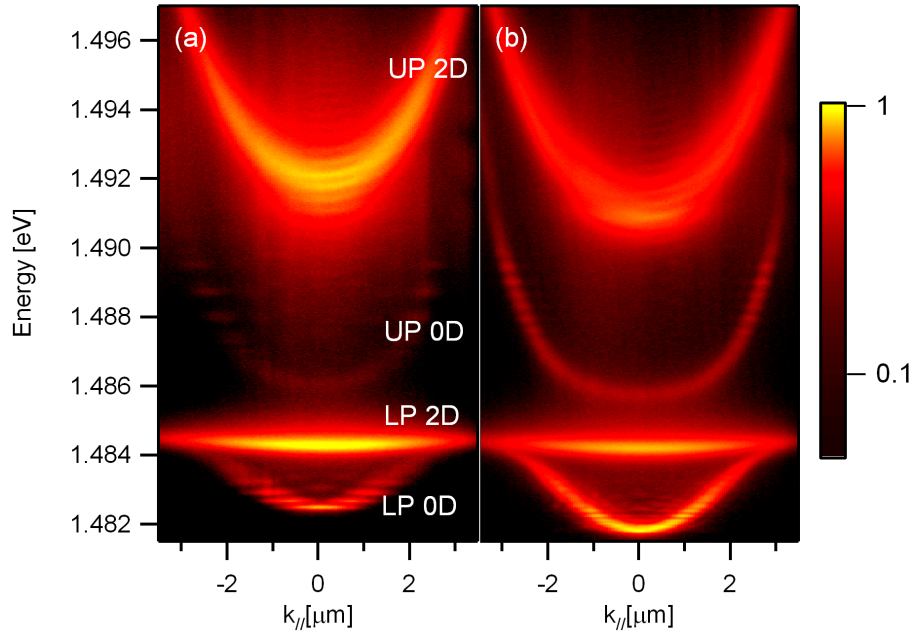


Figure 3.10: Fourier space imaging spectroscopy. The photoluminescence (PL) intensity is plotted with respect to emission energy and in-plane momentum $k_{//}$, for (a) a $10\mu m$ trap and (b) a $20\mu m$ trap, in a normalized log color scale. $k_{//}$ is related to the emission angle by $k_{//} = \frac{2\pi}{\lambda_0} \sin \theta$, where λ_0 is the emission wavelength. On these spectra are visible the lower confined polaritons (LP 0D), upper confined polaritons (UP 0D), the excitonic-like lower two-dimensional polariton branch (LP 2D) and the photonic-like upper two-dimensional branch (UP 2D).

and $m = -1$ states, leading to two new states $\psi_{\pm} = \frac{1}{\sqrt{2}} [e^{+i\phi} \pm e^{-i\phi}]$. These new eigenstates feature $|2m| = 2$ lobes in the azimuthal direction, aligned along the ellipse axes, as observed in Fig. 3.5.

To go beyond this simple geometrical analysis, we need to solve the wave equation on the actual elliptical domain. This is realized in section 4.4, and allows to obtain the wavefunction patterns as well as accurate predictions for the energy splittings.

3.4 Fourier space tomography

As mentioned in section 3.2, it is possible to image the polariton emission in the Fourier space (or momentum space) instead of the real space. Using the imaging spectroscopy setup, we can record E vs $k_{//}$ diagrams in a single shot, $k_{//}$ being linked to the emission angle θ by $k_{//} = \frac{2\pi}{\lambda_0} \sin \theta$, where λ_0 is the emission wavelength.

Figure 3.10 shows the E vs $k_{//}$ diagrams for $10\mu m$ and $20\mu m$ diameter traps. Whereas the $10\mu m$ trap houses well defined discrete confined states, the $20\mu m$ trap contains a quasi-continuum which tends to form 2D polaritonic dispersion. As the excitation spot is larger than the trap, the emission of two-dimensional polaritons is also visible on the same graphs. With the same procedure than for real space imaging spectroscopy, we can perform a tomographic measurement, which provides a three-dimensional (k_x, k_y, E) view of the PL and allows to retrieve two-dimensional

distributions of the confined states in the reciprocal space (shown for a $10\mu m$ trap in Fig. 3.11). The observed PD patterns are similar to real space patterns, but differently scaled, as shown for $(n = 1, m = 0)$ and $(n = 2, m = 0)$ states in Fig. 3.11 (b). This trap is particularly asymmetric, as it is indicated by the rather large degeneracy lift of the $(n = 1, m = 1)$ state, in Fig. 3.11 (c). We measure a splitting of $75\mu eV$, comparable to the linewidth, between the two eigenstates (indicated with a green square in the figure). The PL distribution is shown for different energies (indicated in the figure by the energy difference to the lower eigenstate). Looking at the high energy spectral tail of the upper eigenstate makes it appear cleaner, as there is no more contribution from the lower eigenstate at this energy. On the other hand, at intermediate energies, the two states are mixed, recovering thus a cylindrically symmetric pattern. These two points will be of importance for the resonant excitation of single confined states in chapter 4, and for the excitation of superposition of states in chapter 5.

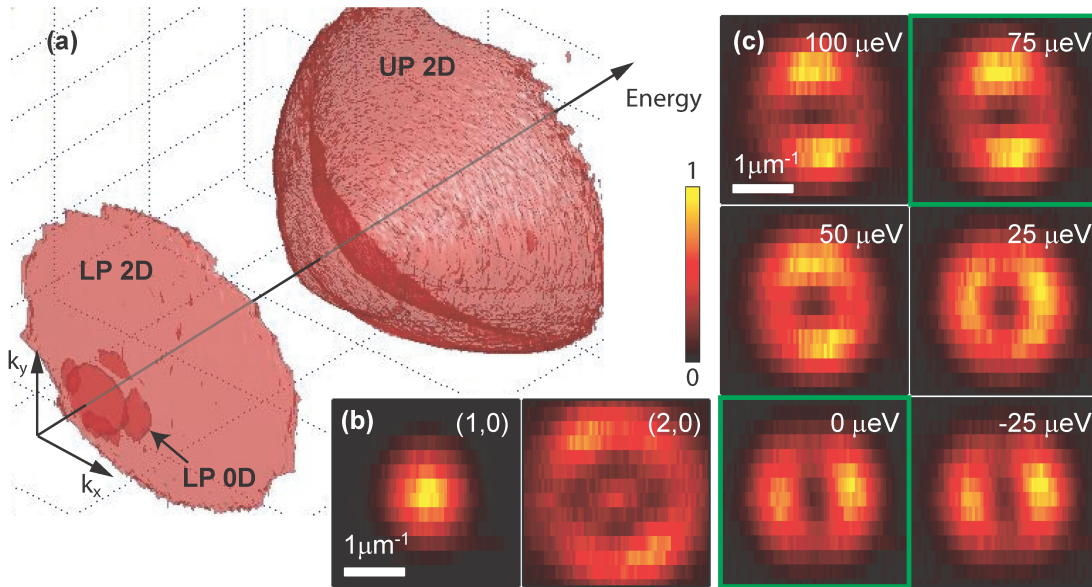


Figure 3.11: Fourier space tomography, in an elliptic trap of $10\mu m$ mean diameter. (a) (k_x, k_y, E) contour plot view of the photoluminescence. (b) Two-dimensional momentum distributions of the PL for $(n = 1, m = 0)$ and $(n = 2, m = 0)$. (c) Two-dimensional momentum distributions of the PL at different energies allow to observe a degeneracy lifting of the $(n = 1, m = 1)$ state, due to the breaking of the cylindrical symmetry. The eigenstates are indicated with green squares. The splitting being of the order of the linewidth, a mixing of the states is visible at intermediate energies. Energies are indicated with respect to the lower eigenstate energy. The PL intensity is plotted in a normalized linear color scale.

3.5 Tomography in exotic structures

While the tomographic tool allowed us to evidence deviations from the cylindrical symmetry in circular traps, it can be used with more exotic confinement potential as a true diagnosis tool. Indeed, in complicated confinement geometries, slight

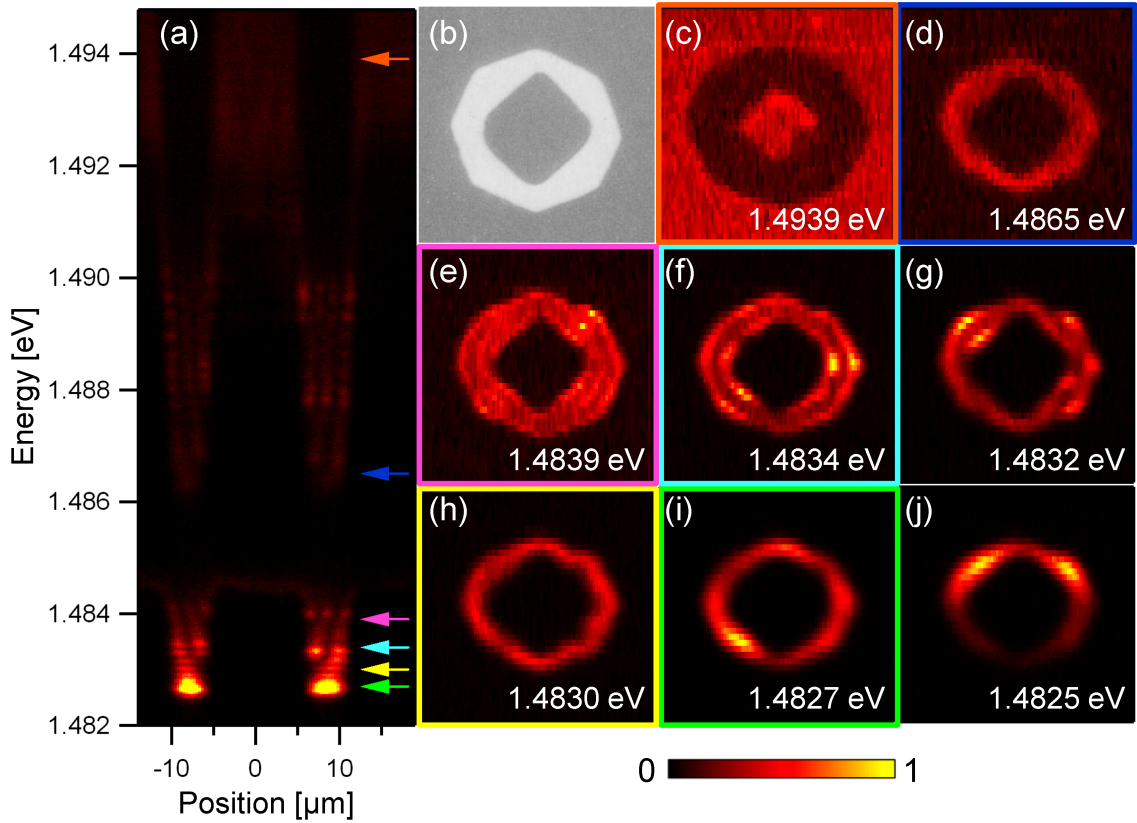


Figure 3.12: Real space tomography in a ring shaped trap. (a) Spatially resolved PL spectrum, showing several discrete levels for the upper and lower confined polaritons. PL intensity is plotted in a normalized linear color scale. (b) Photography of the mask used for the photolithography, showing that the ring structure is asymmetric. (c)-(j) Two dimensional mappings of the PL at different energies, in a normalized linear color scale. Energies of the mappings in a color square are indicated with a corresponding color arrow in (a). PL intensity is plotted in a normalized linear color scale. The mappings allow to see the PD distributions for the two-dimensional upper polariton (c), a confined UP state (d), and several confined lower polariton states (e)-(j).

variations may lead to dramatic changes in the spectrum and spatial distribution of the wavefunctions. One may want to know if the wavefunctions confined in a particular structure satisfies some geometrical properties. In the following, we are realizing tomographies in exotic structures which are present on the sample (rings and coupled structures), and show the potential of imaging spectroscopy as a diagnosis tool.

3.5.1 Rings

Ring structures are an interesting example of confinement potential. Perfectly symmetric rings are one-dimensional traps with periodic boundary conditions. However, a photography of the mask used for the etching of the ring trap, displayed in Fig. 3.12 (b), shows that the ring is asymmetric. In Fig. 3.12, the two-dimensional PD distributions obtained with the tomography technique reveal us the radial harmonics expected in a cylindrical symmetric ring (three radial harmonics can be counted

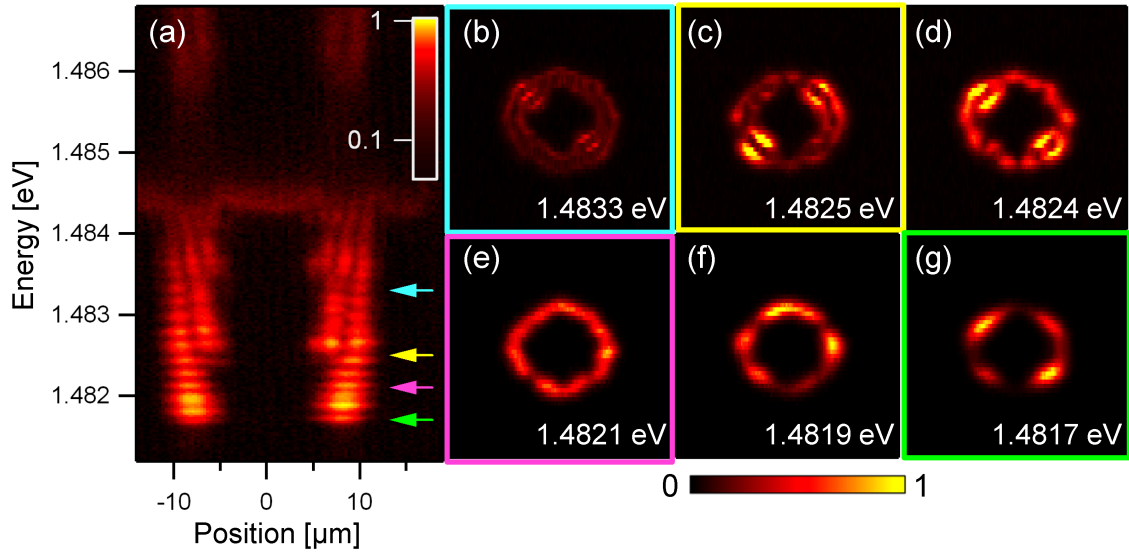


Figure 3.13: Real space tomography in a ring shaped trap, with strong azimuthal localization. (a) Spatially resolved PL spectrum, showing several discrete levels for the upper and lower confined polaritons. PL intensity is plotted in a normalized log color scale. (b)-(g) Two dimensional mappings of the PL at different energies, in a normalized linear color scale. Energies of the mappings in a color square are indicated with a corresponding color arrow in (a). This structure is supposed to be similar than the one of Fig. 3.12, as it is made using the same photolithographic mask. Different localization patterns can however be observed between this figure and Fig. 3.12. In particular, strongly localized states can be seen in (b), (c), (d), (f) and (g).

on Fig. 3.12 (e), two on Fig. 3.12 (f)). Beside this radial quantization, the spatially resolved spectrum also shows several azimuthal harmonics that arise from the periodical boundary conditions of the ring. Fig. 3.12 (h), (i) and (j) display for example three different azimuthal harmonics of the first radial harmonic. The two-dimensional PD distributions also allow to observe some localization in the azimuthal direction, as visible in Fig. 3.12 (g) and (j). Despite this observed symmetry breaking, one can see that the azimuthal localization is rather weak, and that some states like those shown in Fig. 3.12 (d),(f),(h) and (j) are nearly one-dimensional. The tomographic tool has thus allowed to fully characterize the wavefunction distribution, spatially and energetically, for that particular structure. We will show now that the tomography technique can be used to discriminate between structures that are *a priori* similar.

The same tomographic analysis is performed on a ring structure processed using the same photolithography mask, and presented in Fig. 3.13. It shows that the wavefunctions are distributed differently, and that the localization in this structure is stronger than in the structure of Fig. 3.12. In particular, the localization along two orthogonal diagonal direction of the two nearly degenerate states shown in Fig. 3.13 (c) and (d) indicates a breaking of the symmetry for $\frac{\pi}{2}$ rotations. This demonstrates the potential of imaging spectroscopy as a diagnosis tool, allowing to evidence differences in the spectrum and wavefunctions localization in *a priori* similar structures.

3.5.2 Coupled structures

Eventually we show the tomographic measurement realized on a very exotic structure, primarily intended to play the role of a Fresnel lens. The asymmetry of the photolithographic mask led however to the peculiar confinement potential which is shown in Fig. 3.14 (b). It consist in a central trap, similar to the $10\mu m$ diameter traps, surrounded by four one-dimensional curved traps. The tomographic process allows to probe the eigenstates confined in the different sub-structures. In the one-dimensional traps, several standing waves can be observed due to the finite size of the trap. The first longitudinal mode can be seen in (Fig. 3.14 (j)). Higher longitudinal modes, featuring more lobes, can be observed in Fig. 3.14 (d), (f), (g), (h) and (i) for 8, 5, 4, 3 and 2 lobes respectively. A second transverse harmonic is also shown in Fig. 3.14 (c). Looking now at the central circular trap, it is interesting to note that although it has a similar ellipticity than the standard $10\mu m$ traps of section 3.3, the splitting due to the deviation from cylindrical symmetry is much more important here, leading not only to the splitting of the $(n = 1, m = 1)$ state (Fig. 3.14 (k)-(l)), but also of the $(n = 1, m = 2)$ (Fig. 3.14 (h)-(i)). This indicates that the proximity of the one-dimensional traps influences the wavefunctions in the central trap, and constitutes an indirect proof that there is some coupling between the different sub-structures.

3.6 Conclusion

In conclusion, we have demonstrated in this chapter a method to probe the eigenstates of exciton polaritons confined in confinement potentials of different geometries. This technique offers a complete view over the spectrum as well as the distribution of the probability densities in the real and momentum spaces. It allowed to confirm that, although the confinement mechanism is initially acting of the photonic part of the polariton, the excitonic part is also confined thanks to the strong light-matter coupling. We could successfully compare the observed eigenstates with the solution of a wave equation in a cylindrical resonator, and were able to identify the effect of deviations from cylindrical symmetry. Eventually, we showed that the tomographic process can be used as a diagnosis tool for probing particular structures and exotic confinement potentials, like quasi-one-dimensional geometries or coupled structures. These technique will definitely be useful for characterizing the new structures present on the future sample, presented in chapter 9. It can also be used in the field of polariton BEC, in order to spectrally filter the condensate energy (see Ref. [11] for an example).

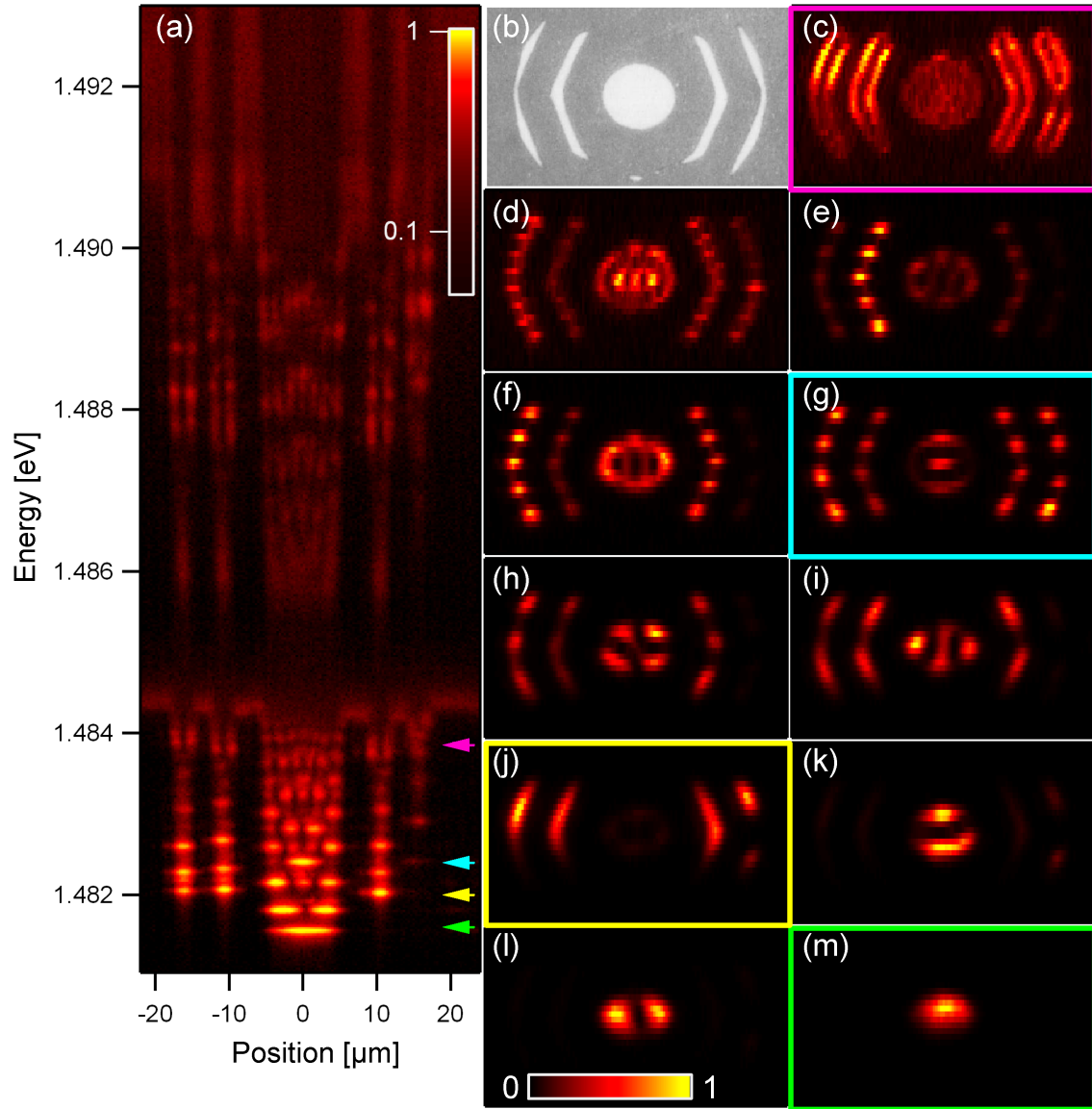


Figure 3.14: Real space tomography in an exotic coupled structure. (a) Spatially resolved PL spectrum, showing several discrete levels for the upper and lower confined polaritons. PL intensity is plotted in a normalized log color scale. (b) Photography of the mask used for the photolithography. (c)-(m) Two dimensional mappings of the PL at different energies, in a normalized linear color scale. Energies of the mappings in a color square are indicated with a corresponding color arrow in (a).

Chapter 4

Phase-resolved imaging of polariton states

4.1 Motivations

In this chapter, we are going one step further in the imaging of confined polariton states, by imaging not only the probability densities but the wavefunctions themselves. Contrarily to the tomographic technique, that allowed to image the unperturbed states under non-resonant pumping, we will this time selectively excite the confined polariton modes with a laser tuned to the polariton state energy. A homodyne detection setup is designed and used in order to retrieve the phase information of the polariton state coherent emission. We will use this tool to probe the eigenstates of the quasi-circular traps already presented in section 3.3, and show that the observed wavefunctions can be successfully compared to the standing wave patterns on an elliptical domain. Elliptical geometries are a topic of interest in optics when one wants to characterize the transverse patterns of elliptical laser beams. In this scope, Gutiérrez-Vega *et al.* have predicted and demonstrated Mathieu and Ince-Gaussian beams [81, 82, 83, 84]. However the measurement of the phase structure still remains a missing component. We will show here that the measured amplitude and phase structures of our confined microcavity polaritons are in very good agreement with analytical solutions expressed in terms of even and odd Mathieu functions. The work presented in this chapter corresponds to the following publication [85].

4.2 Phase-resolved imaging setup

We resonantly excite the polariton states (i.e. with the laser wavelength tuned to the polariton state energy, around $835nm$), using a camera objective which provides a diffraction limited spot of $\sim 15\mu m$ diameter. Thanks to a retro-reflector mounted on a lateral translation stage, we can translate the incoming laser beam on the camera objective, and thus control the excitation angle on the sample (see Fig. 4.1 (a)). A resonantly excited polariton state inherits the coherence of the excitation laser. A coherent emission pattern¹, whose intensity depends of the overlap in real space,

¹We can equivalently see the light as transmitted by the polariton modes, or absorbed and coherently re-emitted by the polariton field. However, in the microcavity polariton community,

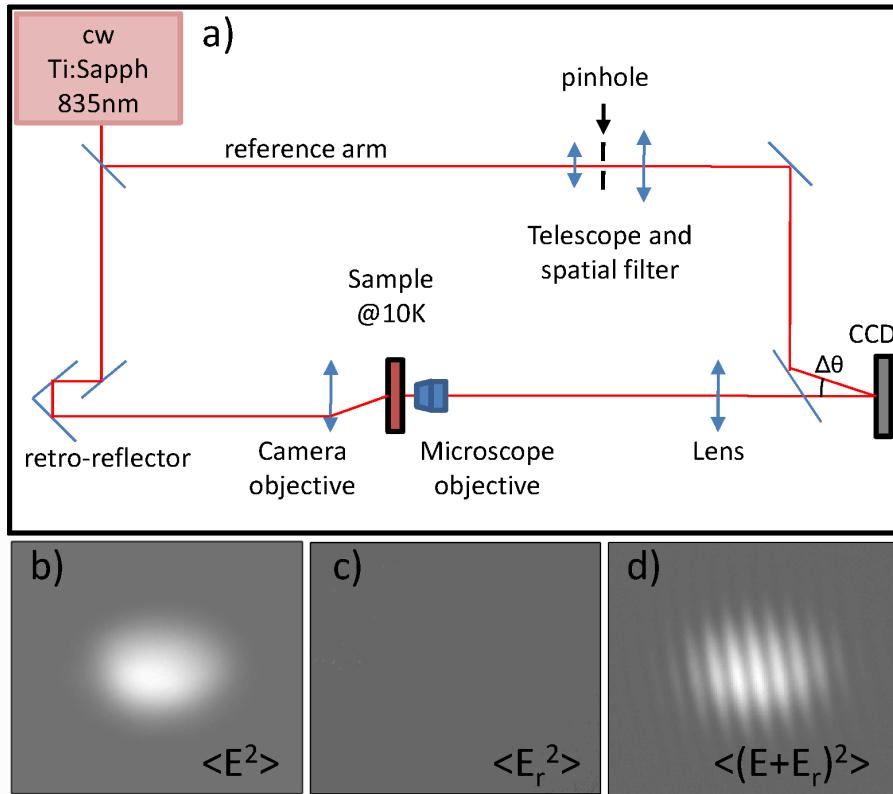


Figure 4.1: (a) Homodyne imaging setup, allowing for the retrieval of the phase information. (b) Image of the coherent emission of a $(n = 1, m = 0)$ state in a $10\mu\text{m}$ mean diameter trap. (c) Only the reference arm is sent to the CCD. (d) Coherent emission and reference interfere. The straight interference fringes come from the slight incidence angle $\Delta\theta$ of the reference arm on the CCD.

momentum space and energy between the laser field and the polariton state [86], is collected using a 0.5 NA microscope objective, and imaged on a CCD. Depending on the position of the imaging lens, real or reciprocal space images can be obtained. However, when the coherent emission is imaged on a CCD, we only have access to its intensity. We have developed a homodyne detection setup, based on a Mach-Zehnder-like interferometer, allowing to retrieve the phase information.

Let us mention that the phase-resolved measurement technique demonstrated in this chapter might also be applied to probe the eigenmodes of empty optical resonators. Indeed, although all our measurements are performed in the strong coupling regime, similar patterns would be observed for the scattering of light on empty micropillars. Let us also note that all the results of this chapter have been obtained under low power optical pumping, in the linear regime.

An image of the coherent emission of the lower polariton ground state ($n = 1, m = 0$) of a $10\mu\text{m}$ mean diameter trap is shown in Fig. 4.1 (b). In this case, only the intensity $\langle E(x, y)^2 \rangle$ of the emitted coherent field $E(x, y) \equiv E_0(x, y)e^{i\phi(x, y)}$ is detected, and the phase information is lost ($\langle \dots \rangle$ denotes the temporal average).

theoreticians commonly model the physics of microcavities using a polariton field formalism, rather than a transfer matrix formalism (see e.g. [15], or [86]), and the use of “coherent emission of polaritons” is generally admitted to refer to the resonant Rayleigh scattering.

In order to retrieve the phase information, we built a homodyne imaging setup (Fig. 4.1 (a)). The *cw* excitation laser beam is split into two parts: one part is used to resonantly excite the polariton state, the other part serves as a phase reference. The reference arm is directed through a telescope for beam enlargement and wavefront tuning. In the beam waist of the telescope is positioned a $10\mu\text{m}$ diameter pinhole for spatial filtering. The collimated reference arm is then interfered with the signal on the CCD (Fig. 4.1 (a)), with a slightly different incidence angle $\Delta\theta$, in order to provide straight² interference fringes (Fig. 4.1 (d)).

When an interferogram is recorded by the CCD camera, the detected intensity is proportional to

$$\langle (E(x, y) + E_r)^2 \rangle = \langle E(x, y)^2 \rangle + \langle E_r^2 \rangle + 2E_0(x, y)E_{r_0} \cos(\phi(x, y) - \phi_r + \Delta\Phi(x, y)), \quad (4.1)$$

where $E_r \equiv E_{r_0}e^{i\phi_r}$ is the reference field (assumed to be constant on the measurement of area). $\Delta\Phi(x, y)$ is the phase component induced by the reference arm incidence angle $\Delta\theta$:

$$\Delta\Phi(x, y) = \begin{pmatrix} k_{rx} \\ k_{ry} \end{pmatrix} \cdot \begin{pmatrix} x \\ y \end{pmatrix}, \text{ with } \left| \begin{pmatrix} k_{rx} \\ k_{ry} \end{pmatrix} \right| = \frac{2\pi}{\lambda_0} \sin(\Delta\theta). \quad (4.2)$$

The phase of the signal is not accessible from its intensity, but can be extracted from the interference term $2E_0E_{r_0} \cos(\phi(x, y) - \phi_r + \Delta\Phi(x, y))$.

Numerical retrieval of the phase information We use a numerical method, known as digital off-axis holography [87], in order to extract the phase information from the interference term. This method is depicted in Fig. 4.2. We perform a numerical Fourier transform of the interferogram. In the Fourier plane, the interference term is an off-axis contribution, while the continuous terms are situated at the origin, and can be filtered out. By this way, we filter out as well all incoherent contributions. We keep then the interference term only and perform an inverse Fourier transform, from which we obtain $E(x, y)$, including its amplitude and phase informations. The phase gradient $\Delta\Phi$ induced by the setup alignment is determined using this measurement of the $(n = 1, m = 0)$ state, shown in Fig. 4.2, as we expect a constant phase for this state. The obtained phase gradient can be used in further measurements, as it depends of the setup alignment only.

4.3 Imaging the wavefunctions in elliptical traps

We use the homodyne detection setup to image the wavefunctions in a $10\mu\text{m}$ mean diameter trap. This size is a good compromise, as the trap contains a quite important number of confined states, which are at the same time well separated in energy.

Scanning the excitation energy allows to selectively excite the eigenstates of the trap. In cylindrically symmetric systems, a linear superposition of the degenerate

²The distance between the output lens of the telescope and the pinhole needs to be finely tuned in order to obtain a flat reference phase front, and therefore straight interference fringes.

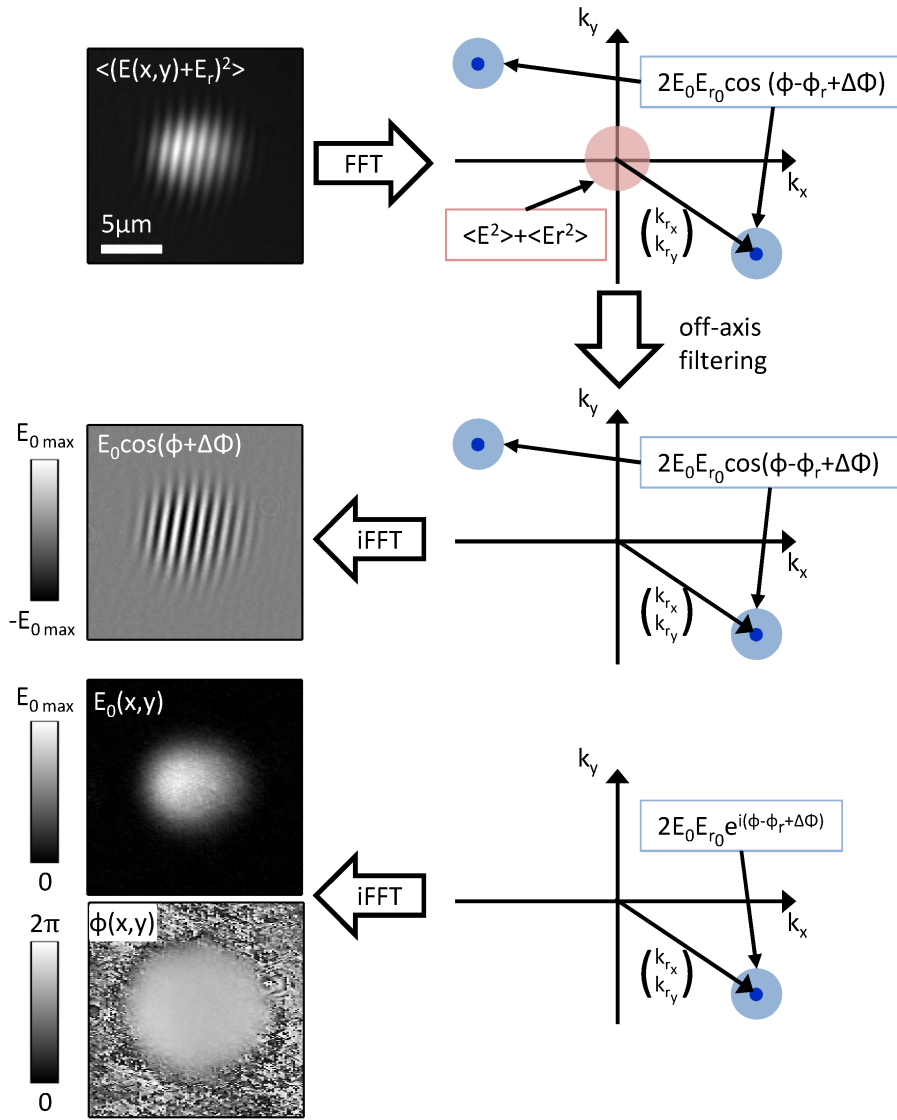


Figure 4.2: Numerical retrieval of the phase information. The fast Fourier transform (FFT) of the interferogram is central symmetric, as the interferogram is real. While the *cw* part of the emission is located at the origin of the Fourier plane, the interference term is situated around the reference arm in-CCD-plane wavevector (k_{rx}, k_{ry}) . Filtering out the continuous terms allows to retrieve the fringes of the interferogram only. Filtering out half of the Fourier plane as well allows to transform the real signal into a complex one, whose magnitude and phase are the amplitude and phase of the polariton wavefunction. The phase gradient $\Delta\Phi$ induced by the setup alignment is determined using this measurement of the $(n = 1, m = 0)$ state, as we expect a constant phase for this state. The amplitude of the reference field can either be assumed to be constant, either separately measured and eliminated from the signal.

$\pm m$ states is always excited. In that case, tuning the excitation angle and position allows to determine the contribution of the $+m$ and $-m$ states in the superposition. This point will be discussed in detail in chapter 5. Now, in slightly elliptical traps, where the eigenstates are no longer the $\pm m$ states, it is possible to take advantage of the degeneracy lift ΔE between the new eigenstates. In very elliptical traps, these

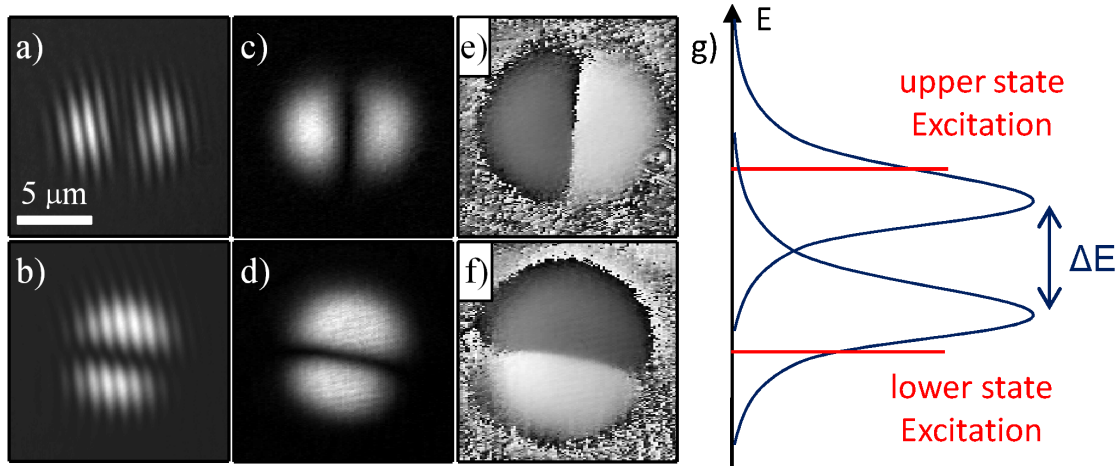


Figure 4.3: (a)-(b) Real space coherent emission of the ($n = 1, m = 1$) lower polariton doublet state in a $10\mu\text{m}$ mean diameter mesa, interfered with the reference beam. (c)-(d) Amplitude and (e)-(f) phase of the state wavefunctions, extracted using off-axis filtering. In (e) and (f), a clear π -phase shift is visible between the two lobes, indicating that the two lobes of the wavefunction are of opposite sign. The combination of the amplitude and phase information provides a full information on the confined polariton wavefunction. Interferograms and amplitude patterns are in a linear gray scale from minimal (black) to maximal (white) intensity. Phase patterns are in a linear gray scale from 0 (black) to 2π (white). (g) Selective excitation technique. Slightly red or blue-shifting the excitation energy allows to excite only one of the nearly degenerate doublet, even if the energy splitting is smaller than the linewidth.

eigenstates would be well separated in energy, and easy to excite selectively. In the $10\mu\text{m}$ traps, though, the degeneracy lift ΔE is of the order or smaller than the linewidth. In this case, one can slightly red-shift or blue-shift the excitation energy with respect to the doublet energy, in order to selectively excite the upper or lower energy state, respectively, as depicted in Fig. 4.3 (g) (the FWHM of the laser is smaller than our resolution limit of $25\mu\text{eV}$).

As a result, we can measure the coherent emission of the eigenstates of the elliptical trap. The resulting interferograms for the ($n = 1, m = 1$) doublet are presented in Fig. 4.3 (a)-(b), and the corresponding numerically extracted amplitude and phase in Fig. 4.3 (c)-(d) and (e)-(f), respectively³. The phase structure shows a clear π -phase shift between the two lobes of the wavefunction, indicating that the two lobes are of opposite sign with respect to each other. We have therefore succeeded in measuring the full wavefunction, and not its squared magnitude only.

Using the selective excitation technique depicted in Fig. 4.3 (g) allows to probe the higher energy eigenstates as well. We have seen in section 3.3.2 that, even if less pronounced than for the ± 1 states, there should be a finite coupling between the $m = +2$ and $m = -2$ states. This is what we actually observe on the states characterized by the quantum numbers ($n = 1, m = 2$), presented in the first two rows of Fig. 4.4. Moreover, a significant qualitative deviation from the patterns

³The phase-gradient $\Delta\Phi$ induced by the reference arm incidence angle is determined from the measurement of the ground state presented in Fig. 4.2.

expected in a circular geometry is observed on the low energy state presented in the first row.

In order to understand this feature, we need to solve the wave equation on the actual elliptic domain. The two-dimensional wave equation is a Helmholtz equation

$$\nabla^2\psi + k^2\psi = 0 \quad (4.3)$$

whose eigenvalues k^2 are proportional to the energy of the eigenmodes ψ . In terms of the elliptical coordinates (ξ, η) , variables can be separated and one obtains two equations known as the angular and radial Mathieu equations [88]⁴. Each of them has two families of independent solutions, namely the even and odd Mathieu functions. The complete two-dimensional even (odd) solutions, analogous to the standing wave patterns of a vibrating membrane, are then given by the product of the angular even (odd) Mathieu function by the radial even (odd) Mathieu function [89, 90, 91]. These eigenstates are also characterized by two quantum numbers, which also provide the number of zeros in the radial and azimuthal directions, respectively. For these reasons we will still use the quantum numbers n and m , and indicate the parity of the state (e.g. $(n = 1, m = 2, e)$ for the $(n = 1, m = 2)$ even state), to describe the eigenstates. These eigenstates should not be confused with the $(n, \pm m)$ states, which were eigenstates of the circular trap. The even and odd two-dimensional solutions of Mathieu equations for the quantum numbers $(n = 1, m = 2)$ have been computed, and are presented in the two first rows of Fig. 4.4, in front of the corresponding experimental patterns. We have used the elliptical semi-axes measured on the photolithography mask for defining the confinement geometry (with a Dirichlet condition). There is an excellent qualitative agreement between these analytical solutions and the experimentally observed patterns, for both the phase and the amplitude. It can be observed that the nodal lines of the wavefunctions follow confocal ellipses ($\xi = \text{constant}$) and hyperbolas ($\eta = \text{constant}$). Several confined states from the same trap are presented in Fig. 4.4, and an excellent overall agreement between the experimentally observed patterns and the analytical solutions is observed as well.

Solving the wave equation on the elliptical domain also allows to obtain a theoretical energy spectrum. The most straightforward physical approach is to describe the system with the time-independent Schrödinger equation, as shown in section 3.3.2. The eigenvalues k of equation (4.3) are then related to the physical parameters by $k^2 = \frac{2m_{LP}E}{\hbar^2}$, where m_{LP} is the effective mass of the polariton and E is the eigenenergy with respect to the bottom of the confinement potential. However, using these physical parameters, the experimental spectrum cannot be satisfactorily reproduced. This is probably due to the two following reasons: first, with the Dirichlet condition, we have assumed an infinite potential barrier created by the trap, whereas the effective confinement potential for the lower polariton is finite, of the order of $3meV$; second, as discussed in section 3.3.2, the effective mass of the polariton depends of the detuning of the given polariton mode with respect to the excitonic resonance, and is therefore different for each confined polariton mode. Using the approach developed in [69, 70], consisting in first solving the Maxwell equation to find the confined optical modes and then strongly coupling these modes

⁴Mathieu equations and their resolution are detailed in the next section 4.4.

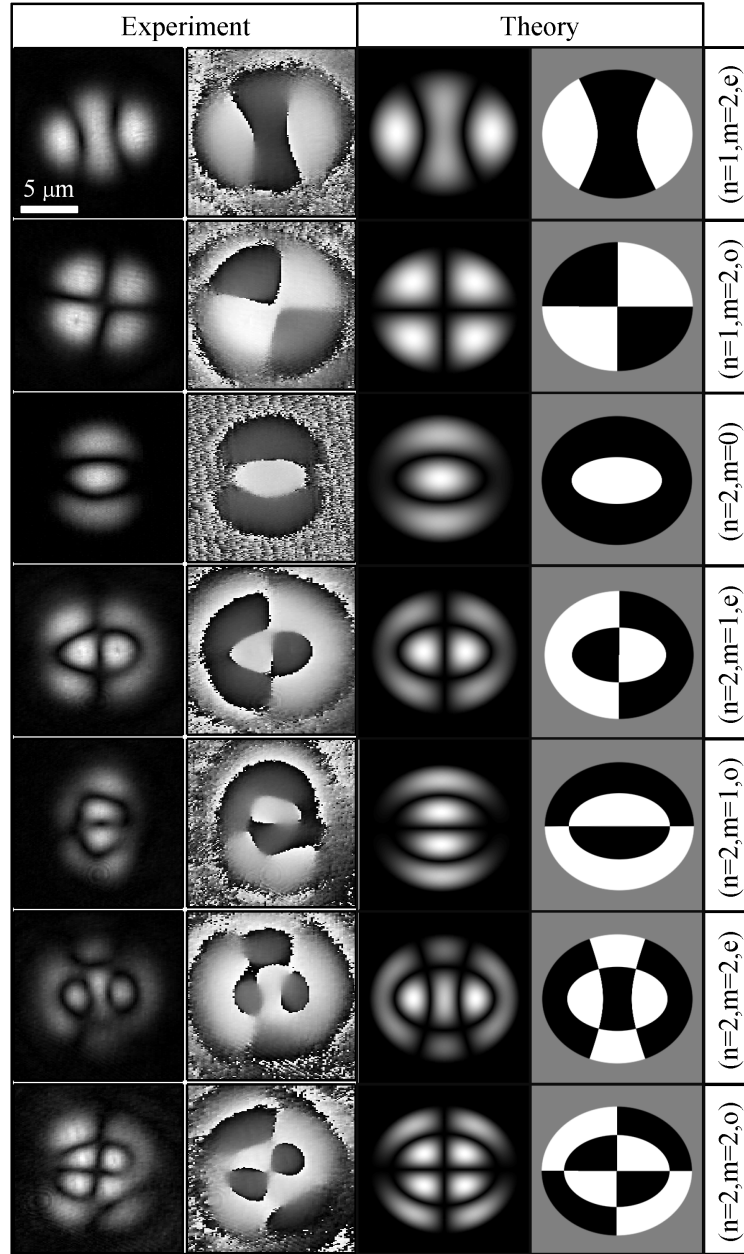


Figure 4.4: First two columns: real space experimental images of the amplitude and phase of several states confined in a $10\mu m$ trap. The phase-gradient reference used is the one that provides a constant phase for the $(n = 1, m = 0)$ state of the trap. Amplitude patterns are in a linear gray scale from minimal (black) to maximal (white) intensity. Phase patterns are in a linear gray scale from 0 (black) to 2π (white). Last two columns: Corresponding amplitude and phase structures obtained from the analytical solutions of the wave equation. The amplitude structures are given by the absolute value of the wavefunction. For the phase structures, black is plotted for the negative parts of the wavefunction and white for the positive parts.

to the exciton , would allow to overcome the issue of the variable effective mass, but not of the finite potential boundary. Taking into account the finite size of the confinement potential would require to use the evanescent Radial Mathieu Func-

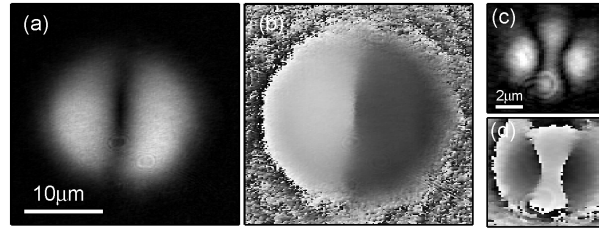


Figure 4.5: (a)-(b) Experimental amplitude and phase emission patterns measured when the $(n = 1, m = 1, o)$ state in a $20\mu m$ mean diameter trap is dominantly excited. (c)-(d) $(n = 1, m = 2, e)$ upper polariton state in a $3\mu m$ mean diameter trap. Amplitude patterns are in a linear gray scale from minimal (black) to maximal (white) intensity. Phase patterns are in a linear gray scale from 0 (black) to 2π (white). The round shape at the bottom of (c) and (d) is an experimental artifact due to a dust particle on the CCD.

tions (RMF) of the second kind Ke_m and Ko_m . Nevertheless, without going further into the physical modeling of the system in order to obtain absolute values for the eigenenergies, we can learn qualitative information about the splitting between the even and odd states with respect to the quantum numbers (n, m) . The computation of the RMF (see Fig. 4.8) indicates that for a given n , the energy splitting between the even and odd states is higher for $m = 1$ than for $m = 2$. Using the values for the elliptical axes a and b measured from the photolithography mask for $10\mu m$ traps, we find through the computation of the RMF a splitting of $48\mu eV$ for the $(n = 1, m = 1)$ doublet and of $31\mu eV$ for the $(n = 1, m = 2)$ doublet. These values are in very good agreement with the values generally measured for $10\mu m$ traps ($\sim 50\mu eV$ and $\sim 30\mu eV$ respectively).

Let us also mention that the phase-resolved imaging of confined states can also be realized in different trap sizes, and for the upper polariton states as well, as shown in Fig. 4.5. For the larger traps ($20\mu m$ mean diameter), featuring a quasi-continuum of states (and a smaller ellipticity), it is difficult to selectively excite a single state, as the energy spacing between the neighbor states is very small. However, it is possible to excite dominantly a given state, as shown for the $(n = 1, m = 1, o)$ state of Fig. 4.5 (a)-(b).

Eventually, it is also possible to image the polariton emission in the Fourier plane. Interference of reciprocal space images with the reference arm provides the same type of interferograms than for real space imaging, from which we can extract amplitude and phase of the wavefunctions as well. A series of reciprocal space patterns for four different states in a $10\mu m$ trap is presented in Fig. 4.6. We can see that patterns in the Fourier plane are very similar than real space patterns, except for the fact that higher-order diffraction is visible around the zero order pattern. The homodyne detection allows to observe the expected π -phase shift between two consecutive diffraction orders.

4.4 Mathieu equations and functions

In this section we show the tools that we used to plot the eigenmodes of the polaritons confined in elliptical traps. A detailed description of the method can also be found

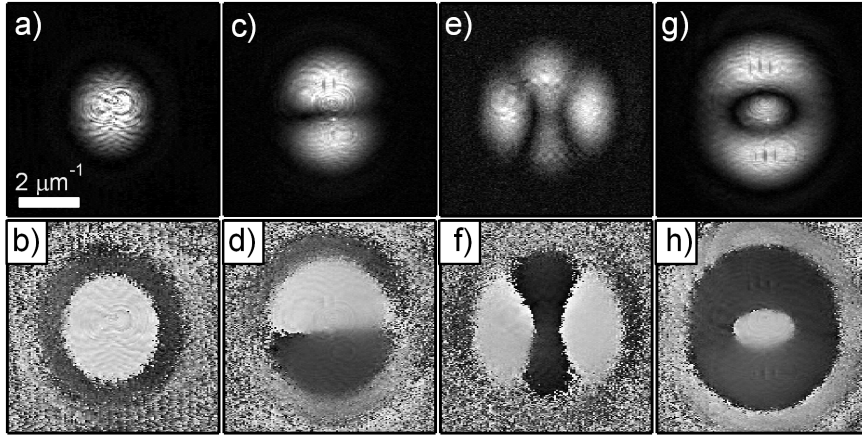


Figure 4.6: Experimental amplitude and phase patterns in the Fourier plane, for the (a)-(b) ($n = 1, m = 0$) state, (c)-(d) ($n = 1, m = 1, e$) state, (e)-(f) ($n = 1, m = 2, e$) state and (g)-(h) ($n = 2, m = 0$) state, in a $10\mu m$ trap. Higher diffraction orders can be seen around the main patterns. Amplitude patterns are in a linear gray scale from minimal (black) to maximal (white) intensity. Phase patterns are in a linear gray scale from 0 (black) to 2π (white). The small vertical lines that one can see on the amplitude patterns are measurement artifacts, due to the saturation of the CCD.

in Ref [90], and a comprehensive overview of Mathieu functions is available in Ref [91].

In order to find the eigenmodes of polaritons confined in an elliptical trap, we need to solve the Helmholtz equation (4.3) in elliptical coordinates (ξ, η) , which are linked to Cartesian coordinates by

$$x = \frac{c}{2} \cosh \xi \cos \eta \quad (4.4)$$

$$y = \frac{c}{2} \sinh \xi \sin \eta \quad (4.5)$$

where c is the distance between the two foci of the ellipse, and is given by $\frac{c}{2} = \sqrt{a^2 - b^2}$, with a and b the semi-major and semi-minor axes of the elliptical confinement, respectively (see Fig. 4.7 (a)). The eccentricity ϵ of an elliptical domain is

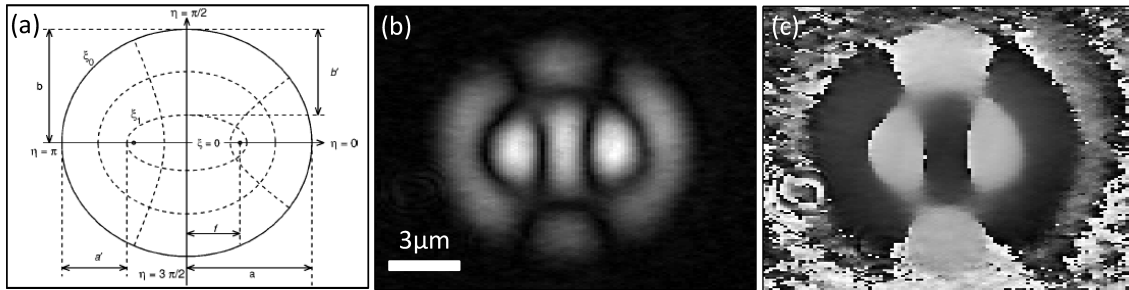


Figure 4.7: (a) Elliptical coordinate system (reproduced from [91]). Ensembles of points with $\xi = \text{const}$ represent confocal ellipses, and ensembles of points with $\eta = \text{const}$ represent confocal hyperbolas. (b) and (c) Comparison with the experimentally observed amplitude and phase patterns of a ($n = 2, m = 2, e$) state in a $10\mu m$ mean diameter trap shows that the wavefunction nodal lines follow constant elliptical coordinates.

given by $\epsilon = \frac{c}{2a}$. The domain boundary is defined by $\xi = \xi_0$, such as $a = \frac{c}{2} \cosh \xi_0$ or $b = \frac{c}{2} \sinh \xi_0$. Ensembles of points with $\xi = \text{const}$ represent confocal ellipses, and ensembles of points with $\eta = \text{const}$ represent confocal hyperbolas. After performing the separation of variables $\psi = R(\xi)\Phi(\eta)$, one obtains two equations:

$$\frac{d^2\Phi}{d\eta^2} + (d - 2q \cos 2\eta)\Phi = 0, \quad (4.6)$$

$$\frac{d^2R}{d\xi^2} - (d - 2q \cos 2\xi)R = 0, \quad (4.7)$$

where $q = \frac{1}{16}c^2k^2$ and d is a separation variable. Equation (4.6) is known as the ordinary or angular Mathieu equation and equation (4.7) as the modified or radial Mathieu equation. Solutions of the angular Mathieu equation (4.6) form two independent families of solutions, the even and odd angular Mathieu functions (AMF)

$$\Phi_m = \begin{cases} ce_m(\eta, q), & m = 0, 1, 2, \dots, \quad (\text{even AMF}) \\ se_m(\eta, q), & m = 1, 2, 3, \dots, \quad (\text{odd AMF}) \end{cases} \quad (4.8)$$

where m is the order of the function. The AMF satisfy the periodic boundary conditions on $\eta \in [0, \pi]$, and features m zeros on this interval. Solutions of the radial Mathieu equation (4.7) which satisfy the continuity conditions at $\xi = 0$ are the even and odd radial Mathieu functions (RMF) of the first kind

$$R_m = \begin{cases} Je_m(\eta, q), & m = 0, 1, 2, \dots, \quad (\text{even RMF}) \\ Jo_m(\eta, q), & m = 1, 2, 3, \dots, \quad (\text{odd RMF}) \end{cases} \quad (4.9)$$

In order to find the eigenmodes of the Helmholtz equation (4.3) we need to find the values of q that satisfy the Dirichlet condition:

$$Je_m(\xi_0, q) = 0 \text{ or } Jo_m(\xi_0, q) = 0 \quad (4.10)$$

There is an infinite family of solutions $q_{n,m}$ that satisfy this condition. We denote $qe_{n,m}$ and $qo_{n,m}$ the n^{th} zero of Je_m and Jo_m , respectively. Figure 4.8 displays $Je_m(\xi_0, q)$ and $Jo_m(\xi_0, q)$ ⁵ for $m = 0, 1, 2$, where the elliptical boundary $\xi_0 = 1.2931$ is obtained using the major axis $2a = 10.78$ and minor axis $2b = 9.27$ measured on the photolithography mask for a $10\mu\text{m}$ trap, providing an eccentricity of $\epsilon = 0.51$. To every $q_{n,m}$ can be associated an eigenvalue k , solution of the Helmholtz equation (4.3), that can be linked to a frequency or energy by using the physical parameters of the problem. The even and odd eigenmodes are given by the product of radial and angular Mathieu functions:

$$\psi e_{n,m} = Je_m(\xi, q)ce_m(\eta, q), \text{ with } q = qe_{n,m} \quad (4.11)$$

$$\psi o_{n,m} = Jo_m(\xi, q)se_m(\eta, q), \text{ with } q = qo_{n,m}. \quad (4.12)$$

Even and odd AMF and RMF, as well as the even and odd eigenmodes resulting of their product, are plotted in Fig. 4.9 for quantum numbers $n = 1$ and $m = 2$ in a $10\mu\text{m}$ mean diameter trap.

⁵Numerical evaluation of the Mathieu functions was obtained using the *specfun* package, available on www.mathworks.com.

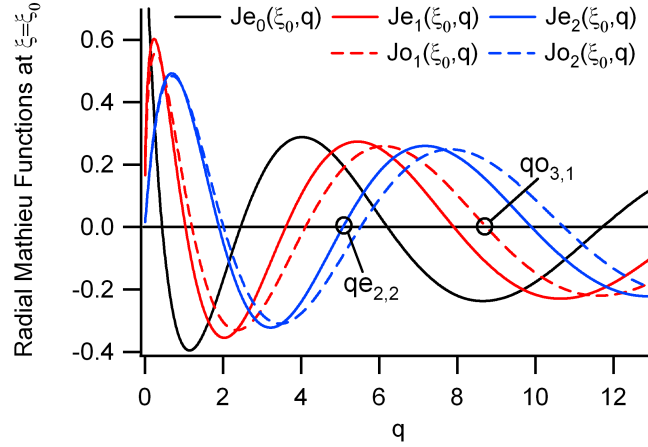


Figure 4.8: Plot of the even and odd Radial Mathieu Functions (RMF) $Je_m(\xi_0, q)$ and $Jo_m(\xi_0, q)$, as a function of the parameter q , at the boundary of the potential trap ($\xi_0 = 1.2931$), for $m = 0, 1, 2$. The parameter q of the eigenmodes satisfying the Dirichlet condition are given by the zeros of the RMF. $qe_{n,m}$ and $qo_{n,m}$ are the n^{th} zero of the even and odd RMF of order m . The energies or frequencies of the eigenmodes are proportional to q . We can see that for a given n , the energy splitting between the even and odd states is higher for $m = 1$ than for $m = 2$. For a given order m , the energy splitting is increasing with n .

4.5 Conclusion

To summarize, we have developed in this chapter a homodyne detection setup that allows for the imaging in real and reciprocal space of the complete wavefunction patterns (amplitude and phase) of microcavity polaritons. We have used this setup to record images of polariton states confined in the elliptical traps of a patterned microcavity. We could observe very clearly the effects of the ellipticity of the confining potential on the wavefunction patterns, which were successfully compared to analytical solutions described in terms of even and odd solutions of Mathieu equations.

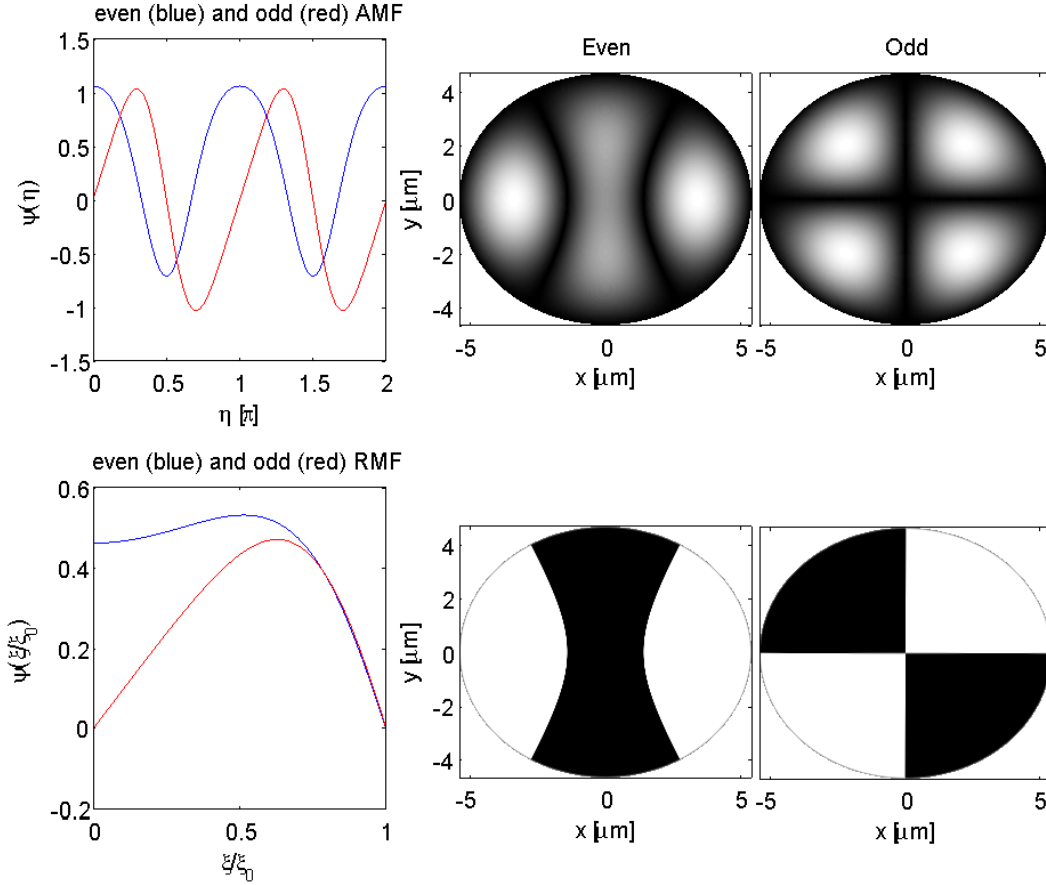


Figure 4.9: Plot of the even and odd angular Mathieu functions (AMF) and radial Mathieu functions (RMF), as well as the even and odd eigenmodes resulting of their product, for quantum numbers $n = 1$ and $m = 2$ and the parameters of a $10\mu\text{m}$ mean diameter trap. The AMF satisfy the periodic boundary conditions on $\eta \in [0, \pi]$, and features m zeros on this interval. The RMF satisfies $Je, o_m(\xi_0, q) = 0$ and the continuity conditions at $\xi = 0$.

Chapter 5

Selective excitation of confined polariton vortices

5.1 Motivations

In the following chapter, we are showing that it is possible to excite superpositions of confined polariton states in the quasi-circular traps. We are demonstrating that tuning the excitation conditions allows to control the resulting emission pattern. In particular, selective excitation of integer orbital angular momentum states is shown, with control over the sign and the value of the orbital charge m . The homodyne imaging setup allows us to evidence the phase singularity which characterizes these states featuring the topology of vortices. In the scope of the exploitation of polariton states in confined geometries for logical applications [19, 20], it is interesting to see to which extent confined polariton wavefunctions can be tailored. Moreover, in the context of the extremely active research on polariton vortices [10, 92, 11, 93, 94, 95, 96, 97], this example also shows that vortices in the polariton field can be created in the linear regime, by pure geometrical means. It confirms that quantized polariton vortices in themselves are not a demonstration of any superfluid behavior. The work presented in this chapter corresponds to the following publications [85, 98].

5.2 Poincaré sphere representation of the degenerate state

Generation of optical vortices has been demonstrated in different types of lasers like ring resonators [99], diode lasers [100] and Vertical Cavity Surface Emitting Lasers (VCSELs) [101]. They have been identified as the transverse modes of cylindrically symmetric optical resonators and often called the TEM_{01} “donut” mode, which can be obtained as a superposition of the TEM_{10} and TEM_{01} modes [102, 103]. As we mentioned it in the previous chapters, there is, in cylindrically symmetric systems, a two-fold degeneracy between states of opposite angular orbital momentum m . Using resonant excitation, one creates a coherent superposition of the $+m$ and $-m$ states (hereafter denoted $|m_+\rangle$ and $|m_-\rangle$). The superposition of these two counter-propagating waves gives rise to the formation of a standing wave in the

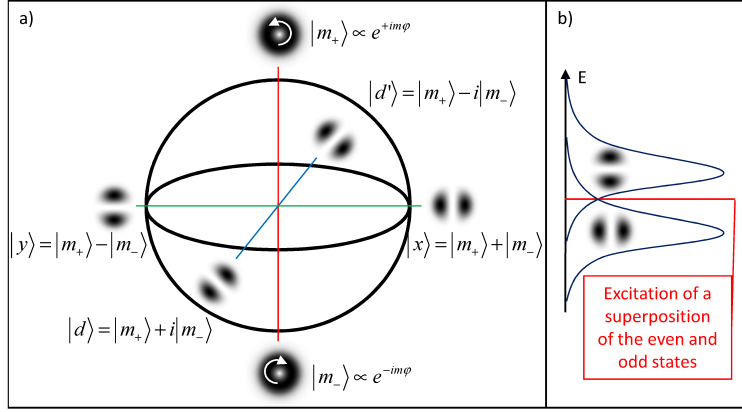


Figure 5.1: (a) Poincaré sphere representation of the degenerate ($n = 1, m = 1$) state. Coherent superpositions (with equal weights) of the integer angular momentum states $|m_+\rangle$ and $|m_-\rangle$ yields to a two-lobe pattern, whose orientation depends of the relative phase between $|m_+\rangle$ and $|m_-\rangle$. For this $m = 1$ state, the same Poincaré sphere can be used to represent the elliptical case, for which $|x\rangle$ and $|y\rangle$ are the even and odd eigenstates. (b) This scheme shows how it is possible to overcome the cylindrical symmetry breaking by exciting a superposition of the even and odd eigenstates, when their energy splitting is of the order of or smaller than the linewidth.

azimuthal direction, or , in other words, to a wavefunction pattern made of $|2m|$ lobes. This degenerate structure can be represented in a Poincaré sphere picture (Fig. 5.1 (a)), where we can see that the lobes can be aligned along any direction, depending of the relative phase between the $|m_+\rangle$ and $|m_-\rangle$ states. Now, we have seen in chapter 4 that in our elliptical structures, $|m_+\rangle$ and $|m_-\rangle$ are no longer the eigenstates, and there is an energy splitting between the new even and odd eigenstates. However, when this splitting is of the order of or smaller than the state linewidths, the ellipticity can be overcome by exciting at an intermediate energy, as depicted in (Fig. 5.1 (b)). In this way, both eigenstates are excited, allowing for the recovering of all the states depicted in Fig. 5.1 (a) -including $|m_+\rangle$ and $|m_-\rangle$ -, which can be seen as superpositions of the even and odd eigenstates. This situation is a geometrical analogy with transverse laser patterns, where the TEM_{01*} mode can be obtained as a superposition of the TEM_{10} and TEM_{01} modes[104, 105]. For the quantum number $m = 1$, the even and odd eigenstates feature two-lobe patterns which are similar to the $|x\rangle$ and $|y\rangle$ states of Fig. 5.1 (a). The same Poincaré sphere can therefore be used to describe the $|m_+\rangle$, $|m_-\rangle$, $|d\rangle$ and $|d'\rangle$ states in terms of superpositions of $|x\rangle$ and $|y\rangle$ ¹.

In the following, as the ellipticity of the system is overcome by the excitation scenario of Fig. 5.1 (b), we chose to express the created superpositions in the $(|m_+\rangle, |m_-\rangle)$ basis. The superposition reads thus as:

$$|\psi\rangle = A|m_+\rangle + B|m_-\rangle \quad (5.1)$$

where A and B are complex coefficients. The value of coefficients A and B is given

¹This is however not valid for larger m , where the shape of the eigenstates are qualitatively modified by ellipticity, as it was showed in chapter 4. We will show in section 5.4 that in this case a superposition of the even and odd states does not allow to recover pure $|m_+\rangle$ and $|m_-\rangle$ states.

by the overlap (in real space, reciprocal space and energy) between the $\pm m$ states and the pump field. It is therefore possible to tailor the emission pattern by tuning the excitation angle and spot position with respect to the trap. For example, it is shown in Ref. [86] that directing the excitation beam on the trap and rotating the excitation angle around the optical axis yields to a rotation of the emission pattern in the momentum space. This corresponds to a rotation on the equator of the Poincaré sphere of Fig. 5.1 (a).

5.3 Excitation of vortex states

We are now going to show that by carefully selecting certain pumping conditions one can also recover the $|m_+\rangle$ and $|m_-\rangle$ states, carrying an integer angular orbital momentum. First of all, we show how such a state is characterized using our homodyne imaging setup. Fig. 5.2 shows a $(n = 1, m = +1)$ state in a $10\mu\text{m}$ mean diameter trap. In the interferogram displayed in Fig. 5.2 (a), one can observe a very clear fork-like dislocation, indicating the presence of a phase singularity. We extract from this interferogram the amplitude (Fig. 5.2 (b)) and phase (Fig. 5.2 (c)) of the polariton field. The two characteristics of quantized vortices are observed: the intensity minimum at the center of the trap (b) and the 2π -phase shift around the core (c) are straightforwardly visible. The core of this vortex is situated at the center of the trap, and the size of the vortex is delimited by the mesa diameter. This state is geometrically analogous to a TEM_{01} “donut” transverse laser mode.

In order to create such a state, one needs to find excitation conditions to maximize the coupling of the laser field with the $|m_+\rangle$ state only, and minimize the coupling with $|m_-\rangle$. This can be done by focusing the excitation laser on the side of the trap, with a finite excitation angle, such as only the spatial tail of the excitation spot is reaching the trap. This corresponds to injecting polaritons with a well defined in-plane momentum mainly on one side of the trap. Such a technique can be used to select which one of the $+m$ or $-m$ state is injected. The excitation angle must lie in the momentum space extension of the vortex state, i.e. around 5° for a $10\mu\text{m}$ trap.

Depending on the side of the trap on which the laser is focused, the charge is going

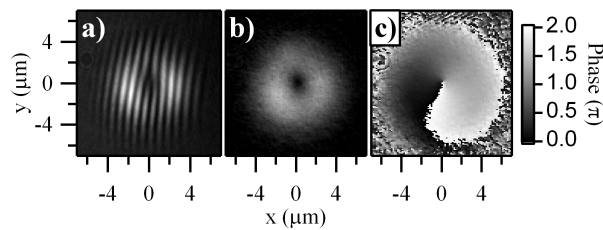


Figure 5.2: (a) Interferogram resulting from the interference of the coherent emission of the $(n = 1, m = +1)$ state of the lower polariton with the reference laser, displaying a clear fork-like dislocation. (b) Amplitude of the coherent polariton field, extracted from (a), showing a minimum in the field density at the place of the phase singularity. (d) Phase of the coherent polariton field, extracted from (a), indicating a 2π -phase shift rotation of the phase around the singularity.

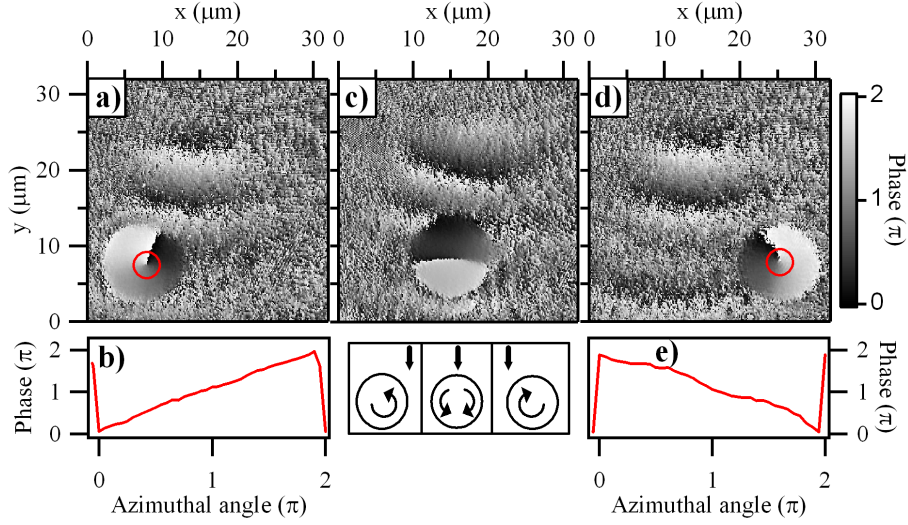


Figure 5.3: (a) Phase mapping and (b) phase distribution profile along the red circle of the polariton field, when the polaritons are injected on the right side of the trap using a pump incidence angle of 4.8° . In this configuration, the vortex is rotating counterclockwise. The position and in-plane momentum of the exciting spot are experimentally indicated by the faint phase signal present beside the trap. (d)-(e) Same as (a)-(b), but injection on the left side of the mesa. In this configuration, the vortex is rotating clockwise. (c) Phase mapping when the polaritons are injected in front of the trap. In this case, both counter-propagating vortices are excited, giving rise to a two-lobe wavefunction pattern. Insets: schematic views of the vortex rotation for the three situations, the pump and its in-plane direction are represented by the thick arrow.

to be positive or negative, as demonstrated in Fig. 5.3, using a finite excitation angle of 4.8° . In this figure, the excitation energy and incidence angle are kept constant, and the position of the excitation spot with respect to the trap is laterally shifted. The phase distribution (Fig. 5.3, (a),(c) and (d)) and the phase profile along the red circle (Fig. 5.3, (b) and (e)) are displayed when the trap is positioned on the left side (Fig. 5.3 (a)-(b)) or right side (Fig. 5.3 (d)-(e)) of the excitation spot. When the trap is positioned in front of the excitation spot (Fig. 5.3 (c)), exciting $|m_+\rangle$ and $|m_-\rangle$, a two-lobe pattern is observed, as a result of the superposition of the two states. The lateral movement of the excitation spot position with respect to the trap thus corresponds to a trajectory along a meridian of the Poincaré sphere of Fig. 5.1.

Note- We would like here to point out a very peculiar detail, that we noticed only very recently, when preparing the figures of this thesis. The rotation of the vortex, as observed in Fig. 5.3 (a) and (d), is going in a counter-intuitive way. The intuition would say that, analogously to water injected into a circular swimming pool, the vortex should rotate in the same way than the external in-plane momentum applied on the trap edge. It is the opposite that is observed here. We do not know at this stage why the observed result does not follow this simple intuitive explanation. What we are sure of (because we tried a large number of positions of the trap with respect to the excitation spot), is that the vortices are systematically rotating in the same direction when positioned on one side of the excitation spot, and systematically in

the other direction when positioned on the other side. The main point of the chapter, which is the selectivity of the vortex charge, is therefore still valid. However, the selection mechanism has to be clarified, in order to understand why the simple (and maybe naive?) picture of the injection of a fluid on the trap edge is not valid. New experiments as well as numerical simulations are going to be undertaken in this perspective.

5.4 Higher angular orbital momentum states

It is also possible to excite states of angular orbital momentum, by tuning the excitation energy to be resonant with a state carrying another quantum number m . For larger m , however, the shape of the even and odd eigenstates are qualitatively modified by the ellipticity of the trap. This has for result that the superposition of the even and odd eigenstates does not yield to a multiply charged vortex. Figure 5.4 shows the superposition of $(n = 1, m = 2, e)$ and $(n = 1, m = 2, o)$. The expected double topological charge is split into two single vortices, due to the ellipticity of the trap. The positions of the two cores are given by the intersections of the nodal lines of the $(n = 1, m = 2, e)$ and $(n = 1, m = 2, o)$ state patterns (shown in Figure 5.4).

While most of the traps feature a similar shape and ellipticity, some of them are different due to local inhomogeneities in the photolithography mask deposition and/or structural defects in the sample. We were able to find a trap with an effective nearly cylindrical symmetry, providing a doubly charged vortex for the $(n = 1, m = 2)$ state. This state is presented in Fig. 5.5, where a trident-like dislocation is visible in the interferogram, resulting in 4π -phase shift when circumventing a single density minimum.

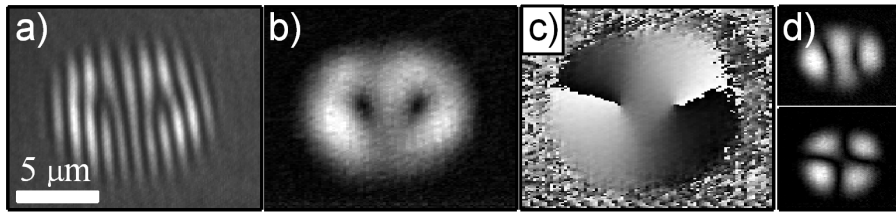


Figure 5.4: (a) Interferogram resulting from the interference of the coherent superposition of $(n = 1, m = 2, e)$ and $(n = 1, m = 2, o)$ states with the reference laser. (b) and (c) Corresponding amplitude and phase structures, respectively. The double topological charge is split into two due to the ellipticity of the trap. The two phase singularities of this “eight” shape are located at the intersections of the nodal lines of the $(n = 1, m = 2, e)$ and $(n = 1, m = 2, o)$ states (shown in (d), not to scale). Interferogram and amplitude pattern are in a linear gray scale from minimal (black) to maximal (white) intensity. Phase pattern is in a linear gray scale from 0 (black) to 2π (white).

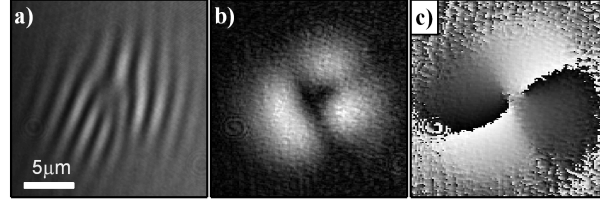


Figure 5.5: (a) Interferogram resulting from the interference of the coherent emission of the lower polariton second excited state ($n = 1, m = +2$) in a nearly cylindrical trap with the reference laser, displaying a trident-like dislocation. (b) and (c) Amplitude and phase mapping extracted from (a), displaying a doubly charged vortex structure. Interferogram and amplitude pattern are in a linear gray scale from minimal (black) to maximal (white) intensity. Phase pattern is in a linear gray scale from 0 (black) to 2π (white).

5.5 Vortex non-linearities

All the measurements presented until now in this chapter were performed in the low excitation density regime. Increasing the pump power by three orders of magnitude (up to $32\mu W/\mu m^2$) allowed us to observe the effect of polariton-polariton interactions in the form of a blue-shift of the vortex state of the order of $120\mu eV$ (Fig. 5.6 (a)). In this measurement, the laser energy was tuned in order to follow the blue-shift of the vortex state.

Another effect of polariton-polariton interactions on vortices should be a dependency of the vortex core size with interaction energy[94]. Indeed, the vortex core size should be of the order of the polariton gas healing length ξ , which depends on the interaction energy E_{int} as $\xi = \frac{\hbar}{\sqrt{2mE_{int}}}$, where m is the polariton effective mass (see Section 7.2.2 for the derivation of this formula). However, the size of our vortices is in our case limited, even in the linear regime, by the confinement potential geometry (a core diameter of $\sim 3\mu m$ is measured in the $10\mu m$ mean diameter traps). On the range of excitation power used in our experiment, we never observed any change in the vortex core size in $10\mu m$ traps. Fig. 5.6 (b) and (c) shows that there is no difference in the vortex core diameter between the linear regime and the highest excitation power available. This result is consistent with a recent publication by Krizhanovskii *et al.* [94], where the effect of interactions on a polariton vortex imprinted using an optical parametric oscillator (OPO) process was investigated. In this paper, a reduction of the vortex core diameter down to $6\mu m$ when increasing the excitation density up to $40\mu W/\mu m^2$ was reported. A quantitative estimation of the healing length for our experimental conditions can also be performed by assuming that the interaction energy is given by the blue-shift of the polariton line. Using our maximal blue-shift of $120\mu eV$, we find a healing length of $\xi = 1.6\mu m$, which is of the order of the measured $\sim 3\mu m$ diameter vortex cores. As we could not use higher excitation power, we tried to exploit the different trap sizes available on our sample. Indeed, vortices can be created in the small traps ($3\mu m$ mean diameter) and large traps ($20\mu m$ mean diameter traps) as well. A vortex in a large trap is shown in Fig. 5.7, for a low excitation density, featuring a core diameter of $\sim 4.2\mu m$. In these large traps, we did observe some reduction of the vortex core size while increasing the pump power, but these results were not fully reproducible. The main reason

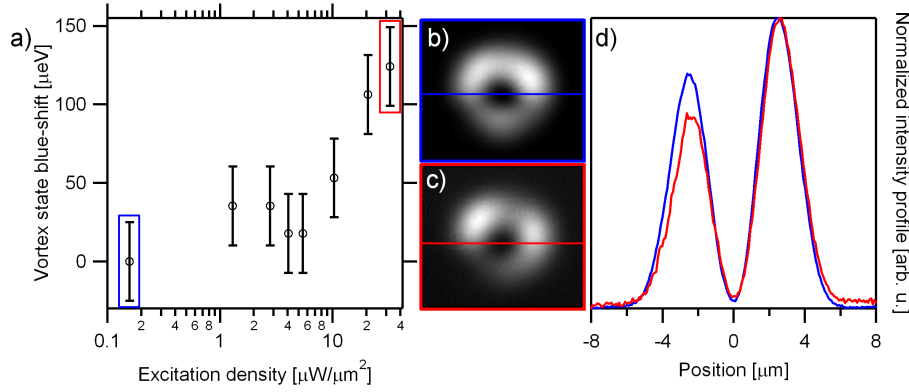


Figure 5.6: (a) Blue-shift of the polariton vortex state in a $10\mu\text{m}$ diameter trap, with respect to excitation density. The laser energy is tuned to follow the vortex state blue-shift. Error bars are given by the spectral resolution limit of $25\mu\text{eV}$. (b)-(c) Amplitude patterns, in a linear gray scale from minimal (black) to maximal (white) intensity, for the lower excitation density (blue square) to the larger excitation density (red square). (c) Line profiles along the blue (red) lines in (b)-(c) are plotted for the lowest (highest) excitation density. No change in the vortex core diameter can be observed.

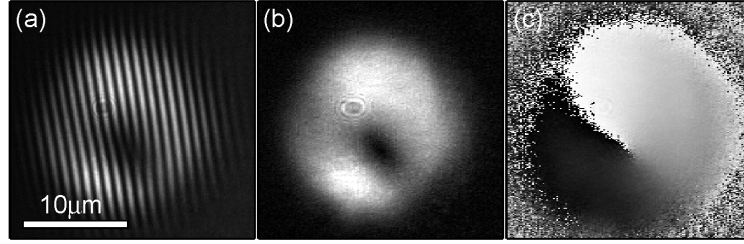


Figure 5.7: (a) Interferogram, (b) Amplitude pattern and (c) phase pattern of a vortex in a $20\mu\text{m}$ mean diameter trap, for a low excitation density. Interferogram and amplitude pattern are in a linear gray scale from minimal (black) to maximal (white) intensity. The phase pattern is in a linear gray scale from 0 (black) to 2π (white).

is the experimental difficulty of tuning the excitation laser energy for exciting the vortex state, while this latter is blue-shifting and is very close energetically to other confined states.

5.6 Conclusion

In conclusion, we have demonstrated the selective excitation of trapped polariton states in a patterned semiconductor microcavity. Thanks to the homodyne detection setup, the phase and the amplitude of the coherent light-matter gas were directly visualized, and trapped polariton vortices were identified as a superposition of eigenstates of the quasi-circular traps. We have experimentally shown the selection of the vortex charge by tuning the excitation conditions. A splitting of the double vortex charge into two vortices for the quantum number $m = 2$ has been observed as a consequence of trap ellipticity. This work shows the essential role of engineered lateral confinement for the topological tailoring of the coherent emission pattern of an

exciton-polariton gas resonantly excited using a Gaussian laser field. This work may possibly provide new exploitation schemes for polariton lasers made of cylindrical micropillars [22].

Chapter 6

Oscillations between vortex and anti-vortex states

6.1 Motivations

In the following chapter we are considering the case where the confined polariton states are not continuously driven by the laser frequency (like a forced oscillator), but are excited with a laser pulse and let free to evolve. In this situation, when a single confined state is excited (in the linear regime), it will simply decay with a characteristic decay time given by the polariton lifetime. On the other hand, when a superposition of states is excited, their phase oscillations at different frequencies will give rise to a time evolution of their interference pattern. In the following, we are focusing on the excitation of the nearly degenerate $(n = 1, m = 1)$ state in a $10\mu m$ mean diameter trap. Adding a time resolution to the homodyne imaging setup, we are showing that the time evolution of the coherent superposition of the even and odd eigenstates $(n = 1, m = 1, e)$ and $(n = 1, m = 1, o)$ yields to an oscillation between vortex and anti-vortex states. This phenomenon is remarkably well described within the Poincaré sphere representation of the $(n = 1, m = 1)$ state.

6.2 Time resolved homodyne imaging setup

In order to observe the time evolution of the wavefunction pattern, we need to develop a time-resolved setup. A solution already used in different groups is to image the polariton emission on the slit of a streak camera, which provides the time evolution of one axis of the image plane with a resolution of $\sim 4ps$. Shifting the position of the image plane across the streak camera slit allows to recover the dynamics of the system in two dimensions [106, 107]. In this case, if one wants to retrieve the phase information, a stabilized interferogram must be imaged on the slit of the streak camera, as in Refs. [96, 108, 109].

In our case we use a different setup, based on the Mach-Zehnder interferometer presented in chapter 4. We have added a delay line on the excitation arm (see Fig. 6.1 (a)), and use from now on a mode-locked Ti:Sapph laser, which provides $12nm$ -broad, $80fs$ -long pulses at a repetition rate of $80MHz$. Creating a polariton population with the excitation pulse, we can probe the polariton dynamics by vary-

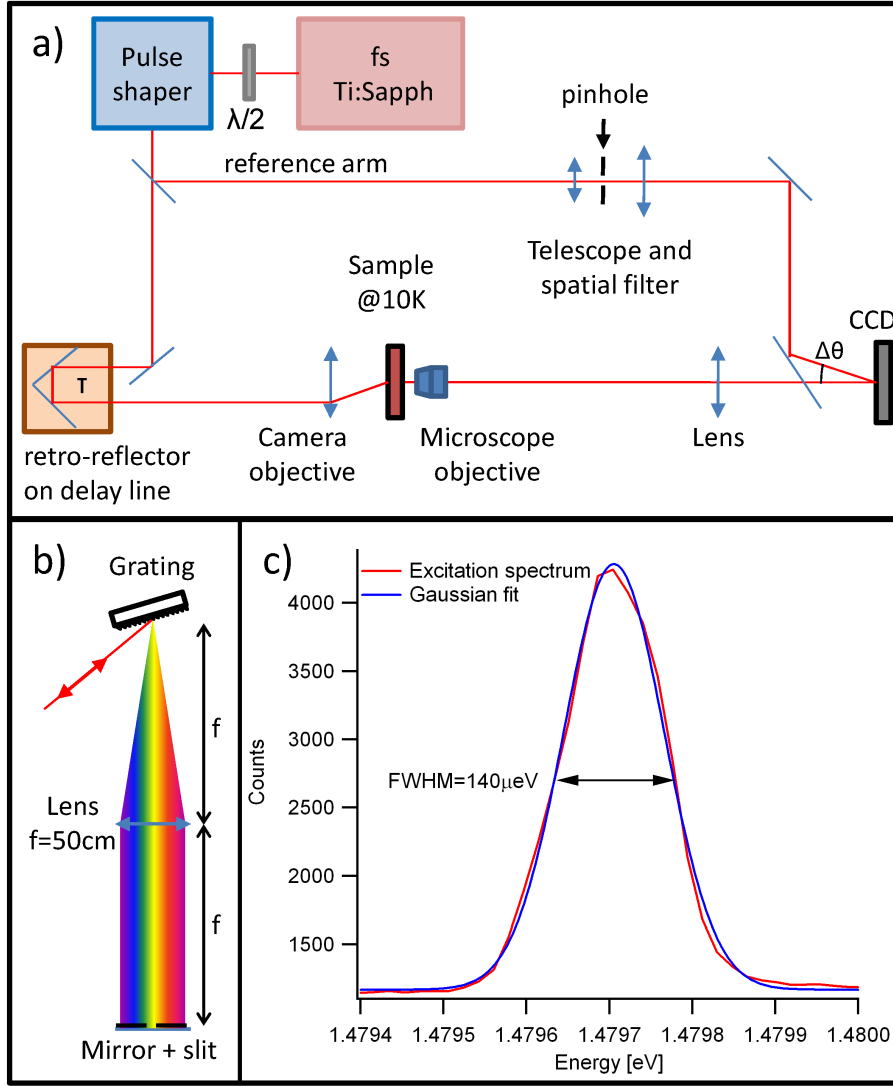


Figure 6.1: (a) Time and phase resolved imaging setup, based on a Mach-Zehnder interferometer, similarly to the phase resolved setup shown in Fig. 4.1. In order to obtain the time resolution, a mode-locked Ti:Sapph laser is used, and a delay line allows to scan the delay between excitation and reference pulses. A pulse shaper is added for the spectral tailoring of the laser pulse. It is preceded by a $\lambda/2$ waveplate, that allows for the rotation of the laser linear polarization, in order to maximize the output power of the polarization sensitive pulse shaper's grating. (b) Detail of the pulse shaper, containing a 1200 lines/mm blazed grating, a 50cm focal length lens, a $75\mu\text{m}$ wide slit and a mirror. (c) Spectrum of the laser pulse at the pulse shaper output, showing a nearly Gaussian $140\mu\text{eV}$ -broad pulse.

ing the delay τ between the excitation and reference pulses. Indeed, the reference pulse will interfere on the CCD only with the coherent emission emitted at τ . By this way we obtain a time-resolved imaging setup, with an intrinsic phase resolution, without using a streak camera. The time resolution of the setup is given by the temporal length of the reference pulse.

Pulse shaping In order to selectively excite the trapped polariton states, we need to spectrally tailor the excitation pulse. We built a pulse shaper (see Fig. 6.1 (b)) consisting in a 1200 lines/mm blazed grating, a 50cm focal length lens, a 75 μ m wide slit and a mirror. The laser pulse is dispersed by the grating, and spectrally filtered by the slit. It is then sent back through the same optical elements, in order to compensate for the pulse dispersion. We use a spherical lens, so as the outcoming beam is vertically shifted from the the incoming and can be conveniently separated and injected into the Mach-Zehnder interferometer. As the grating is polarization sensitive, a $\lambda/2$ waveplate is placed before the pulse shaper, and allows to rotate the laser polarization for optimizing the output power. A spectrum of the outcoming pulse is shown in Fig. 6.1 (c). The pulse FWHM is measured to be 140 μ eV, and has a nearly Gaussian shape. This allows us to estimate¹ the pulse length to be 13ps, which will be the time resolution of the interferometric measurements.

6.3 Oscillations between vortex and anti-vortex states

We use the 140 μ eV broad pulse obtained from the pulse shaper to excite a superposition of the even and odd eigenstates resulting from the slight ellipticity of a 10 μ m mean diameter trap (the eigenstates linewidths are $\sim 80\mu$ eV and the splitting between the even and odd states has been measured to be $\Delta E = 50 \pm 25\mu$ eV). Very generally, instead of imposing the oscillation frequency, as it was the case with a *cw* laser in chapters 5 and 4, we create a coherent superposition which is then free to evolve.

It is very convenient to represent again the superposition in a Poincaré sphere (Fig. 6.2 (a)). We place the eigenstates ($n = 1, m = 1, e$) and ($n = 1, m = 1, o$) on the vertical axis, and their possible superpositions on the equator of the sphere. As the two eigenstates oscillate with different frequencies, their relative phase will constantly change with time, leading to an evolution of the wavefunction pattern. This evolution can be very easily pictured in the Poincaré sphere representation as a rotation of the state vector of the system (in purple on Fig. 6.2 (a)) around the eigenaxis at a frequency $\omega = \frac{\Delta E}{\hbar}$. This periodical oscillation is analogous to the Rabi oscillations observed when a superposition of upper and lower polaritons is created, or to the spatial oscillations observed between two coupled wells when a superposition of the symmetric and antisymmetric eigenstates is created.

Once a polariton population is injected by the excitation pulse, the time evolution of the coherent emission can be probed by scanning the delay τ between excitation and reference pulses. From the recorded interferograms, digital off-axis filtering (see section 4.2 for details) allows to extract the amplitude and phase of the coherent polariton field $\Psi(x, y, \tau)$ emitted at the delay τ . We show on Fig. 6.2 (b) the spatially integrated amplitude $|\Psi|$ of the coherent emission with respect to the interferometer delay. It can be seen that after the injection by the ~ 13 ps long pulse, the polariton population $|\Psi|^2$ decays with a characteristic decay time of $\tau = 15.7 \pm 0.3$ ps. Images

¹For a chirpless, Gaussian pulse, the time-bandwidth product is ~ 0.44 . See e.g. Encyclopedia of Laser Physics and Technology, http://www.rp-photonics.com/gaussian_pulses.html

of the coherent emission, at the delays indicated by vertical black lines and letters (i)-(v) in Fig. 6.2 (b), are shown in Fig. 6.2 (c), (d) and (e). The fringes of the interferogram (in a saturated color scale) are displayed in (c), the emission field amplitude in (d) and the emission field phase in (e).

In the first column (i) the polariton injection is shown. It displays a diagonal state $|d\rangle$, indicating that a well balanced (i.e. with similar weights) superposition of $(n = 1, m = 1, e)$ and $(n = 1, m = 1, o)$ is created. Columns (ii) to (v) show the free evolution of the polariton field emission pattern, with an interval between each picture of $\sim 25ps$. A decrease of the signal intensity is observed with time, due to the finite polariton lifetime measured in (b). The polariton emission patterns passes from a vortex state (rotating counterclockwise, with a fork-like dislocation oriented downwards) in (ii), a $|d'\rangle$ state (orthogonally aligned with respect to the $|d\rangle$ state of (i)) in (iii), an anti-vortex state (rotating clockwise, with a fork-like dislocation oriented upwards) in (iv), and a diagonal state $|d\rangle$ again in (v). The system state vector has therefore made a full rotation along the Poincaré sphere equator. The rotation period is $T \sim 4 \times 25ps = 100ps$ (with a $\sim 13ps$ resolution), corresponding to an oscillation frequency of $\sim 10GHz$. It allows to estimate for this trap the energy splitting between $(n = 1, m = 1, e)$ and $(n = 1, m = 1, o)$: $\Delta E = \hbar\omega = \hbar\frac{2\pi}{100} = 41 \pm 5\mu eV$, in agreement with the $50 \pm 25\mu eV$ generally measured with spatially resolved spectroscopy.

6.4 Conclusion

In conclusion, we have presented in this chapter a time and phase resolved imaging setup, based on Mach-Zehnder interferometry, that allows to probe the dynamics of coherent superpositions of confined polariton states. In particular, a periodical oscillation between vortex and anti-vortex states has been evidenced in elliptic polariton traps. The observed phenomenon is remarkably well described by a rotation of the system state vector around the eigenaxis in the Poincaré sphere representation of the $(n = 1, m = 1)$ state. The measured oscillation frequency of $\sim 10GHz$ corresponds to the energy splitting between the eigenstates of the elliptical trap.

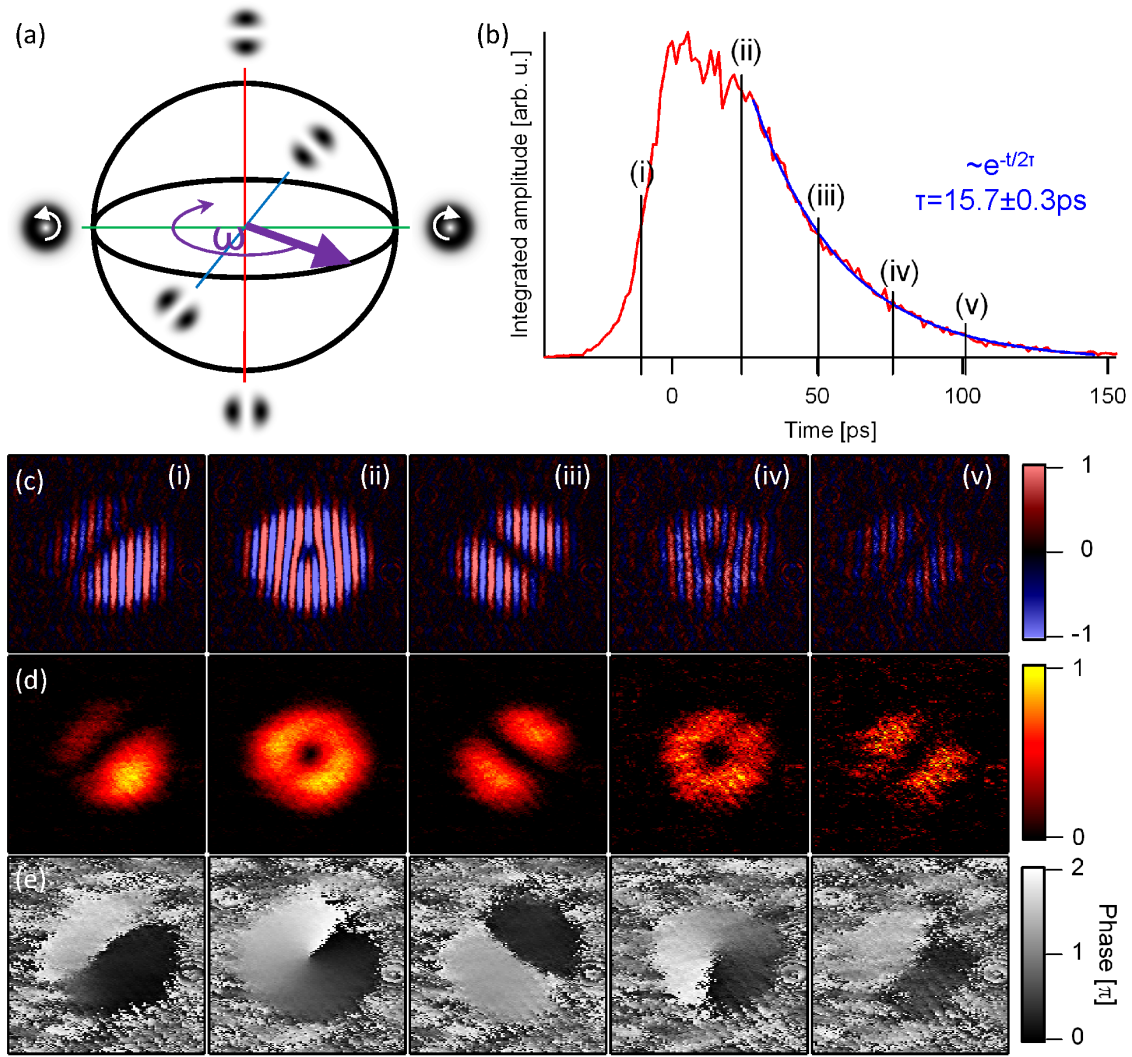


Figure 6.2: (a) Poincaré sphere representation of the nearly degenerate ($n = 1, m = 1$) state in a quasi-circular trap. The eigenstates resulting from the trap ellipticity correspond to the poles of the sphere, and their equally weighted superpositions are located on the equator. The type of superposition depends of the phase difference between the eigenstates. The most typical superpositions, which are the vortex, anti-vortex and diagonal states are shown on the picture. The time evolution of a superpositions can be pictured as a rotation of the state vector (in purple) around the eigenaxis, at a frequency $\omega = \frac{\Delta E}{\hbar}$, where ΔE is the energy splitting between the eigenstates. (b) Amplitude $|\Psi|$ of the polariton coherent field, spatially integrated over the whole polariton emission, versus time. The time zero is given by the estimated zero delay between excitation and reference pulses. In blue: a mono-exponential fit allows to extract the decay time 2τ of the polariton field amplitude $|\Psi|$. It gives a decay time τ for the polariton population $|\Psi|^2$ of $\tau = 15.7 \pm 0.3 \text{ ps}$. The fringes of the interferogram (in a saturated color scale) are displayed in (c), the emission field amplitude in (d) and the emission field phase in (e). The different columns show snapshots of the time evolution of the emission pattern, at times indicated with vertical black lines and a corresponding letter (i)-(v) in (b). This evolution is very well explained by a rotation of the system state vector along the equator of the Poincaré sphere shown in (a).

Part III

Polariton fluid dynamics

Chapter 7

Quantum Turbulence in a polariton fluid

7.1 Motivations

In this chapter we are exploiting our time-resolved homodyne imaging setup to address polariton fluid dynamics. Indeed, our measurement technique is very advantageous to study two-dimensional polaritons, as it allows not only to probe the propagation of a polariton wavepacket in the microcavity plane, but also to extract the fluid velocity from the phase gradient. Even more interestingly, the phase resolution allows to unambiguously detect vortices in the polariton flow, and therefore to address the physics of quantum turbulence in the polariton fluid. The theoretical study of turbulence in quantum gases has triggered a lot of interest in the physics community [110, 111, 112, 113, 114, 115, 116], but only few experiments were able to directly address the role played by vortices in the phenomenon [117, 118, 119]. The observation of turbulence in a microcavity is therefore a major experimental step following the demonstration of polariton superfluidity [16]. In the following sections we experimentally study a polariton fluid flowing past an obstacle, and report on the nucleation of quantized vortex pairs in the wake of the obstacle. Images of the nucleation mechanism and of vortex migration along the flow will be presented, demonstrating the potential of semiconductor microcavities for the study of turbulence in quantum fluids. Combining measurements of the dynamics in the real space and the momentum space allows to associate the nucleation mechanism with a slow down of the polariton fluid, as a result of the interaction of the excitation spectrum with the obstacle. The nucleation conditions in terms of local fluid density and velocity on the obstacle perimeter will be discussed. Eventually, it will be shown that the experimental results can be reproduced by the numerical resolution of the generalized Gross-Pitaevskii equation (GPE) which include the non-equilibrium character of the polariton fluid. The experiments of this chapter are realized on the same sample than the one of the preceding chapters, but in the planar region surrounding the traps. The position on the sample is chosen such as the exciton-photon detuning is close to zero for the extended two-dimensional polaritons.

7.2 Framework

7.2.1 Turbulence in classical fluids

Hydrodynamic instabilities in classical fluids have been studied in the pioneering experiments of Bénard in the 1910'. Convective Bénard-Rayleigh flows and Bénard-Von Kármán streets are now well known examples in non-linear and chaos sciences [120], and are of crucial practical importance as well in fields ranging from meteorology to hydroelectric machinery [121]. In conventional fluids, the flow around an obstacle is characterized by the dimensionless Reynolds number $R_e = \frac{vR}{\nu}$, with v and ν the fluid velocity and dynamical viscosity, respectively, and R the diameter of the obstacle. When increasing the Reynolds number, laminar flow, stationary vortices, Bénard-Von Kármán streets of moving vortices and fully turbulent regimes are successively observed in the wake of the obstacle [120].

7.2.2 Superfluidity and turbulence in quantum gases

In quantum gases, such as liquid helium or Bose-Einstein condensates, the situation is different from the classical case in many points of view. First, due to the quantization of circulation, vortices in a coherent gas ought to be quantized [122]. Second, in superfluid systems, the Reynolds number cannot be defined due to the absence of viscosity. It is however only true when the Landau criterion is fulfilled, i.e. when the fluid velocity v is smaller than the speed of sound in the system c_s [123]. In superfluid Helium, evidences have been given for the appearance of dissipation above a critical velocity, but only indirect measurements have addressed the role played by vortices in the friction mechanism [113].

Experiments in ultra-cold atomic gases also allowed to observe a critical velocity, when moving an obstacle through the condensate, under which a frictionless flow was observed [124, 125]. For condensates moving at a velocity greater than the speed of sound ($v > c_s$) and hitting an obstacle, the appearance of Čerenkov radiations, analogous to the sound shock wave emitted by supersonic airplanes, is observed. This radiation is well reproduced by the numerical resolution of GPE [126]. The relationship between critical velocity and turbulence in quantum gases has been first theoretically addressed using GPE in the work by Frisch *et al.* [110], where the nucleation of quantized vortices in the wake of a cylindrical obstacle has been observed for fluid velocities below the Landau criterion, as a friction mechanism. In this pioneering work, where a steady homogeneous flow is assumed, the appearance of drag on the obstacle is accompanied by the emission of vortices, down to a critical fluid velocity of $\sim 0.4c_s$. Frisch *et al.* link this critical value to a local increase of the fluid velocity in the vicinity of the impenetrable obstacle: the vortices are emitted when the fluid velocity on the obstacle perimeter is larger than the speed of sound. Considering a local velocity on the obstacle perimeter v two times larger than the fluid velocity far from the obstacle v_∞ , the critical velocity is found to be $\frac{v_\infty}{c_s} = \sqrt{\frac{2}{11}} \sim 0.43$.

On the experimental side the most promising observations of the role played by vortex nucleation in the friction process have also been realized in atomic condensates [127,

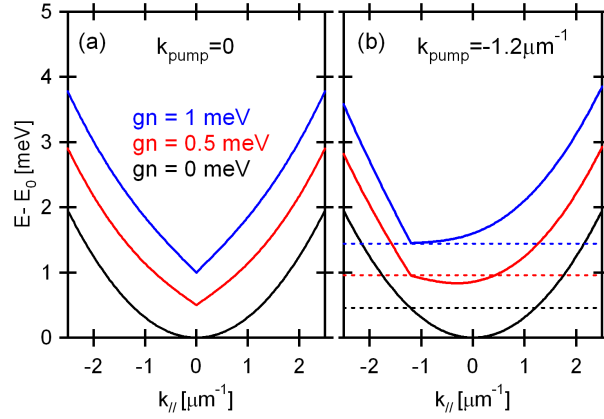


Figure 7.1: **Bogoliubov excitation spectra** (a) Plots of the excitation spectra, according to eq. 7.1, for $m = 0.7 \text{ meV} \cdot \text{ps}^2 \cdot \mu\text{m}^{-2}$ and $gn = 0$ (black curve), $gn = 0.5 \text{ meV}$ (red curve) and $gn = 1 \text{ meV}$ (blue curve). E_0 is the polariton energy at $k_{||} = 0$ in the non-interacting limit ($gn = 0$). (b) Same as in (a), but with an applied Galilean boost, as defined in eq. 7.3, with $k'_{||} = -1.2 \mu\text{m}^{-1}$. The intersections of the dotted lines with the dispersion indicate the possibilities of Rayleigh scattering. The blue curve depicts a superfluid regime and features a Mach number smaller than one ($\frac{v}{c_s} < 1$). The red curve depicts a Čerenkov regime, for which the Mach number is greater than one ($\frac{v}{c_s} > 1$).

117, 118, 119]. However, no experiment has allowed to image the nucleation mechanism with a phase resolution so far.

7.2.3 Superfluidity and turbulence in microcavities

The recent demonstration of superfluidity of an exciton polariton gas [16] offers a very advantageous tool to explore quantum turbulence. Predicted by Ciuti & Carusotto [14, 15], polariton superfluidity can be probed by resonantly injecting a coherent polariton population with a *cw* laser and monitoring the resonant Rayleigh scattering (RRS). Due to polariton-polariton interactions, pumping resonantly the polariton branch strongly modifies the excitation spectrum.

Bogoliubov excitation spectrum The following theory allows to describe superfluidity as defined by the Landau criterion (originally established for liquid Helium [128]) for a gas of weakly interacting bosons [123]. Let us consider the generalized Gross-Pitaevskii equation, restricted to the lower polariton branch¹, as given in section 1.5 by eq. 1.17. A parabolic dispersion $\epsilon(k_{||}) = \frac{\hbar k_{||}^2}{2m}$ is assumed, with a lower polariton effective mass m defined by eq. 1.11. The blue-shift ΔE of the polariton mode is given by the interaction energy $\Delta E = gn$, with g the polariton-polariton interaction constant and $n \equiv |\psi|^2$ the polariton density. Considering an homogeneous driving laser field and translational invariance ($V_C = V_X = 0$), eq. 1.17 can be linearized around its steady state solution. The resulting Bogoliubov excitation spectrum for a polariton branch resonantly driven at $k_{||} = 0$ is then given by [14, 15]

¹This assumption is valid only if the upper polariton branch is not excited. It will be shown further how we experimentally take care of this point.

$$E(k_{//}) = E_0 \pm \sqrt{(\epsilon(k_{//}) + 2gn) \epsilon(k_{//}) + gn}, \quad (7.1)$$

where E_0 is the polariton energy at $k_{//} = 0$ in the non-interacting limit. The linewidths have been neglected here for the sake of simplicity. The \pm corresponds to the so-called *normal* (+) and *ghost* (−) branches, which are symmetric with respect to each other. The normal and ghost branches can be seen as the ensemble of signal and idler states resulting of the polariton-polariton scattering at the pump angle. The normal branch is plotted in Fig. 7.1 (a) for $gn = 0$, $gn = 0.5\text{meV}$ and $gn = 1\text{meV}$. While for the low density (or non-interacting) limit the dispersion remains parabolic, the effects of polariton-polariton interactions are visible for $gn = 0.5\text{meV}$ and $gn = 1\text{meV}$, in the form of a blue shift gn of the dispersion curve (interaction energy) and a linearization of the dispersion in the vicinity of $k_{\text{pump}} = 0$. The asymptotic behavior of the excitation spectrum is

$$E(k_{//}) - E_0 = \begin{cases} \sqrt{\frac{ng}{m}} \hbar k_{//} + ng & \text{for } k_{//} \rightarrow 0 \\ \epsilon(k_{//}) + 2ng & \text{for } k_{//} \rightarrow \infty \end{cases}. \quad (7.2)$$

We can see that in the large in-plane wavevector limit one recovers a parabolic (free particle) dispersion. In the low in-plane wavevector limit, though, a linear, sound-like dispersion takes place, allowing to define a speed of sound in the system: $c_s = \sqrt{\frac{ng}{m}}$. Comparing the kinetic energy $\epsilon(k_{//}) = \frac{\hbar^2 k_{//}^2}{2m}$ with the interaction energy ng allows to evaluate the in-plane wavevector for which the crossover between the free particle-like behavior and the sound-like behavior takes place: $k \sim \frac{\sqrt{2mgn}}{\hbar}$. The corresponding distance is called the *healing length*: $\xi \sim \frac{\hbar}{\sqrt{2mgn}}$.

Galilean boost In order to study the behavior of a propagating polariton gas, injected with a finite in-plane momentum $k'_{//}$ (linked to the excitation laser incidence angle θ by $k'_{//} = \frac{2\pi}{\lambda_0} \sin \theta$), one needs to apply a Galilean boost to the excitation spectrum:

$$\begin{cases} k_{//} \rightarrow k_{//} + k'_{//} \\ E(k_{//}) \rightarrow E(k_{//}) + \frac{\hbar^2 k_{//} k'_{//}}{m} + \frac{\hbar^2 k'^2_{//}}{2m} \end{cases}. \quad (7.3)$$

The resulting dispersions are plotted in Fig. 7.1 (b), for a pump in-plane wavevector of $k'_{//} = -1.2\mu\text{m}^{-1}$, and for the same three values of gn than in Fig. 7.1 (a). These dispersions allow to describe the flow of a polariton gas, with a flow speed v given by $v = \frac{\hbar k'_{//}}{m}$. While the parabola of the low density limit case remains unchanged (black curve), the excitation spectra (red and blue curves) are tilted by the Galilean boost. The red and blue curves present then different situations: for the red curve, the fluid velocity is supersonic ($v > c_s$), while for the blue curve, which corresponds to a larger the speed of sound, the fluid velocity is subsonic ($v < c_s$).

Resonant Rayleigh scattering When a propagating polariton population is injected, elastic scattering on the disorder landscape (or resonant Rayleigh scattering - RRS) occurs, with conservation of energy. Therefore, a modification of the excitation spectrum also modifies the RRS. In the low density limit, energy conserving

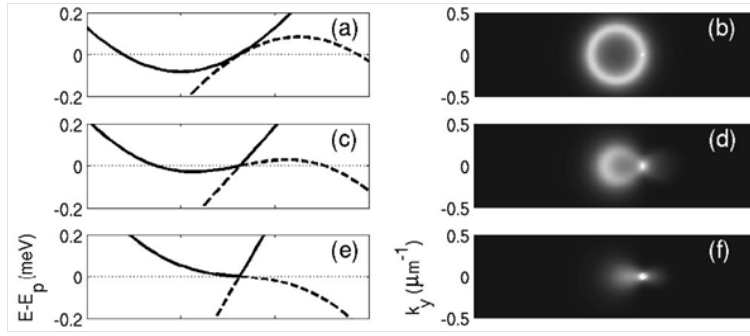


Figure 7.2: Figure part reproduced from Ref. [15]. *Left column:* Bogoliubov excitation spectra (plain line: normal branch, dashed line: ghost branch) for the three mentioned regimes: low density (or linear) regime (a), Čerenkov regime (c), and superfluid (e). *Right column:* corresponding RRS patterns. In the low density regime, interaction of the polariton gas with disorder leads to the building of the so-called Rayleigh ring (b). In the superfluid regime, the Rayleigh ring has collapsed (f).

RRS gives rise to a ring in the momentum space, the so-called *Rayleigh ring*, centered on $k_{\parallel} = 0$, with a radius given by k_{pump} . Under high excitation density, when the fluid velocity is subsonic (blue dispersion curve), the dispersion does not offer any more the possibility of Rayleigh scattering. This collapse of the Rayleigh ring prevents any interaction of disorder with the polariton fluid, which can flow without friction. In this case, the Landau criterion is fulfilled, as the fluid velocity is lower than the sound velocity. It corresponds to a Mach number (defined as the ratio of the fluid velocity v over the sound speed c_s) smaller than one ($\frac{v}{c_s} < 1$). The red dispersion curve depicts the so-called Čerenkov regime, where the fluid velocity is greater than the sound speed ($\frac{v}{c_s} > 1$). The different RRS patterns (and thus the transition to superfluidity) can be easily observed by collecting the photons leaking out of the cavity and imaging them in the Fourier plane. Moreover, the fluid velocity (linked to the excitation angle) and the sound speed (linked to the excitation density) are both tunable parameters. Images of the RRS in the three mentioned regimes (low density, Čerenkov and superfluid) are shown in Fig. 7.2 (taken from Ref. [15]).

On the experimental side, frictionless flow of a polariton wavepacket has been reported in a triggered OPO scheme [129]. The collapse of the Rayleigh ring and transition to superfluidity has been demonstrated in a resonantly injected polariton fluid [16]. In this last paper, depending on the fluid velocity, superfluid or Čerenkov regimes were observed.

Similarly to conventional superfluids, quantum turbulence is expected to appear in microcavities as a friction mechanism, at the breakdown of superfluidity [130, 131]. While decreasing the sound speed in the system, hydrodynamic nucleation of quantized vortex pairs occurs when the local velocity in the vicinity of the obstacle gets larger than the sound velocity. Soliton lines, and eventually a Čerenkov regime, follow when the velocity of the fluid far from the obstacle becomes greater than the speed of sound [131]. The major difficulty, pointed out in Refs [130, 131], is that the excitation laser imposes its phase on the polariton fluid, preventing the formation of non-trivial phase structures such as vortices. To overcome this issue, an abrupt

switch off of the excitation laser [130] or a non uniform spatial pump profile [131] are proposed. In our case, we are going to use a pulsed excitation, in order to create a polariton wavepacket which will be free to propagate in the microcavity plane once the excitation pulse is gone.

7.3 Setup and experimental conditions

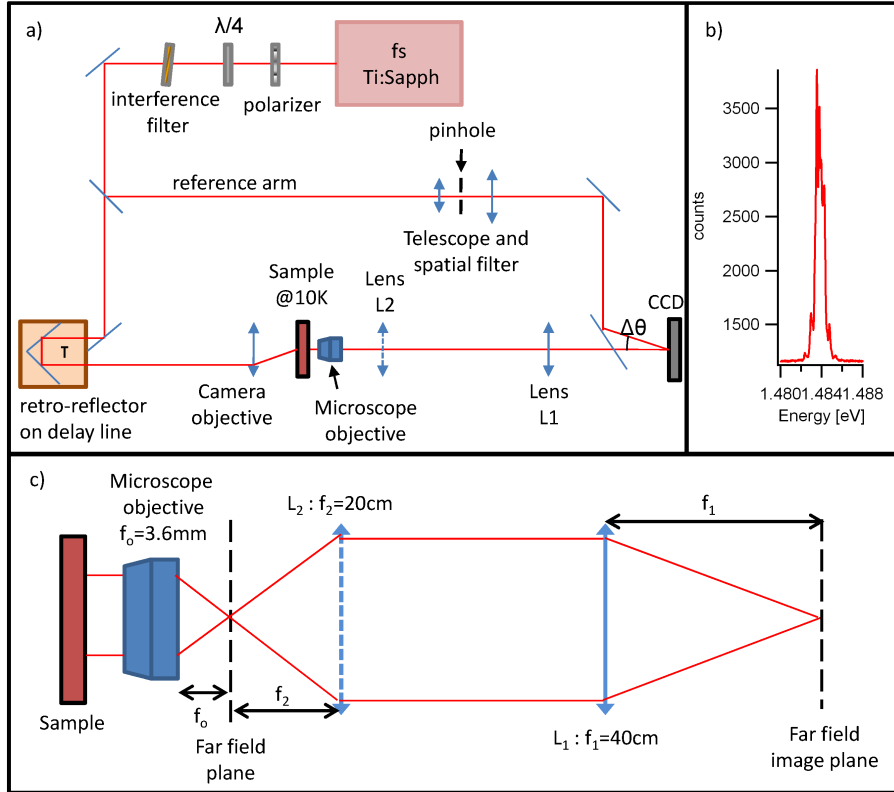


Figure 7.3: **Experimental setup** (a) The experimental setup is very similar to the one presented in the previous chapter 6, except that the pulse is spectrally filtered by an interference filter. An optical isolator, composed of a polarizer and a $\lambda/4$ waveplate is added at the laser output, in order to avoid back reflections into the mode-locked laser cavity. The resulting laser light is circularly polarized. On the imaging side, the L_1 lens has a focal length of $f_1 = 40\text{cm}$, for real space (or near field) imaging. A lens L_2 , of focal length $f_2 = 20\text{cm}$ is added for the imaging of the Fourier space (or far field). (b) Spectrum of the laser pulse at the output of the interference filter. It is $\sim 1\text{meV}$ broad. Its very irregular shape is most probably due to a polarization sensitivity of the interference filter. (c) Detail of the imaging configuration. The optical rays are traced for the imaging of the Fourier space, when L_2 is added on the optical path. This setup provides a magnification of $M = 110\times$, and magnifies the Fourier space twice as much as the $2f - 2f$ configuration presented in Fig. 3.2.

The setup used (Fig. 7.3) is quite similar to the one used for the observation of oscillations between vortex and anti-vortex states (chapter 6). The major change is the use of an interference filter instead of the pulse shaper. Indeed, the power

losses in the pulse shaper (mainly due to the $\sim 60\%$ maximum efficiency of the ruled grating, on which the pulse was passing two times) prevented us to get densities large enough to significantly enter into the polaritonic non-linear regime. Spectral filtering is necessary, though, in order to avoid exciting the upper polariton branch (and avoid coherent effects such as Rabi oscillations to take place). Using the interference filter allows us to reach excitation powers up to $3mW$ and to address non-linear effects. The filter is preceded by an optical isolator, made of a polarizer aligned on the laser polarization, and a $\lambda/4$ waveplate whose optical axis is aligned at 45° of the laser polarization, providing thus a circularly polarized light. These two elements serve as an optical isolator, as any reflection of the laser on subsequent optics will get π -shifted and thus come back with an opposite circular polarization, and eventually cross-polarized with respect to the polarizer axis. This system is used to avoid problematic back reflections of the laser light into the mode-locked laser cavity. The circularly polarized laser pulse passes then through the interference filter, which provides a $\sim 1meV$ -broad pulse, whose spectrum is shown in Fig. 7.3 (b)². This pulse is then separated into an excitation pulse and a reference pulse, in a Mach-Zehnder configuration, similarly to what we described in the previous chapters. Removing the sample and scanning the delay between the excitation and reference arms allows to perform an autocorrelation measurement of the laser pulse (black curve in Fig. 7.6 (a)), indicating a $\sim 3ps$ -long pulse. This will therefore set the time resolution of our setup. Another modification of the setup, compared to chapter 6, is the position and focal lengths of the imaging lenses. For real space imaging we use a $40cm$ focal length lens, providing us a magnification of $M = 110\times$. For the Fourier space imaging, we add a $20cm$ focal length lens (see Fig. 7.3 (c)), allowing to magnify the Fourier space two times more than with the $25cm$ focal length lens in the $2f - 2f$ configuration used in chapters 3 and 4.

Using our $\sim 3ps$ -long excitation pulse, we inject a polariton wavepacket with an oblique excitation angle. The wavepacket can then evolve freely in the microcavity plane during the polariton lifetime (measured characteristic decay time: $\tau \sim 15ps$), providing a sufficiently long time window during which quantum turbulence can form. We resonantly inject polaritons in the lower polariton branch with an initial in-plane momentum imposed by the pump of $k_{//} = 1.2\mu m^{-1}$, corresponding to a fluid velocity of $v = 1.13\mu m/ps$. In Fig. 7.4 (b) the yellow circle indicates the pump extension in energy and momentum. Our theoretical approach of considering the Gross-Pitaevskii equation for the lower polariton branch only is therefore justified, because the upper branch is not excited here. The exciton-photon detuning δ is also taken to be much smaller than the Rabi splitting. We let the wavepacket scatter on a structural defect of $\sim 5\mu m$ transverse size (Fig. 1a). Our time and phase-resolved imaging setup allows us to observe the dynamics of the scattering on a picosecond

²The origin of the very irregular shape of this spectrum has been identified only recently, after having performed all the experiments presented in this chapter. The shape of the spectrum is dependant of the laser polarization and incidence angle on the filter. The interference filter being a Fabry-Pérot resonator, it is quite natural to expect a TE-TM splitting for an oblique incidence angle. Recently, we have therefore placed the interference filter before the optical isolator, in order to get a linearly polarized incident laser, and used a $\lambda/2$ waveplate to rotate the laser polarisation and eliminate the TE-TM splitting. By this way we could therefore obtain a “clean” Lorentzian spectrum, as was expected from this filter.

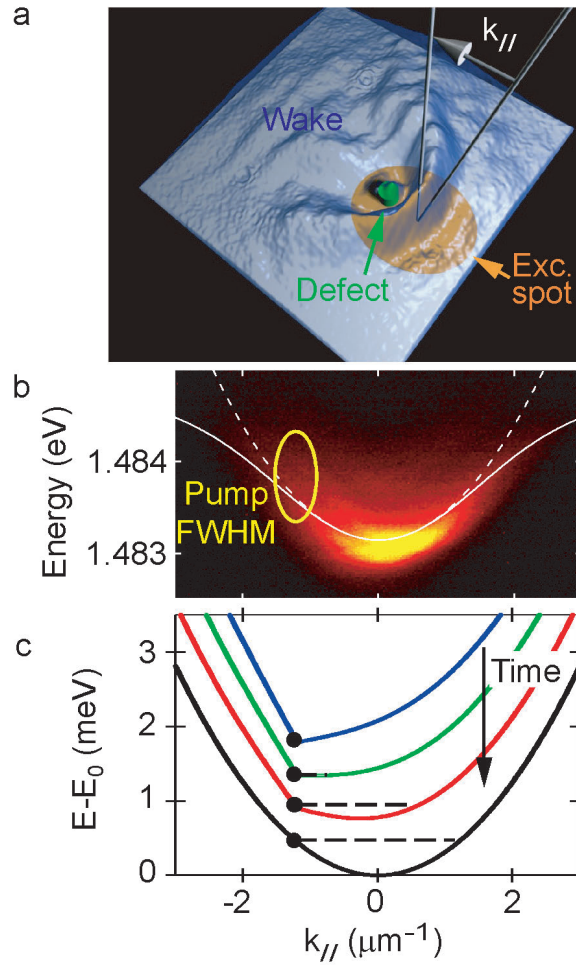


Figure 7.4: (a) Scheme of the experiment: A polariton wavepacket is resonantly injected with an in-plane wavevector $k_{//}$ in front of a structural defect on which it scatters. (b) Experimental polaritonic dispersion curve, under non-resonant pumping. The plain line indicates the theoretical lower polariton (LP) dispersion, and the dashed line the standard small momentum parabolic approximation of the LP branch. During the experiment, polaritons are resonantly injected in the lower polariton branch: the yellow circle indicates the energy and momentum extension of the pulsed pump. (c) Theoretical dispersion curves. Under low excitation density, the system is in the linear regime, and the dispersion is parabolic in the small momentum approximation (black curve). Polariton population is given by the black dot, and the intersection of the dashed line with the dispersion gives the possibility of scattering events which conserve energy. When increasing the pump power, the excitation spectrum is modified, going from a Cerenkov regime (red curve) to a superfluid regime (blue curve). The black arrow schematically shows the time evolution of the dispersion curve during the decay of the polariton population.

time scale, and to track the formation and migration of vortices in the turbulent flow.

An extremely important consequence of the pulsed excitation is that we are not creating a steady flow. The time dependence of the polariton population will lead to a dynamical excitation spectrum, and a speed of sound changing with time. Using a high density pulsed excitation, we expect therefore to pass through all the

different regimes after the polariton injection (as schematically indicated by the black time arrow in Fig. 7.4), from subsonic to the low density limit, leading to an extremely rich dynamics. In particular, the system will be bound to pass through the intermediate regime depicted by the green dispersion curve in Fig. 7.4 (c), corresponding to a Mach number of $\frac{v}{c_s} = 1$. In such a case, the dispersion curve is flat on a finite distribution of wavevectors, offering a continuous reciprocal space region in which Rayleigh scattering can occur. This feature appears crucial to us for the vortex nucleation mechanism to occur, as we will discuss later on. Eventually, because of the spatial inhomogeneity of the polariton wavepacket, we will also have to consider local flow velocities and local sound speeds.

7.4 Preliminary data: Time-integrated measurements

In order to have an overview on the different flow regimes that can be observed, we start by presenting time-integrated spatial patterns of the scattering process, as well as momentum space resolved spectra (using the technique presented in section 3.4), taken along the k_x axis. By “time-integrated” we simply mean the pattern recorded on our CCD, without using the reference pulse. In Fig. 7.5 (a)-(e) are presented the spatial patterns, and in Fig. 7.5 (f)-(j) the corresponding spectra, for different experimental conditions (excitation in-plane momentum k_{pump} and power P_{exc}). On the spatial images, the polariton flow is going in the $-x$ direction (leftward). In the momentum space resolved spectra, the white dashed line shows the lower polariton dispersion (in the non-interacting limit), fitted from the non-resonant spectrum of Fig. 7.4 (b). The momentum and energy extension of the pump is indicated in yellow. As these measurements are time-integrated, they should be considered with great care, as they are an average over the whole population dynamics. Moreover it is probable that the momentum space resolved spectra, which are a cut along the k_x axis in the two-dimensional momentum space distribution, were not taken exactly at $k_y = 0$.

Nevertheless, this set of time integrated bring us interesting informations. For low excitation powers (Fig. 7.5(a)-(b)), parabolic wavefronts can be observed on the spatial profiles, as a result of the elastic scattering on a structural defect. There is virtually no fluid density behind the obstacle. On the corresponding momentum-resolved spectra (Fig. 7.5(f)-(g)), the major contributions come from the pump in-plane momentum and its opposite (the so-called *back-scattering* direction, as it is expected from a cut along the k_x direction in the Rayleigh ring).

When increasing the excitation power (and thus increasing the average speed of sound), there is a critical excitation power ($P_{exc}^{thresh} = 20\mu W$), above which the momentum-resolved spectrum are drastically different. It can be seen in Fig. 7.5(h) that the contribution from the back-scattering direction has vanished. Instead of this, there seems to be a relaxation down to the bottom of the polariton branch. At even higher excitation power ($2.1mW$ - Fig. 7.5(i)), the spectrum is even more peculiar. It is however very difficult to interpret this time-integrated spectrum, as the dynamics is not revealed here. The reason for which no emission can be observed

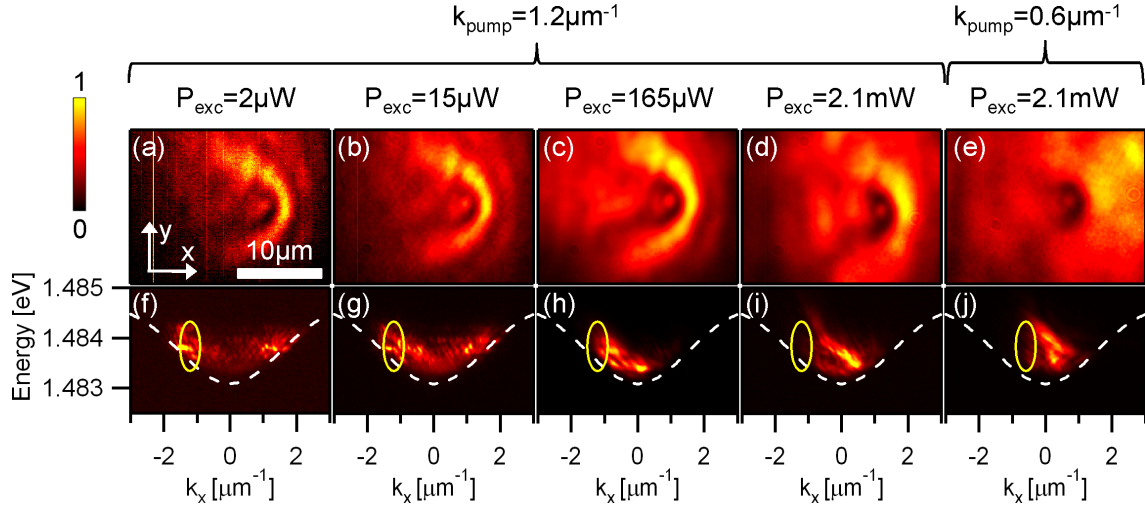


Figure 7.5: **Overview of the different flow regimes: time-integrated data (a)-(e)** Spatial images of the scattering process, for various pump power and in-plane momenta. The flow is going leftwards. In (a), the parabolic wavefronts are the signature of the elastic scattering on a non-perturbative defect. (f)-(j) Corresponding momentum space resolved spectra, taken in the same experimental conditions than (a)-(e). The spectra are resolved along k_x , and may not have been taken exactly at $k_y = 0$. The observed regimes go, from left to right on the figure, from a standard elastic scattering process to a seemingly superfluid regime. All images and spectra are plotted in a normalized color scale.

from the pump angle is probably that the spectrum, resolved along the k_x direction only, was not taken exactly at $k_y = 0$. From the spatial images (Fig. 7.5(c)-(d)), an interesting feature is the appearance of polariton density behind the obstacle. However, two oblique low-density lines are preserved. From these time-integrated measurements it is not possible to tell if these lines are soliton lines, as predicted by Pigeon *et al.* [131], or if they are the time-averaged paths of moving vortices.

This last excitation power being the highest experimentally available, it was not possible to observe additional phenomenologies by increasing more the average speed of sound in the system. However, we could use the other tunable parameter, which is the polariton flow speed. Reducing the excitation incidence angle allows to reduce the polariton wavepacket initial in-plane momentum. Below a critical in-plane wavevector of $0.6 \mu m^{-1}$, we do not observe any more oblique low density lines in the spatial image (Fig. 7.5 (e)), neither any sign of parabolic wavefront. The polariton fluid seems to flow homogeneously without being affected by the presence of the defect (except for its localized footprint). The corresponding momentum-resolved spectra (Fig. 7.5 (d)) is very peculiar, as it features two populations at different energies. It might be caused by the multi-peaked excitation spectrum. For future experiments, performing a tomography in the two-dimensional momentum space for the different excitation powers would provide much more information than these one-dimensional spectra.

After this overview of the different regimes that can be observed with time-integrated measurement, we are now going to show the time-resolved measurements, which will bring us much more detailed information about the dynamics of the polariton flow. We will show the three characteristic regimes observed, i.e (1) the

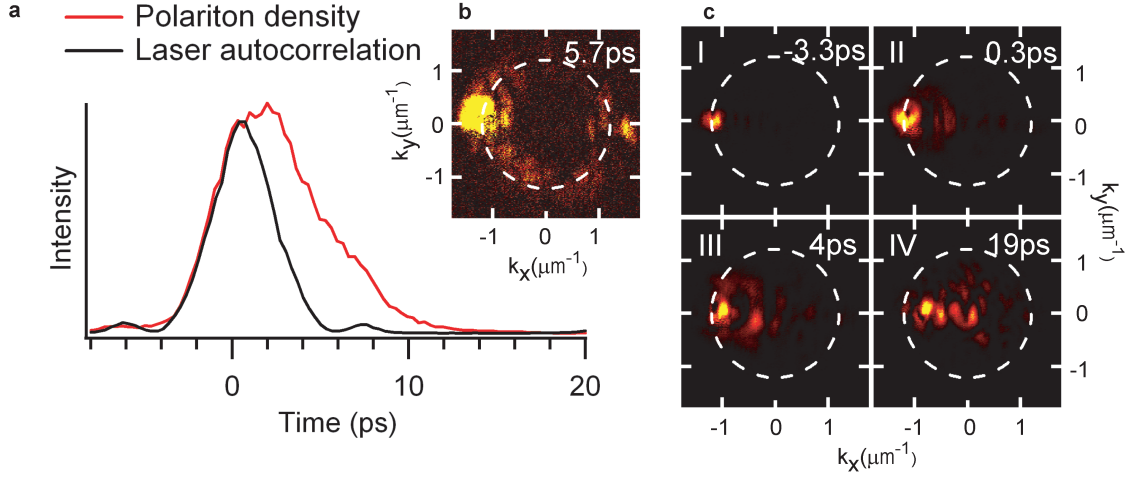


Figure 7.6: **Population dynamics** (a) *Red curve*: Measured polariton density $|\Psi|^2$, integrated in a small region in the vicinity of the obstacle, with respect to the interferometer delay. *Black curve*: autocorrelation of the pulsed excitation. Comparison of red and black curves shows the time window on which non-trivial phase patterns such as vortices can develop in the injected polariton wavepacket. (b) Momentum space image of the emission, under low excitation power ($15\mu\text{W}$). In this low excitation density regime, a Rayleigh ring is visible, as a result of the scattering of the polariton wavepacket on the defect. The intensity of the Rayleigh ring is maximal 5.7ps after the excitation pulse. The dashed circle indicates the expected position of the Rayleigh ring in the low density regime. (c) Momentum space dynamics of the emission, under high excitation power (2.1mW). The time dependent modification of the excitation spectrum leads to a spreading of the polariton population inside the Rayleigh ring, and a general slow down of the polariton propagation.

low density regime (corresponding to Fig. 7.5(b) and (g)), in which “standard” elastic scattering occurs, (2) the high density regime (corresponding to Fig. 7.5(d) and (i)), for which we will demonstrate the hydrodynamic nucleation of vortices in the wake of the obstacle, and (3) the seemingly superfluid, low momentum regime (corresponding to Fig. 7.5(e) and (j)).

7.5 Population dynamics

Interferometric measurements taken for different delays between the excitation and reference pulse allow us to retrieve the dynamics of the polariton fluid. In Fig. 7.6 (a) we display the normalized polariton density integrated in the vicinity of the defect (red curve), and compare it to the normalized autocorrelation measurement of the laser (black curve). It shows that a significant fraction of the polariton population is still moving in the vicinity of the obstacle even when the excitation pulse is gone.

We first discuss the dynamics in the momentum space. At low excitation pump power ($15\mu\text{W}$), the system is in the linear regime. In this case, a Rayleigh ring (Fig. 7.6 (b)) appears due to elastic scattering of polaritons on the obstacle and surrounding disorder, and disappears with the polariton decay time. At high pump power (2.1mW), the time-dependent polariton density makes the dispersion curve vary with time, and pass through the different cases depicted in Fig. 7.4 (c). The

four panels of Fig. 7.6 (c) show different snapshots of this evolution.

First the excitation laser creates a wavepacket with an in-plane momentum of $k_{//} = 1.2\mu m^{-1}$ (Fig. 7.6 (c)I). Then, as the polariton density decays, we observe the filling of the interior of the Rayleigh ring (Fig. 7.6 (c) II-IV), resulting in an average slow down of the wavepacket velocity. This behaviour can be qualitatively reproduced using the generalized Gross-Pitaevskii model (see Fig. 7.14 III), and understood as follow: the decay of the polariton density is accompanied by a decrease of the sound velocity. When $v \sim c_s$ (green dispersion curve in Fig. 7.4 (c)), elastic scattering of the polariton wavepacket on the environment fills a contiguous region inside the Rayleigh ring, relaxing the wavevector conservation rule. This is of crucial importance for the vortex nucleation mechanism, as vortices can appear only when a significant quantity of fluid has been slowed down behind the obstacle, and that a contiguous and sufficiently broad region of the reciprocal space provides the necessary wavevectors to form the rotating flow around the phase singularity.

Bringing together this observed slow down with the time-integrated momentum space resolved spectra of Fig. 7.5 (h) and (i) allows to give the following picture for the high density population dynamics: there is a relaxation towards the bottom of the polariton dispersion curve (the interaction of the excitation spectrum with the obstacle and disorder causing the loss of momentum, and the decay of the population causing the loss of interaction energy).

7.6 Spatial dynamics

7.6.1 Low density regime (elastic scattering - supersonic)

Figure 7.7 shows the scattering of the low density wavepacket on the obstacle, for an excitation power of $15\mu W$ and an excitation angle of 9.3° (corresponding to a pump in-plane momentum of $1.2\mu m^{-1}$). The very low density yields to a very low speed of sound in the system ($c_s = \sqrt{\frac{nq}{m}}$). This regime can thus be seen as strongly supersonic. In this regime, the polariton gas normally interact with disorder, and scatters elastically on the obstacle. In the momentum space, a Rayleigh ring is visible, as shown in Fig. 7.6 (b). In the real space, a parabolic wavefront is created as an interference between the propagating polaritons and the scattered one. The three rows of Fig. 7.7 display experimental images of (I) the normalized polariton density, (II) the fringes of the interferogram (in a saturated color scale, in order to track the fork-like dislocations, if any), and (III) the phase of the polariton gas, for different times after the excitation pulse. The homodyne setup allows not only to access the dynamics of the polariton fluid density, but also its phase, whose gradient provides the local in-plane momentum of the fluid (linked to the local fluid velocity by $v = \frac{\hbar k_{//}}{m}$). The estimated obstacle position is indicated with a green circle, and the polariton flow goes leftward. Using acquisition times of 0.2 seconds, each measurement is an integration over 1.6×10^7 experimental realizations.

In the first column ($-0.7ps$), the phase structure is imposed by the excitation laser. The fluid density already shows the precursors of the parabolic wavefronts, though. These wavefronts are much more defined in the second column, where a non-trivial phase structure has developed: finite phase jumps can be seen between the

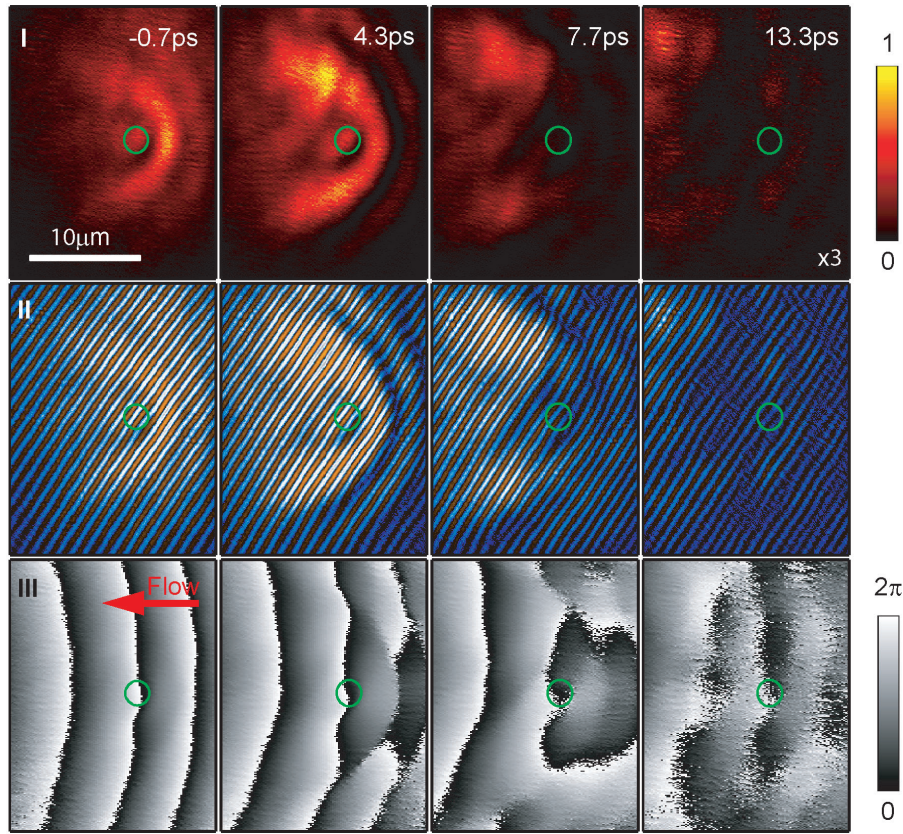


Figure 7.7: **Experiment: low density regime** Experimental images of the scattering of the polariton wavepacket on the structural defect (indicated by a green circle), for the low density regime ($P_{exc} = 15\mu W$). The pump in-plane momentum is $1.2\mu m^{-1}$. The three rows show the polariton density (I), the fringes of the measured interferogram, in a saturated color scale (II), and the polariton phase (III). With this low excitation density, the polariton wavepacket undergoes elastic scattering on the obstacle, leading to parabolic interference fringes between the propagating polariton and the backscattered ones. The phase resolution allows to evidence a finite phase jump between the different parabolic precursors. Density values are multiplied by a factor three in the last density plot, for the sake of visibility.

successive wavefronts. In the third and fourth columns, the decay of the polariton population can be observed.

Extracting the fluid velocity from the phase gradient As mentioned earlier, the phase structure allows to determine the velocity field of the polariton fluid. A crucial point is therefore to determine the phase gradient induced by the setup alignment, or in other words, the incidence angle of the reference pulse on the CCD. In order to do this, it is possible to measure the interference pattern resulting from the coherent emission of a polariton trap ground state, as explained in chapter 4. In experiments of polariton fluid dynamics, it is also possible to use a low density measurement, where a Rayleigh ring is expected in the Fourier plane. If the Fourier plane can be accessed optically, as in Fig. 7.6 (b) and (c), it can also be obtained numerically, from the FFT of the interferogram. The dynamics in the momentum

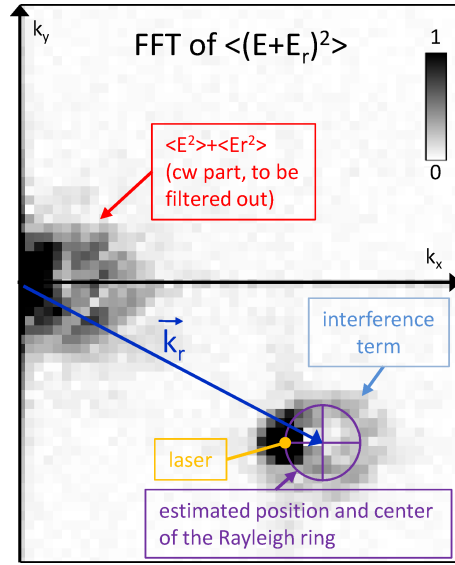


Figure 7.8: FFT of the interferogram corresponding to the second column of Fig. 7.7. Only the half part of the Fourier plane is shown, as it is symmetric with respect of the origin. The *cw* term is visible at the origin of the Fourier plane, and will be filtered out. The interference term forms the Rayleigh ring, whose center can be estimated in order to determine the value of the reference in-CCD-plane wavevector \vec{k}_r . This value is used to remove the phase gradient induced by the setup alignment.

space can therefore be obtained numerically, using the sole interferometric measurement in the real space (however, optical measurement of the dynamics in the Fourier space where also performed, in order to achieve a better image resolution). Determining the phase gradient induced by the reference arm incidence angle corresponds to pointing out the value of the reference in-CCD-plane momentum. A typical real space interferogram FFT, corresponding to the second column of Fig. 7.7, is presented in Fig. 7.8. The Rayleigh ring and its center can be identified (in violet). The center of the Rayleigh ring being expected to be the center of the momentum space, it allows to point out the value of the in-CCD-plane momentum (in blue) and thus of the phase gradient induced by the reference arm alignment. This reference can be used for all other measurements, as it depends only on the setup alignment. It is of crucial importance, as it allows to determine the absolute value of the fluid velocity. We have checked that by using this reference, the measured in-plane momentum on the first column of Fig. 7.7 corresponds indeed to the pump in-plane momentum of $1.2\mu\text{m}^{-1}$ (a 2π phase shift should be obtained on a distance Δx such as $\Delta x = \frac{2\pi}{1.2\mu\text{m}^{-1}} = 5.2\mu\text{m}$). A systematic error, corresponding to an error of one pixel on the determination of the reference in-CCD-plane wavevector, will be considered. Local fluid velocities are then obtained by fitting the slope of the phase profile in the region of interest. The total error on this value takes into account the standard deviation of the linear fit, as well as the systematic error coming from the determination of the phase gradient induced by the setup alignment.

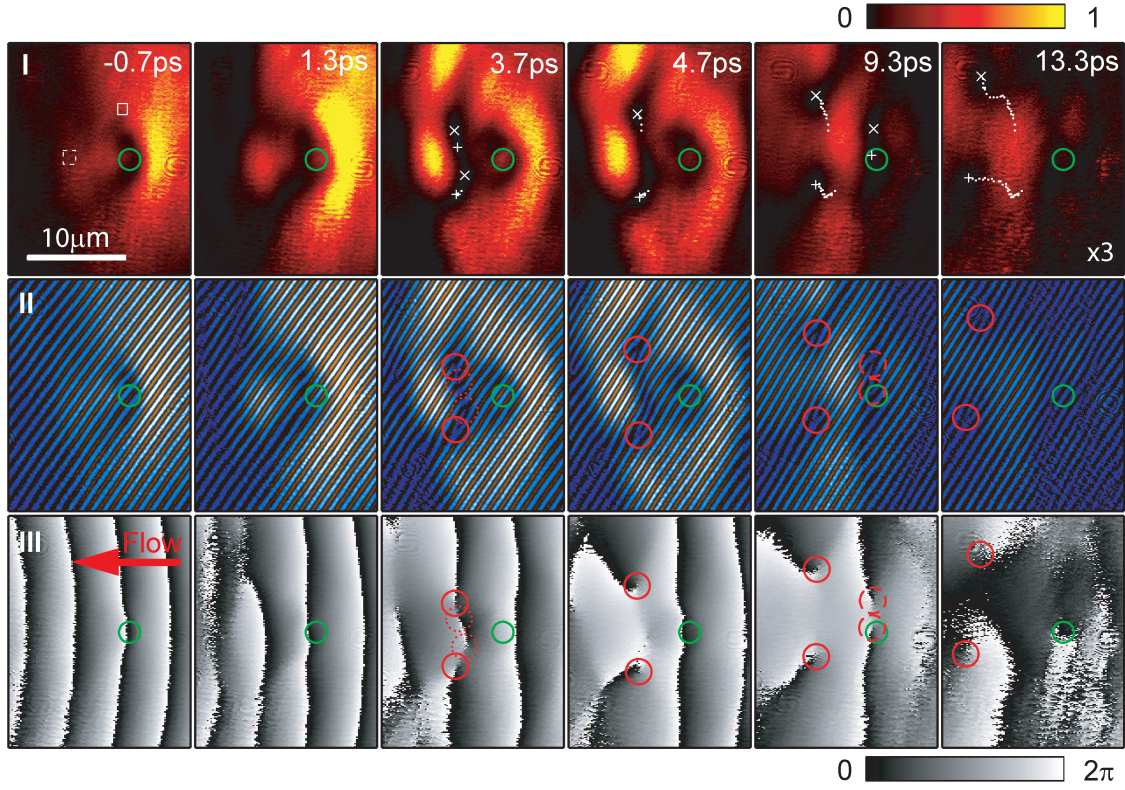


Figure 7.9: **Experiment: vortex nucleation regime** Experimental images for the high excitation density ($P_{exc} = 2.1mW$) and high fluid velocity. The wavepacket propagates towards the left, with an initial momentum of $1.2\mu m^{-1}$. The three rows show (I) the polariton density, (II) the fringes of the measured interferogram, in a saturated color scale, in order to facilitate the observation of the vortices, (III) the polariton phase. In the first column (-0.7ps), the phase structure is fully imposed by the excitation pulse, preventing the formation of vortices. Second column (1.3ps): the polariton wavepacket starts to feel the effect of the obstacle, resulting in a zone of minimal polariton density in the wake of the obstacle, and a bending of the polariton wavefront. Third column (3.7ps): nucleation of vortices in the wake of the obstacle. Vortices are indicated with white markers (\times for vortex, $+$ for anti-vortex) on the density plot, and are circled in red on the fringes and phase plots. Dotted circles indicate short-lived vortices. Fourth, fifth and sixth columns (from 4.7 to 13.3 ps): motion of the long-lived vortex pair. Previous vortex positions are indicated with white dots on the density plots, allowing to follow the vortex motion. Dashed circles in the fifth column (9.3ps) indicate the position of a new vortex pair which moves on a few microns before disappearing due to the decay of the polariton population. For the sake of visibility, density values are multiplied by a factor three in the last density plot.

7.6.2 Vortex nucleation regime

We discuss now the dynamics of the high density regime (corresponding to the time-integrated image of Fig. 7.5 (d)). Figure 7.9 displays experimental images of (I) the normalized polariton density, (II) the fringes of the interferogram (in a saturated color scale, in order to track the fork-like dislocations), and (III) the phase of the polariton gas, for different times after the excitation pulse. The initial wavepacket

momentum is still $1.2\mu m^{-1}$, and the average excitation power is $2.1mW$. In the first column ($-0.7ps$), the phase structure is imposed by the excitation laser (this feature is referred as a “phase-pinned superfluid” by Bolda *et al.* [130]). The phase gradient allows to extract the flow velocity, which is measured to be $1.1 \pm 0.2\mu m/ps$, in agreement with the injected velocity of $1.13\mu m/ps$. In the second column ($1.3ps$), a low density region appears in the wake of the defect, along with a curvature of the wavefront. Thanks to the phase resolution, a slow down of the polariton flow in the wake of the obstacle can be observed. The value of the flow velocity behind the obstacle (in the region delimited by the dashed white square in Fig. 7.9 I) is shown in Fig. 7.12 (a). In the third column of Fig. 7.9 ($3.7ps$), it is measured to be $0.9 \pm 0.2\mu m/ps$, and goes down to $0.3 \pm 0.2\mu m/ps$ in the fifth column ($9.3ps$). There is therefore a phase accumulation between the almost stationary wave behind the obstacle and the main flow. As expected in a quantum fluid, where the circulation is quantized, the phase accumulation is accompanied by the nucleation of quantized vortices [111]. The nucleation of vortices can be observed in the third column ($3.7ps$) of Fig. 3, where a tearing of the phase front is visible. Vortices are unambiguously identified by a minimum of density and a fork-like dislocation in the interferogram accompanied with a phase singularity in the phase structure. They are indicated by white markers (\times for vortex and $+$ for anti-vortex) on the density map, and red circles on the interferogram and phase maps. At the onset of the vortex nucleation, four of them are nucleated in the wake of the defect, but two of them (circled with dotted lines) merge together within less than 2 picoseconds. It indicates most likely that the size of the obstacle is large enough for nucleating a vortex pair, whose core diameters are measured to be $2\mu m$ to $3.3\mu m$ (depending on the vortex under scrutiny and the line profile axis)³, but too small to allow the nucleation of four vortices. The creation and merging of this additional vortex pair may also be due to the local disorder landscape (numerical simulations - see Section 7.8 - also show that disorder can lead to the creation of short-lived vortex pairs in low fluid density areas). The remaining vortex pair flows downstream, and we track its motion (white dots on the density map) on a dozen of microns and picoseconds, until the decay of the polariton population. While in atomic condensates the vortex trajectories are closed loops due to the trapping potential [119], the polariton vortices are free to propagate in the microcavity plane. The snaky nature of their tracks is due to the local disorder landscape, and the slight right turn is attributed to the microcavity wedge that provides a global potential gradient towards this direction. It is also interesting to note the additional vortex pair created at a delay of 9 picoseconds (visible in the fifth column, dashed circles). This pair propagates on a few microns and then disappears in the noise due to signal decay. It does not allow to define a shedding frequency, as this latter is expected to depend on the fluid density [110, 111], which is varying with time in our experiment.

³Using estimations of the local polariton density (see Section 7.7 for details), we find a healing length of $\xi \sim 1\mu m$, which is of the order of the measured vortex core size.

7.6.3 Low velocity regime

The last regime to be detailed is the one corresponding to the time-integrated image of Fig. 7.5 (e), using a high excitation power ($2.1mW$) but a lower excitation angle ($k_{pump} = 0.6\mu m^{-1}$). The dynamics is displayed in Fig. 7.10. While the fluid density passes apparently unaffected over the defect, the phase structure allows to evidence a progressive bending of the phase front, corresponding to a slow down of the flow behind the obstacle. This yields to the nucleation of a unique vortex pair at long time, when only a fraction of the polariton population is remaining. At the nucleation time, the fluid velocity is very low in the vicinity of the obstacle. As a consequence the vortex pair cannot be dragged away from the obstacle before the complete decay of the polariton population. Additionally, this low velocity regime probably provides the most accurate estimation of the obstacle effective size, given by the dark region in the third column of Fig. 7.10 I. According to this the defect would have a transverse size of $\sim 5\mu m$ and a size in the direction of the flow of $\sim 2\mu m$.

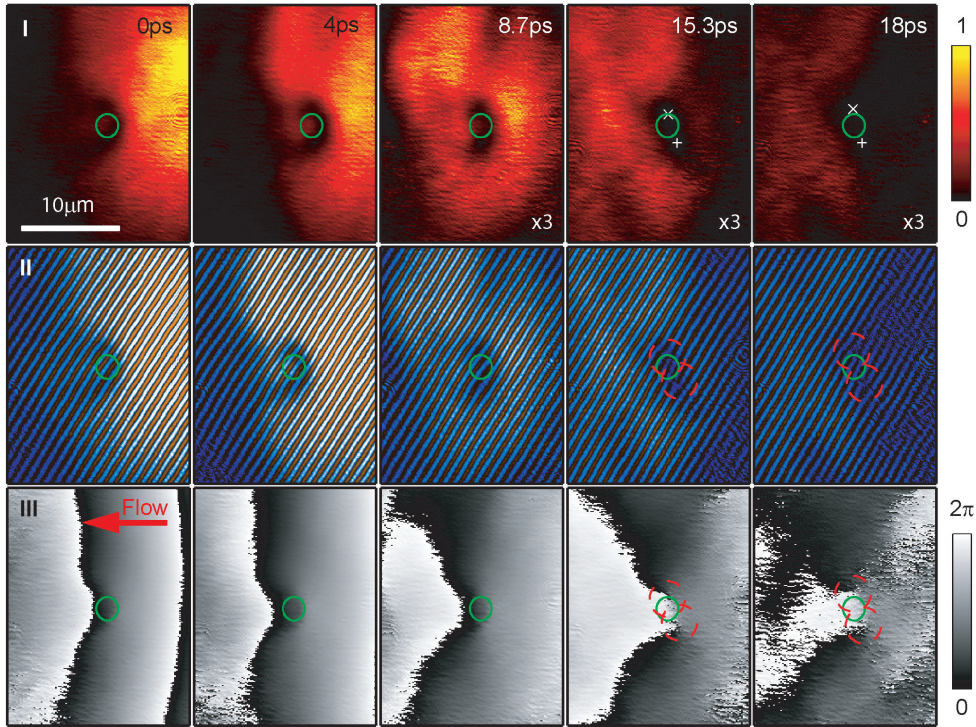


Figure 7.10: **Experiment: low velocity regime** Same as in Fig. 7.9 (average excitation density of $P_{exc} = 2.1mW$), but for an initial momentum of the polariton wavepacket of $0.6\mu m^{-1}$. The three rows show the polariton density (I), the fringes of the measured interferogram, in a saturated color scale (II), and the polariton phase (III). With such a low momentum, the wavepacket passes the obstacle without creating any turbulence in the wake of the obstacle. When the polariton population has significantly decayed (two last columns), a vortex pair is created at the boundary of the obstacle. The pair remains stitched to the defect for several picoseconds, and disappears in the noise when the polariton population has decayed. Density values are multiplied by a factor three in the three last density plots, for the sake of visibility.

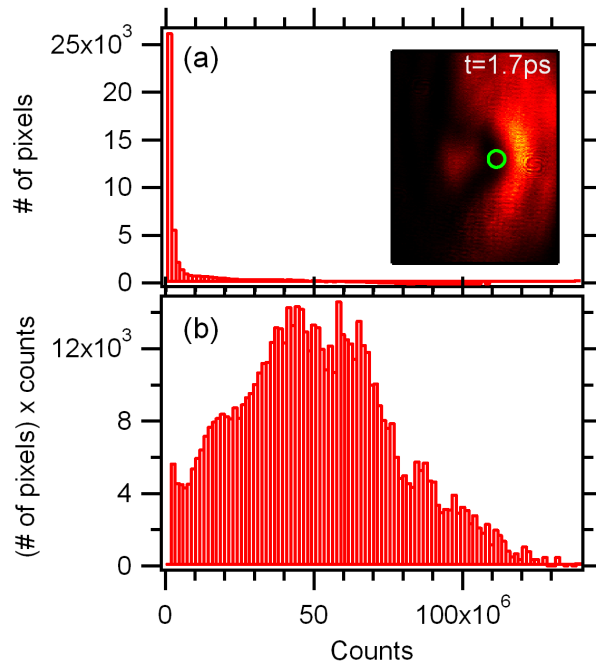


Figure 7.11: (a) Histogram displaying the number of pixels that registered a given number of counts, for the density map at $t = 1.7ps$ (shown in inset). (b) Same histogram, but the number of pixels is multiplied by the number of counts. This distribution is expected to mimic the emission spectrum that should be observed at this time.

7.7 Determining experimental conditions for vortex nucleation

In theoretical predictions [110, 112, 131] different flow regimes are observed depending on the Mach number. Turbulence is expected in the wake of the obstacle when the local velocity on the perimeter of the impenetrable obstacle becomes supersonic. The original work of Frisch *et al.* [110] also predicts that this critical velocity is attained on the obstacle perimeter when $\frac{v}{c_s} \sim 0.4$ far from the defect, in a homogeneous and steady flow. In our case, it is not possible to use such a criterion, as we have a finite size, time dependent population. The only way to determine the experimental conditions for vortex nucleation is therefore to look at the local fluid velocity and sound velocity on the obstacle perimeter. While the fluid velocity vector field can be directly extracted from the polariton field phase gradient, the local speed of sound can be estimated from the density map, as shown in the next paragraph.

Estimation of the local speed of sound The value of the local sound velocity is determined from the density map, originally in arbitrary units, which needs to be scaled to the blue-shift ng . We do not have access to the time-dependent blue shift. However, provided the slow-down of the polariton population observed in the momentum space dynamics (Fig. 7.6 (c)), we can assume that the major contribution to the blue-shift of the polariton branch at $k_{//} = k_{pump}$ comes from the beginning of the dynamics. This blue-shift can be estimated from Fig. 7.5 (i) to be of the order of $0.8meV$ (with an estimated uncertainty of $0.2meV$). Provided the maximum polari-

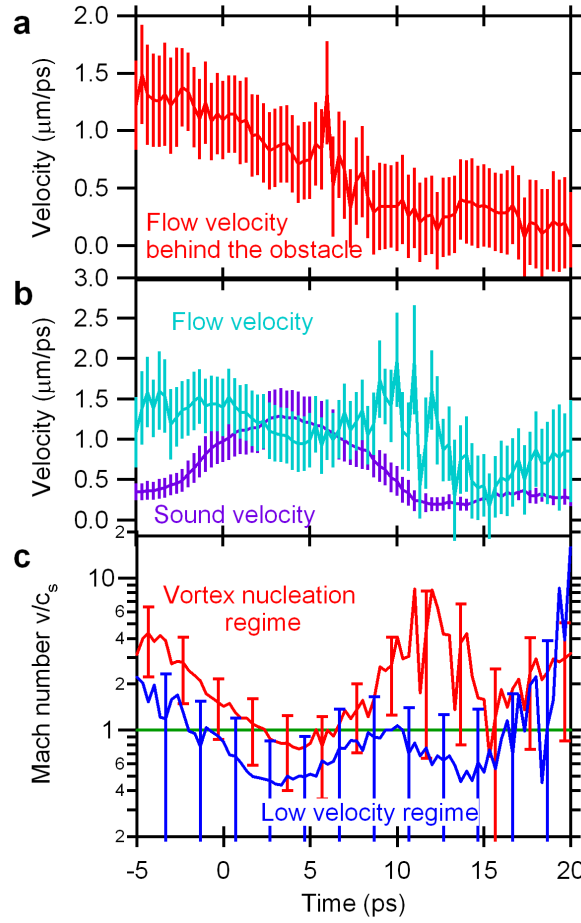


Figure 7.12: **Quantitative measurements** (a) Flow velocity measured behind the defect (in the region delimited by the dashed white square in Fig. 7.9 I), for the vortex nucleation regime. An almost constant slow down can be observed. The small jump observed at around 6ps is due to a phase singularity passing in the vicinity of the region of interest. (b) Flow velocity and sound velocity measured on the obstacle perimeter (in the region delimited by the plain white square in Fig. 7.9 I), for the vortex nucleation regime. The error bars on the velocity take into account the standard deviation of the linear fit of the phase gradient, as well as a systematic error coming from the determination of the phase gradient induced by the setup alignment. The error bars on the sound velocity take into account the standard deviation on the averaging in the region of interest, as well as the systematic relative error on the scaling method. (c) *Red curve*: Mach number $\frac{v}{c_s}$ on the obstacle perimeter, for the vortex nucleation regime. *Blue curve*: Mach number $\frac{v}{c_s}$ on the obstacle perimeter, for the low velocity regime. The green line on $\frac{v}{c_s} = 1$ indicates the limit between subsonic flow (below the line) and supersonic flow (above the line).

ton emission intensity (integrated over the whole emission) occurs at a delay of 1.7ps (inset in Fig. 7.11), we plot an histogram of the number of counts detected at that delay (Fig. 7.11 (a)). Each bar in this histogram indicates the number of pixels that detected a given amount of counts. In Fig. 7.11 (b), we have multiplied the number of pixels by the number of counts itself. The obtained distribution is expected to mimic the emission spectrum, and shows a global maximum around 50×10^6 counts. With this we can estimate the local blue-shift by scaling the number of counts on

the density maps by a factor $\frac{0.8\text{meV}}{50 \times 10^6 \text{counts}}$. This allows to extract a rough estimation for the local speed of sound along the dynamics (it more likely gives a lower bound to its value, as the averaging of the blue-shift probably yields to an underestimation of its value).

Figure 7.12 (b) shows the values of the fluid velocity and speed of sound measured on the obstacle perimeter (averaged in a region delimited by the plain white square in Fig. 7.9 I) along the dynamics. While the fluid velocity is staying above a value of $0.95 \pm 0.35 \mu\text{m}/\text{ps}$, the sound velocity rises above the value of the fluid velocity. The corresponding values of the Mach number $\frac{v}{c_s}$ are displayed in Fig. 7.12 (c) (red curve), showing that a value of $\frac{v}{c_s} \sim 1$ is obtained on the obstacle perimeter at the onset of the vortex nucleation. For comparison, the values of the Mach number on the obstacle perimeter for the low velocity regime are plotted in blue in Fig. 7.12 (c). They show that the flow remains mostly subsonic (or superfluid, in the sense of the Landau criterion) during the major part of its dynamics. The damping of polariton-polariton interactions finally allows to enter the vortex nucleation regime.

7.8 Numerical simulations based on the Gross-Pitaevskii equations

7.8.1 Numerical resolution of GPE

We solve iteratively the generalized Gross-Pitaevskii equation for the lower-polariton mode ψ , described in Section 1.5,

$$i\hbar \frac{d}{dt} \psi(\mathbf{r}, t) = \left(-i\frac{\gamma}{2} + \sum_k \hbar\omega_k |k\rangle\langle k| + g|\psi(\mathbf{r}, t)|^2 \right) \psi(\mathbf{r}, t) + V\psi(\mathbf{r}, t) + F_p(\mathbf{r}, t). \quad (7.4)$$

The potential V is made of a $3\mu\text{m}$ large and 1meV high obstacle. Our model accounts for the dissipation of polaritons at rate $\frac{\gamma}{\hbar}$, and a 1ps -long initial excitation of the system $F_p(r, t)$. The polariton-polariton interaction is assumed to depend linearly on the polariton density $|\psi(\mathbf{r}, t)|^2$ with a coefficient g , and $\sum_k \hbar\omega_k |k\rangle\langle k|$ is the kinetic Hamiltonian, diagonal in the plane wave basis $|k\rangle$, with eigenvalues $\frac{\hbar^2 k^2}{2m}$. For the resolution in the real space, k_j is transformed into $-i\frac{\partial}{\partial j}$. The parameters used in the simulations are: $\gamma = \frac{\hbar}{15\text{ps}}$, $g = 0.01\text{meV} \cdot \mu\text{m}^2$, $m = 0.7\text{meV} \cdot \text{ps}^2 \cdot \mu\text{m}^{-2}$. The excitation intensity for the high power experiment corresponds to a maximal polariton density of $120\mu\text{m}^{-2}$ on a $20\mu\text{m}$ large spot, and for the low power experiment to a maximal polariton density of $1.2\mu\text{m}^{-2}$.

7.8.2 Agreement with experiments

The three flow regimes observed experimentally are extremely well reproduced by the numerical simulations. For comparison, simulations are shown in Fig. 7.13 (standard Rayleigh scattering in the low density flow), Fig. 7.14 (vortex pair nucleation for a $1.2\mu\text{m}^{-1}$ momentum wavepacket), and Fig. 7.15 (almost unperturbed flow in the $0.6\mu\text{m}^{-1}$ momentum wavepacket).

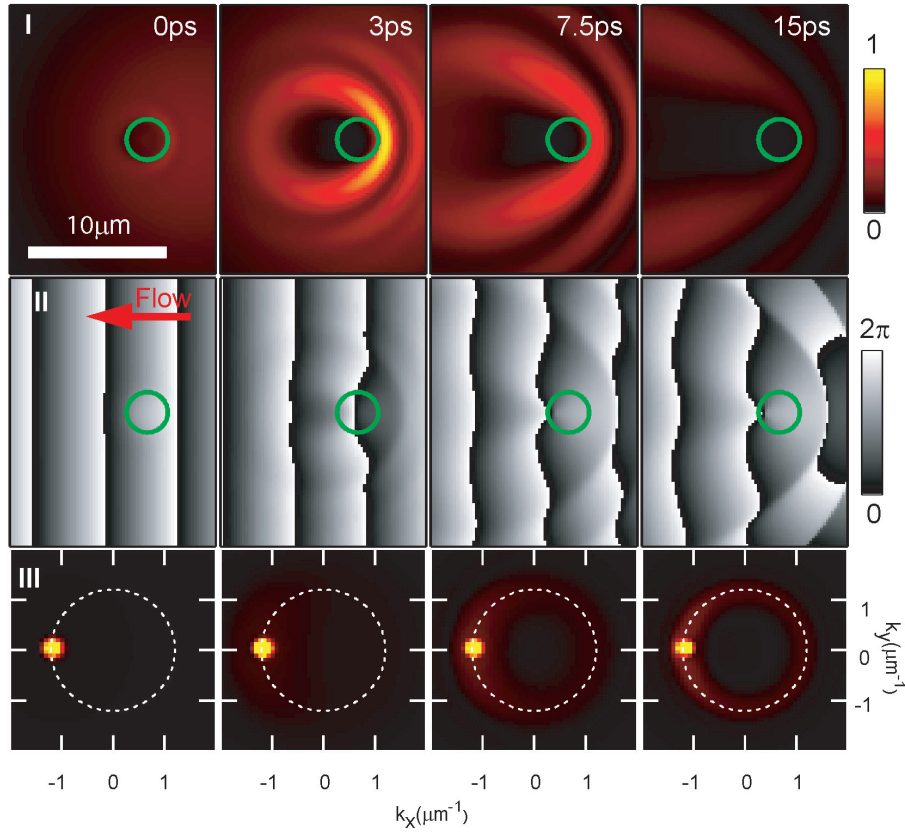


Figure 7.13: **Simulations: low density regime** Simulation of the low density, supersonic regime, reproducing the experimental features of the experimentally observed low density regime of Fig. 7.7. (I) and (II) density and phase profiles of the polariton fluid, displaying parabolic scattering wavefronts. (III) Momentum space dynamics, showing the appearance of a Rayleigh scattering ring. The white dashed circle indicates the expected position of the Rayleigh ring. Position and size of the defect are indicated by the green circle. Parameters: $k_{pump} = 1.2\mu m^{-1}$, excitation power $1.2\mu m^{-2}$ on a $20\mu m$ large spot.

In particular the vortex nucleation regime (Fig. 7.14) appears within a range of parameters close to our experimental findings. The low velocity regime (Fig. 7.15) is simulated by decreasing by a factor of 2 the initial polariton wavevector. An almost frictionless flow dominates the spatial dynamics at short times. On the other hand, when the initial polariton density is decreased below a maximum polariton density of $90\mu m^{-2}$ around the obstacle, the flow changes from a quantum fluid regime to the classical scattering behavior of a diluted polariton gas (Fig. 7.13).

Regarding the momentum space dynamics, the simulations reproduce the rise and decay of the Rayleigh ring for the low density regime (Fig. 7.13 III). For the high density regime, a qualitatively different behaviour is observed (Fig. 7.14 III): no Rayleigh ring is visible, and a spreading of the population in the momentum space is observed instead. There is however an important qualitative discrepancy (the only one so far) with the experimentally observed feature: in the experiment (see Fig. 7.6 (c)), the entire population undergoes a slow down, whereas in the simulation the major part of the population remains centered around k_{pump} . This might come from the fraction of the polariton population which interacts with the

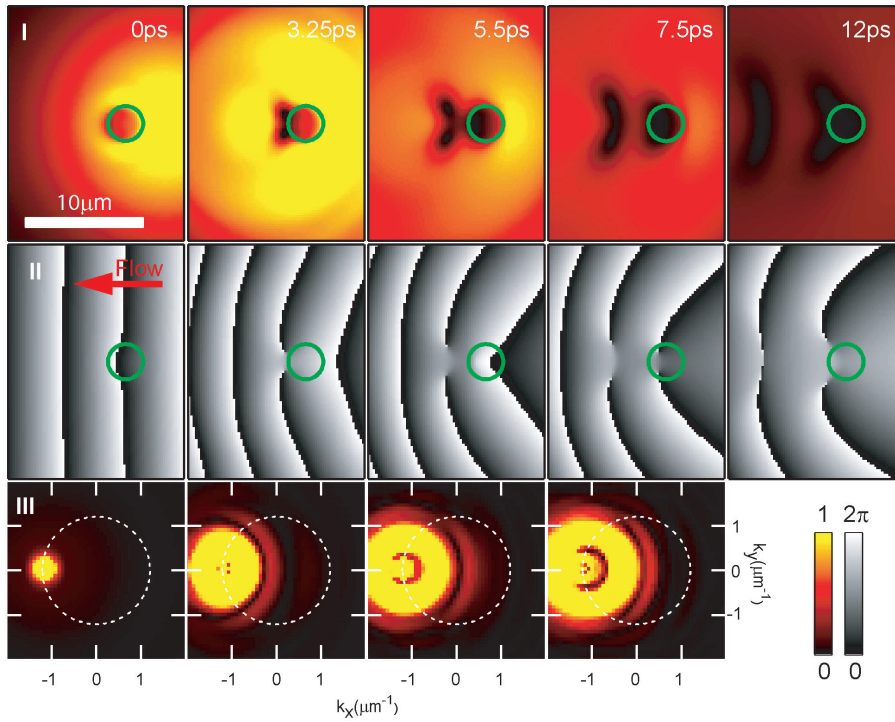


Figure 7.14: **Simulations: vortex nucleation regime** Simulation of the vortex nucleation regime, reproducing the features of the experimentally observed vortex nucleation regime of Figs. 7.6 (c) and 7.9. (I) and (II) density and phase profiles of the polariton fluid, displaying the hydrodynamic nucleation of two vortex pairs. (III) Momentum space dynamics, showing a spreading into the interior of the Rayleigh ring. The white dashed circle indicates the position that would be expected for a Rayleigh ring. Position and size of the defect are indicated by the green circle. Parameters: $k_{pump} = 1.2\mu m^{-1}$, excitation power $120\mu m^{-2}$ on a $20\mu m$ large spot.

obstacle or the surrounding disorder landscape: a more disordered landscape in the simulation leads to a larger fraction of the population slowing down. However, in the simulation, we were not able to produce a disorder landscape such that the entire population would slow down, as is experimentally observed.

7.8.3 Insights from simulations

The numerical simulations allow of course to measure the local fluid velocity and density. A snapshot of the computed phase profile is displayed in Fig. 7.16 (a), for the vortex nucleation regime, at the onset of the first vortex pair nucleation. Local values of the Mach number are represented by color lines, with a green thick line for $\frac{v}{c_s} = 1$. In order to compare the experimental findings of Fig. 7.12 (c), we plot in Fig. Fig. 7.16 (b) the time evolution of the Mach number on a small region close to the equator of the obstacle (small black and white circle in Fig. 7.16 (a)), using simulation parameters corresponding to the three flow regimes described previously (vortex nucleation regime, low velocity regime and low density regime). While the low density experiment always lies in the supersonic region (black curve), the high density experiments (blue and red curves) remain subsonic for a significant part of

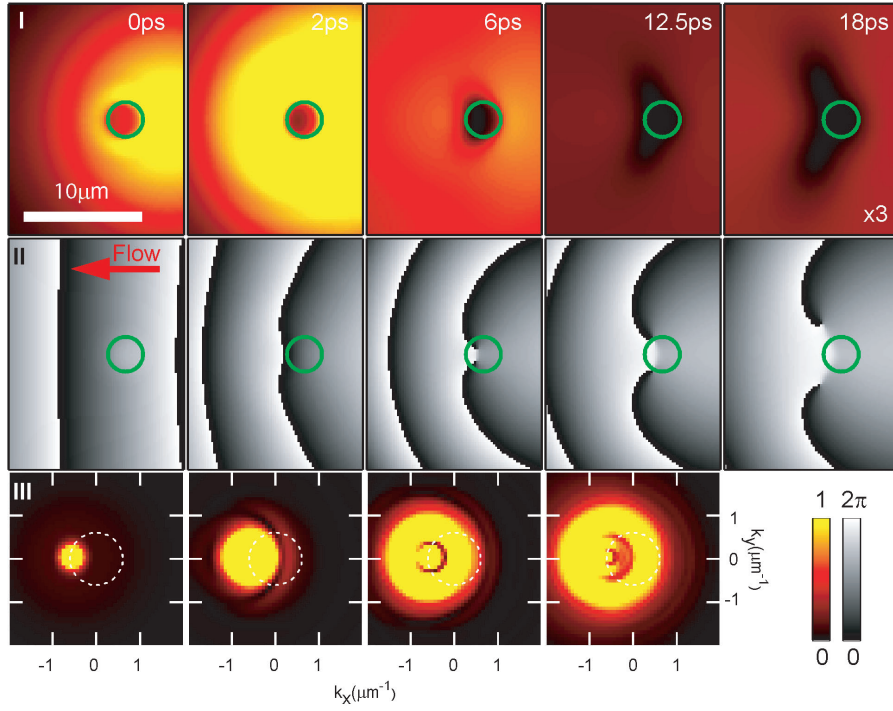


Figure 7.15: **Simulations: low velocity regime** Simulation of the low velocity regime, reproducing the features of the experimentally observed low velocity regime of Fig. 7.10. (I) and (II) density and phase profiles of the polariton fluid. A vortex pair is nucleated at long time, and stay on the defect for several picoseconds. Simulation show that the vortex pair is eventually dragged away from the defect at long time, when the fluid density is very low. This effect is not observed in experiment, as the low fluid density at long times hinder the measurement of the phase. Density values are multiplied by a factor three in the last density plot, for the sake of visibility. (III) Momentum space dynamics. The white dashed circle indicates the position that would be expected for a Rayleigh ring. Position and size of the defect are indicated by the green circle. Parameters: $k_{\text{pump}} = 0.6 \mu\text{m}^{-1}$, excitation power $120 \mu\text{m}^{-2}$ on a $20 \mu\text{m}$ large spot.

their dynamics. Similarly to the experimental findings, the low velocity regime (blue curve) remains subsonic for a longer time than the vortex nucleation regime (red curve). Moreover, consistently with the argument originally developed by Frisch *et al* [110] for the transition to turbulence in a superfluid, we find in the simulation that the phase accumulation resulting in vortex nucleation starts at the precise time when the fluid velocity gets equal to the sound speed (when $\frac{v}{c_s} = 1$) on the obstacle equator. The nucleation of the vortex pair is just following this event; the higher the initial velocity, the closer the vortex nucleation to the initial phase accumulation (this effect is analogous to the lowering of the vortex shedding frequency predicted for homogeneous equilibrium BEC when the fluid velocity gets close to the critical velocity [110, 111]). The vortices are dragged away from the obstacle at later times, in a time range corresponding to the experimental findings.

The numerical simulations also allow to evidence the role of the polaritonic nonlinearities in the nucleation process. Indeed, there are no vortices nucleating in the wake of the obstacle if the interaction constant is set to 0. The hydrodynamic nucleation process can therefore be differentiated from linear optical processes, like

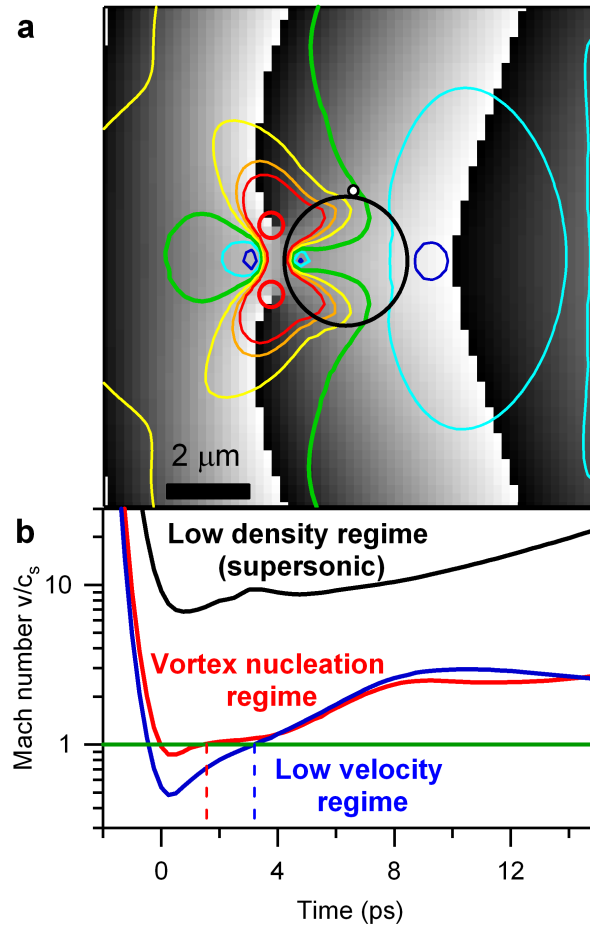


Figure 7.16: **Nucleation criterion: numerical evidence** (a) Numerical simulation of the phase profile, with simulation parameters corresponding to the vortex nucleation regime, at the onset of vortex nucleation. The obstacle is indicated with a black circle, and the flow is directed leftward. The thick red circles show the vortex positions. Color lines indicate lines of equal Mach number. The green thick line indicates a local Mach number of 1, blue lines indicate a local subsonic flow ($\frac{v}{c_s} < 1$), yellow to red lines indicate a local supersonic flow ($\frac{v}{c_s} > 1$). (b) Evolution of the Mach number at the equator of the obstacle (small black and white circle in (a)), using simulation parameters corresponding to the vortex nucleation regime (red curve), to the low velocity - mainly subsonic- regime (blue curve) and to the low density -linear- regime (black curve). The phase accumulation starts when the fluid velocity crosses the sound velocity ($\frac{v}{c_s} = 1$) on the obstacle equator (dashed lines) systematically resulting in the nucleation of vortices.

the generation of vortex lattices whenever three or more plane waves interfere.

Eventually, if randomly distributed disorder, scaled to match the experimental Rayleigh ring raising time (0.7meV for 5.7ps rise time), is added to the potential landscape the vortex pair dynamics tends to get more complicated. Disorder can hinder vortex pair recombination, or may even lead to the appearance of additional phase singularities in areas where the polariton density is very low. Indeed, creation of a vortex in a low density area costs very few energy and can be triggered by any perturbation like disorder. They are however not considered as “hydrodynamically nucleated vortices”, as they do not consist in a minimum of density in a dense fluid

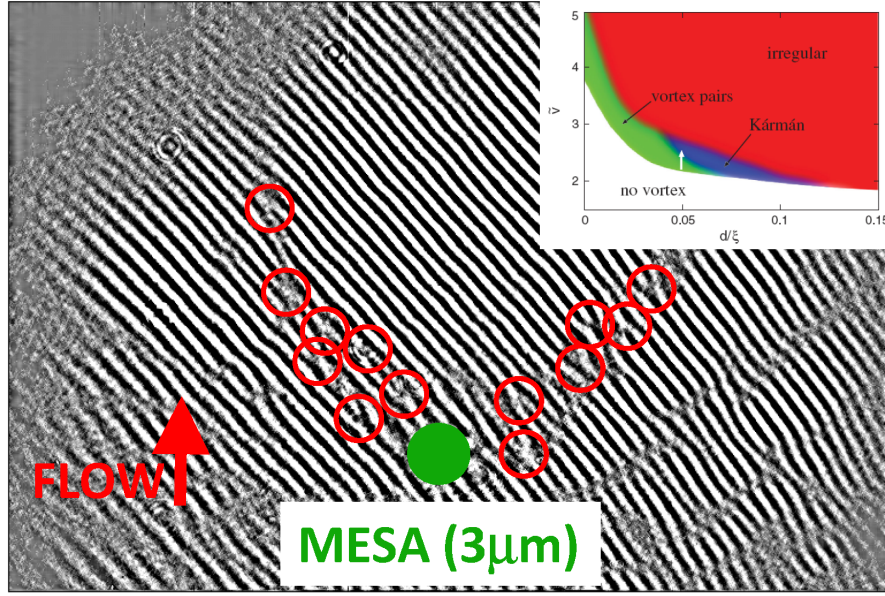


Figure 7.17: Preliminary measurement: Interferogram of a turbulent flow, for an initial in-plane momentum of $1.2\mu\text{m}^{-1}$. This snapshot is taken a few picoseconds after the injection of the fluid. The obstacle is a $3\mu\text{m}$ diameter trap (mesa), providing a nearly circular attractive potential of $\sim 7\text{meV}$ depth. A large number of vortices are visible, aligned along two streets. They are indicated by fork-like dislocations and circled in red. Inset: phase diagram reproduced from Sasaki *et al.* [115], showing different possible quantum turbulence regimes in an homogeneous atomic BEC, with respect to the fluid velocity and the obstacle size.

area and do not necessarily appear in the wake of the obstacle.

7.9 Towards Bénard-von Karman streets and full turbulence: preliminary results

An very direct and interesting follow-up of this work is to take advantage of the polariton traps described in the preceding chapters. Indeed, these latter constitute nearly circular obstacles of different sizes. This should allow to address additional flow regimes, such as the quantum counterpart of Bénard-Von Kármán streets, or fully turbulent regimes (i.e. with a chaotic proliferation of vortices). A recent theoretical work based on the numerical resolution of the Gross-Pitaevskii for an homogeneous equilibrium BEC [115] has calculated a phase diagram for the different possible flow regimes. This phase diagram is reproduced in the inset of Fig. 7.17, and is established with respect to the fluid velocity (normalized to the speed of sound) and the obstacle size (normalized to the healing length). If our experimental conditions does not allow to inject polariton with much higher velocities than the one used in this chapter, we can use traps of much larger size, using the $10\mu\text{m}$ and $20\mu\text{m}$ diameter traps. Of course the time-dependent fluid density will have to be taken into account as well, as it will make both the sound velocity and the healing length vary with time. Some very promising preliminary measurements have already

been taken. The fact that the obstacle is a deep attractive potential seems to play a determining role in the nucleation and trajectory of vortices, and lead to the creation of Bénard-Von Kármán-like streets, even with the small $3\mu\text{m}$ diameter mesas (see Fig. 7.17).

7.10 Conclusion

We have reported in this chapter the observation of quantum turbulence in a polariton fluid. Using time-resolved interferometry, we have evidenced the nucleation of vortex pairs in the wake of an obstacle. Our experiment allows to observe the nucleation mechanism with a phase resolution, and to follow the motion of the vortices, whose paths are influenced by local disorder and microcavity sample wedge. We have also shown how a general slow down of the polariton wavepacket necessarily accompanies the vortex nucleation, as a consequence of the peculiar polariton dispersion shape when the fluid velocity crosses the sound velocity. The nucleation conditions have been established in terms of local fluid velocity and sound velocity on the obstacle perimeter. Our results are successfully reproduced within the framework of Gross-Pitaevskii equations. Our experiment demonstrates the huge potential of semiconductor microcavities for the study of turbulence in quantum gases. Key advantages are the direct optical access of the polariton field (in real and momentum spaces), the absence of trapping potential, and the operation at cryogenic temperature (and possibly at room temperature in state-of-the-art Nitride-based microcavities [27]). The ability to control polariton properties opens the way to subsequent breakthrough experiments such as the scattering of a wavepacket on engineered obstacles of different sizes and shapes, which will provide the possibility to address the quantum counterpart of Bénard-Von Kármán vortex streets and fully turbulent regimes [115].

Part IV

Perspectives

Chapter 8

Experiment Proposals

In this chapter we list some experiments that could be performed as a follow-up of the work presented in this thesis. Some of these proposals can be realized on the present microcavity sample, and some other will require the growth of a new patterned microcavity sample (the details concerning the fabrication of a new sample are gathered in the next chapter). Let us mention that a new mask for the photolithography, with numerous new confining potential shapes and sizes is ready to be imprinted on a new sample. This mask (referred in the following as the *new mask*), was designed by Ounsi El Daïf, and offers a lot of new experimental possibilities. Photographs of the result of photolithography using the new mask on photosensitive resin deposited on a test wafer are shown in Fig. 8.1.

This chapter is not intended to be deeply detailed, but is merely there to have a written trace of possible subsequent experiments, and a brief record of the corresponding literature.

8.1 Spatially resolved spectroscopy

The usefulness of the imaging spectroscopy tool presented in chapter 3 for characterizing specific confinement potentials has already been mentioned. It could also be used on a larger scale in order to characterize the disorder landscape of the microcavity. A large scale disorder map of the sample would be very useful to identify defect-free areas to study polariton propagation, or natural defect shapes that could serve as obstacles for fluid dynamics experiments. Beside this, a PL map (emission energy and linewidth) would be interesting in itself: the geometry of the disorder landscape (for example, if it is aligned along crystallographic axes) may give interesting informations about the sample structure or the effect of aging (the sample is now 6 years old). Moreover, using a polarization sensitive detection may allow to detect and map polarization splitting effects, and correlate them with the disorder landscape or the excitonic and photonic contents of the polaritons.

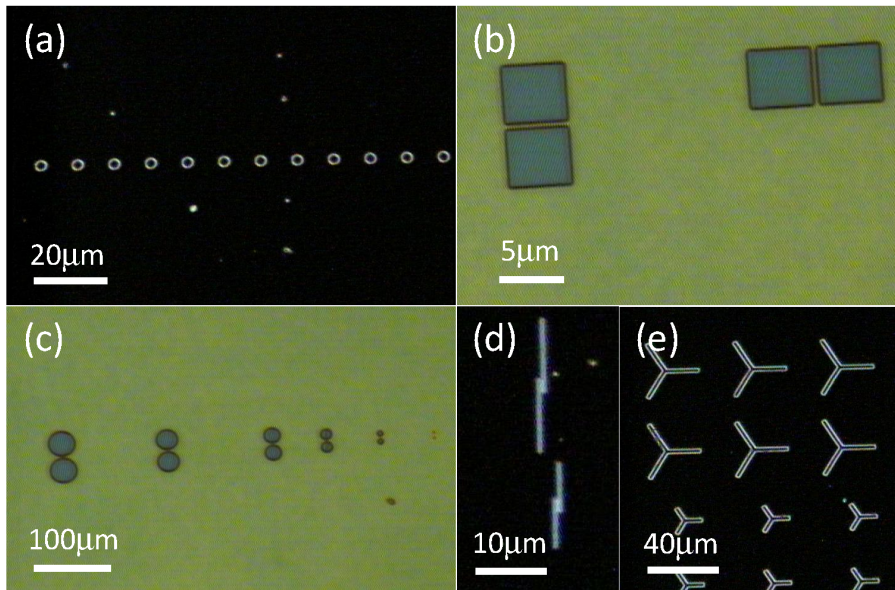


Figure 8.1: Microscope images of photosensitive resin deposited on a test wafer. The photolithography has been performed using the new mask. (a) Dark field photograph of a trap array. (b)-(c) Bright field photographs of coupled traps. (d) Dark field photograph coupled 1-dimensional traps. (e) Dark field photograph of Y-shaped 1-dimensional traps that can serve as couplers or splitters.

8.2 Quantum fluidics...

8.2.1 ...using the present microcavity sample

The experimental results shown in chapter 7 demonstrate the potential of semiconductor microcavities for the study of quantum fluids and turbulence. As already mentioned, the next logical step is to use the polariton traps existing on the sample to address the quantum counterpart of Bénard-Von Kármán streets and fully turbulent regimes [115]. The preliminary measurements indicate that the attractive nature of the confinement potential plays a significant role in the nucleation and trajectories of vortices and soliton lines. A possible outlook could be to tune the effective confinement potential by injecting a polariton population in the trap, using an independent *cw* laser. It would be a way of optically engineer the polariton landscape, and an alternative to the creation of optical defects by means of a blue-detuned laser, as recently demonstrated in Ref. [132].

An other interesting experiment would be to quantify the role of the sample wedge on the wavepacket propagation. This effect has already been qualitatively observed in the experiments presented in chapter 7. The acceleration of polariton by the potential gradient induced by the wedge shape has already been reported [133]. The nucleation mechanism might be favored or hindered, depending if the potential gradient is in the direction of the flow or not.

8.2.2 ...using new potential geometries

Of course, the patterning of repulsive obstacles of different sizes on a new sample would provide a fantastic laboratory for studying the textbook hydrodynamic nucleation of vortices in the wake of circular impenetrable obstacles. The new mask contains inverted circular and square mesas of various sizes between $0.5\mu\text{m}$ and $5\mu\text{m}$ that were designed for this purpose. It also contains arrays of traps (with various trap sizes and inter-trap spacings), that could be used as a diffraction grating (Fig. 8.1 (a)).

It could be also very interesting to design new obstacles to be patterned on a future sample. For examples barriers with small openings of various sizes, in order to study the superfluid propagation through the opening. Thanks to the versatility of the etching method, even more exotic obstacles could be designed, such as the profile of a wing.

8.2.3 Time-resolved blue-shift

Eventually, let us mention that a very useful supplementary experimental asset would be to record the blue-shift of the polariton emission with a time resolution (for example by installing a streak camera at the output of the spectrometer). This would help to much more precisely scale the polariton density and blue-shift. We saw that this scaling is of crucial importance for determining the sound velocity or the healing length in the polariton gas. Moreover, combining time-resolved measurements of the blue-shift and of the momentum space dynamics would allow to understand better the rich population dynamics resulting from the dynamical evolution of the excitation spectrum. If we add to this the momentum space tomography, we would be able to make a full map of the population dynamics, and to understand better the underlying physics.

In particular, measurement of the dynamical blue-shift correlated with time-resolved measurement of the polariton density may help to test the limits of the Gross-Pitaevskii model, which assumes that the blue-shift is proportional to the polariton density. A recent experiment [24] has shown that the contribution of a dark reservoir should be accounted for, even in the case of resonant excitation.

8.3 Quantum optics

Squeezing The generation of squeezed light states (already demonstrated in planar semiconductor microcavities [134]) is expected to be more efficient in the absence of a continuum of states. A recent theoretical work [135] has analysed the effect of the confinement by disorder on the squeezing of the polariton states. The polariton traps of the present sample constitute a controlled disorder, with three confinement sizes (plus the non-confined polaritons), and thus various energetic separations between the confined states. Measuring the squeezing of the emitted light would allow to probe the transition from fully confined - and well separated - states to a continuum, and test the predictions of Ref. [135]. This would open the way to the use of laterally confined polaritons for squeezing and quantum noise reduction in quantum

optics.

Quantum blockade The new mask contains circular confinement geometries of very small size, down to $0.5\mu m$ diameter, in which the highly non-linear polariton-polariton interaction is expected to give rise to quantum blockade and single photon emission under resonant excitation [17, 60].

Coupled structures Coupled circular and square polariton traps are also present on the new mask, with various trap sizes and distances between the coupled structures (Fig. 8.1 (b)-(c)). These structures can be used to explore a variety of Josephson-like oscillations under resonant excitation [55], and have also been recently proposed for the emission of single photons [18].

Trap arrays A theoretical paper predicts the fermionization of photons in a periodic array of coupled cavities, as a result of the combination of the non-equilibrium nature of the polariton system with the strong polariton-polariton interactions [56]. It would be worth designing such structures on a future mask. Let us mention that the new mask already contains linear arrays of small traps (Fig. 8.1 (a)), which could be used to study quantum phase transitions in strongly interacting many-body systems [136].

Trap lattices In a longer term perspective, the realization of coupled trap lattices may allow the realization of a quantum simulator, analogously to optical lattices for neutral atoms. Controlling the spacing between the traps and the polariton density, it would be possible to probe the superfluid-Mott insulator transition [137]. Numerous other experiments, inspired from the community of optical lattices [138], could be realized. Let us note that, following the demonstration of polariton diodes [32, 34], the quantum simulator might be electrically pumped.

8.4 Miscellaneous

Polariton neurons The recent demonstration of spin multistability on our sample [24] opens the way to the experimental realization of the proposal for polaritonic circuits [19]. The new mask contains 1-dimensional traps that can be exploited for this purpose (Fig. 8.1 (d)), as well as Y-shaped splitters or couplers that can be used to experimentally demonstrate the polarization sensitive logic gate proposed in Ref [19] (Fig. 8.1 (e)).

Confined polariton states: study of polarization A follow-up of the the work concerning the selective excitation of confined states presented in chapters 4 and 5 would be to exploit the polarization (or spin) degree of freedom. All the experiments in these chapters were performed using a linearly polarized pump and a linearly polarized detection. However, due to the polarization degree of freedom, the polariton field can be projected on the σ^+ and σ^- basis (or spin up and spin down). Recent experiments have demonstrated that the two species can be excited

independently [139], and exhibit independent bistability thresholds, leading to state-of-the-art multivalued spin switching [24]. The work of Taofiq Paraïso and co-authors [24] was performed on the ground state of a $3\mu m$ trap. It would be extremely interesting to observe the effects of different polarized excitation (and to use as well a polarization sensitive detection) on the excited states, such as the $(n = 1, m = 1, e)$, $(n = 1, m = 1, o)$, for which a polarization splitting should accompany the lifting of the cylindrical symmetry.

Chapter 9

New sample design and fabrication

All the experiments that have been presented in this thesis were performed on the same sample, which is the only one patterned microcavity sample so far. A significant part of my PhD (mainly the first two years) was devoted to the fabrication of a new sample, using the new mask briefly introduced in the last chapter. It is a major stake, considering the large number of new experimental opportunities that new confinement geometries can offer. However, the MBE that allowed to grow the first sample was out of order, and it was decided to use a second-hand MBE for the growth of the new sample.

Despite all the efforts of our grower, this MBE kept having technical problems. A consequent time has been devoted to the characterization of epitaxial layers (QW layers, DBRs and cavities), but no usable sample came out of it, and the machine was abandoned. Now, a brand new MBE machine is getting installed, and will be ready soon to grow new structures. This chapter is here to have a record of the main issues encountered during the fabrication, and of novel sample designs that we imagined in order to solve these issues. I hope it will be useful for the people who are going to undertake the fabrication of the future sample.

9.1 General design: comment on the number of quantum wells

The existing patterned microcavity sample is containing a single embedded InGaAs QW, and thus could not reach the threshold for stimulated relaxation in the confined states because of the saturation of the strong coupling (see section 2.2.3). As the polariton traps were primarily fabricated to demonstrate polariton lasing, it was thus decided that the new sample would contain more QWs, in order to increase the exciton saturation density. Other groups working with different confinement schemes have subsequently reported polariton lasing in microcavities containing 12 to 21 *GaAs* QWs in a *Ga_{0.05}Al_{0.95}As* [22, 54], and featuring Rabi splittings of $\sim 15\text{meV}$. Later on, polariton condensation has even been reported in a planar ultra-high finesse cavity (26 and 30 DBR pairs for a quality factor of $Q = 12000$) containing 21 *GaAs* QWs [140]. We have therefore focused our efforts on fabricating a cavity with at least 12 QWs, grouped in three stacks positioned at the anti-nodes of the electromagnetic field in a $3\lambda/2$ cavity. Although we were able to produce high finesse

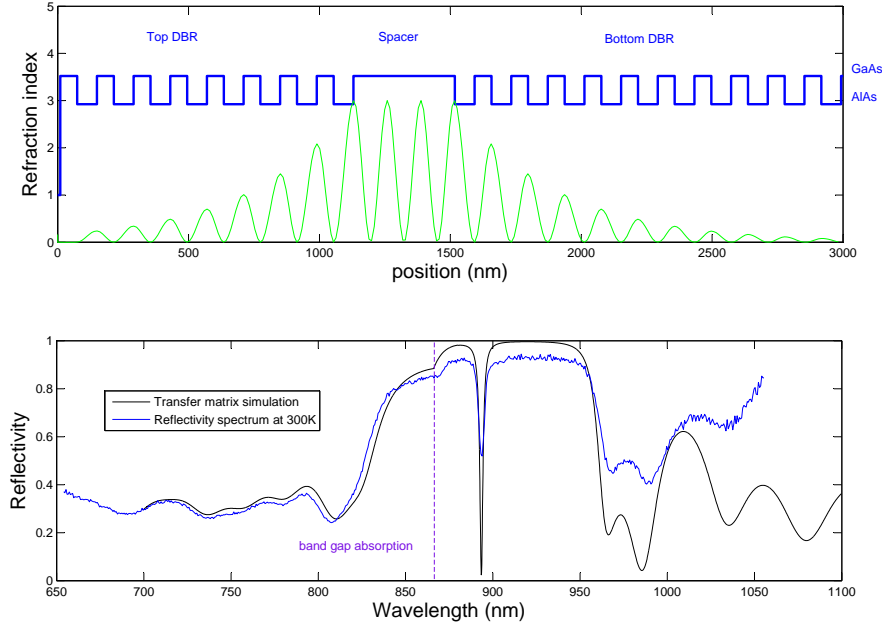


Figure 9.1: **Optical characterization: example.** *Top panel:* structure of a $3\lambda/2$ cavity with 8(10) pairs $Al/GaAs$ for the top (bottom) DBR, used for determining the growth rates of the MBE. *Bottom panel:* Comparison between the white light reflectivity spectrum (normalized to the white light spectrum), and the transfer matrix simulation, which includes the effect of band gap absorption (below $870nm$). A wavelength dependent refractive index is used, fitted from the data of Zollner *et al.* [141] and www.luxpop.com for room temperature.

cavities and QWs of reasonably high quality ($\gamma_X^* \sim 1meV$) we were never able to produce a microcavity in the strong coupling regime with the second-hand MBE. We have not been able to find whether it was due to unexpected irregular growth rates or to some other reason. We must mention that stacks of $In_{0.05}Ga_{0.95}As$ QWs in $GaAs$ are not usual at all, as these latter are not as deep as the $GaAs$ QWs in $Ga_{0.05}Al_{0.95}As$ used in the other groups, and may therefore suffer from inter-QW coupling. The effect of coupling between the $InGaAs$ QWs of a stack should therefore be carefully studied.

I would here like to raise a point which seems very important to me. In my opinion, it is not necessary at all to achieve the bosonic stimulation in our future sample. Indeed, polariton BEC and lasing have been already demonstrated in $GaAs$ based microcavities by several other groups by now, in various configurations [22, 53, 54, 66, 140]. It is therefore not a breakthrough experiment anymore. I hope that the material presented in this thesis¹ convinced the reader that an extremely rich phenomenology can be observed in resonantly injected polariton gases. These latter share the coherence, macroscopic occupancy and non-equilibrium nature of

¹And the work of my colleagues: Taofiq Paraíso, Roland Cerna and Verena Kohnle [24, 73, 86, 107, 142].

the polariton BEC.

The fact that the coherence is not spontaneous, but inherited from the driving field is not really a drawback. The possibility to control the polariton energy, momentum and density with the laser field are indeed huge advantages of the resonantly injected polariton gas over the polariton BEC. Moreover, the reader may have noticed that virtually all the experiment proposals mentioned in the previous chapter 8 work for resonant excitation. For these reason, I strongly suggest in the future not to focus on the growth of a microcavity with 12 or more embedded QWs, because 1 or 3 *InGaAs* QWs would be enough for fully exploiting the possibilities offered by new confinement geometries.

9.2 Fabrication of the sample

9.2.1 Characterization methods

The characterization methods are quite standard, and already described in Ounsi El Daïf's thesis [67].

The growth rates of the MBE machine are determined by growing test optical structures which are characterized using white light reflectivity. The comparison of the reflectivity spectrum with transfer matrix simulations (based on a core code initially written by C. Ciuti) allows to extract the growth rates of the MBE machine for the *GaAs* alloy and the *AlAs* alloy. The ideal characterization structure is an empty cavity (see Fig. 9.1 for an example), as it allows to differentiate the effect of *GaAs* and *AlAs* (it would not be the case with a single DBR). This method also allows to determine the wedge shape of the sample [67]. An alternative solution to characterize the growth rates of the MBE machine would be to use X-ray diffraction.

The optical properties of the QWs and bulk materials are determined by photoluminescence measurements at liquid helium temperature, using a HeNe laser for optical pumping.

9.2.2 Clean room processing

The different steps for the patterning of the microcavity spacer are described in Ounsi El Daïf's thesis [67]. I have ensured that I was able to reproduce the process in the clean room, and that the parameters used for the photolithography of the epoxy resin given in Ounsi's thesis were compatible with the smallest structures of the new mask. Images of the resin after the photolithography are shown in Fig. 9.2. The smallest structure size ($0.5\mu m$) and the smallest separations ($0.4\mu m$) are resolved. Exotic structures are also shown. This demonstrates the high fidelity and the versatility of the imprinting of the mask.

The cavity spacer is then patterned using selective wet etching of the *GaAs*. The depth of the etching is controlled by the insertion of thin *AlAs* etch stops. The depth of the etching can be checked using white light reflectivity, because the thickness of the "cavity" formed by the bottom DBR and air is different for the etched and non-etched parts (Fig. 9.3). For a λ cavity, the shift of the optical mode

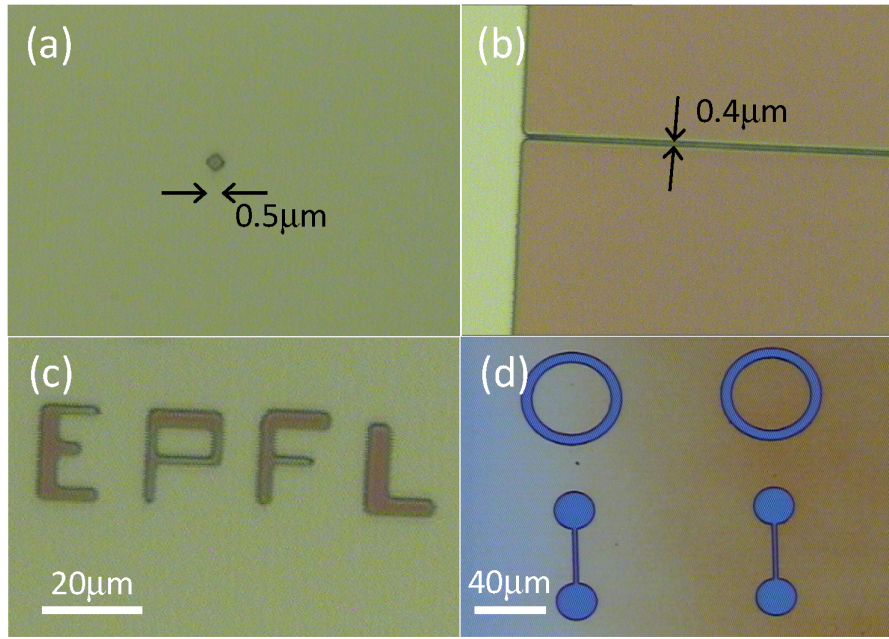


Figure 9.2: Microscope images of the photosensitive epoxy resin *S1805* deposited on a test wafer. The photolithography has been performed using the new mask. Small structures and exotic structures are shown. (a) $0.5\mu\text{m}$ diameter trap (smallest trap size of the mask). (b) Two square traps separated by a $0.4\mu\text{m}$ barrier (smallest barrier size of the mask). (c)-(d) Exotic structures.

gives directly the depth of the etching. In my opinion, this intermediate check can be skipped, as the use of etch stops has proven to be very reliable so far.

Then the sample is cleaned and brought back to the MBE, where an *in-situ* hydrogen plasma cleaning is performed before regrowing the top DBR.

9.2.3 Alternative to the regrowth: wafer bonding

Eventually, we would like to mention an issue that was raised when using the second hand MBE machine. This latter did not have the possibility of performing *in-situ* plasma cleaning. This would have most probably been detrimental to the regrowth of the top DBR. We therefore studied an alternative technique known as wafer bonding. Please note that this was a prospective work, which was abandoned before obtaining very significant results. I am mentioning it here only to keep a trace of what has been done.

Wafer bonding (or wafer fusion) is a process already successfully used for the fabrication of VCSELs [143] or solar cells [144]. Hydrophobic wafer bonding between two cleaned and activated GaAs surfaces (with aligned crystallographic axes) allows ideally to bind the two surfaces with atomic forces, and recover monolithic GaAs. A tried and tested technique of surface cleaning and activation is the use of a plasma of hydrogen radicals [145]. However, discussing with Prof. Anna Fontcuberta i Morral from the Laboratory of Semiconductor Materials, it appeared that the fusion could be realized without plasma cleaning if the two sample surface are brought together after cleaning with acetone and isopropanol. The last step is the application of

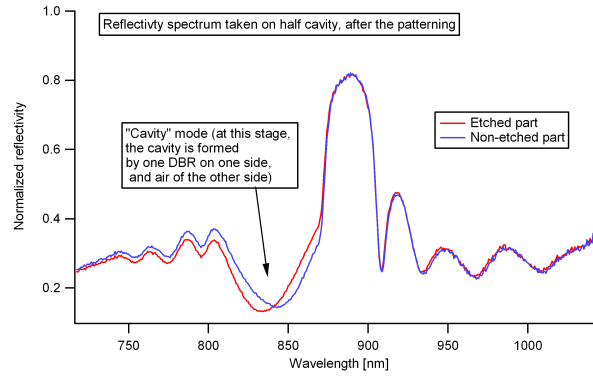


Figure 9.3: Room temperature white light reflectivity spectra (normalized to the white light spectrum) of a half cavity, i.e. the bottom DBR and cavity spacer. The patterning of the cavity spacer can be detected in the form of a shift of the “cavity” mode. It is a very broad resonance, as the “cavity” is here formed between the bottom DBR and air.

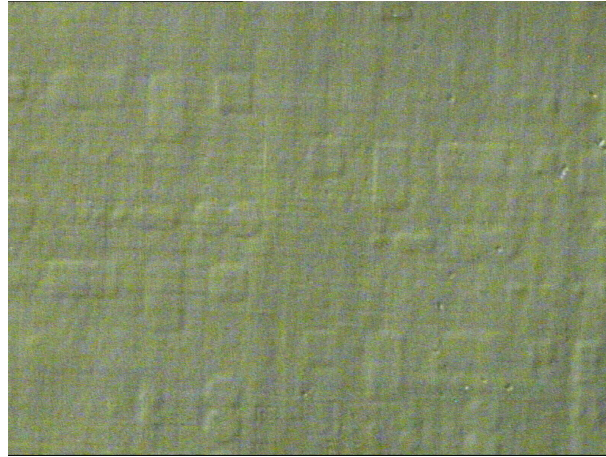


Figure 9.4: Microscope image of a patterned sample fused with the bonding machine of the Laboratory of the Physics of Nanostructures. This image, taken close to the edge of the wafer, is taken on the sample surface after removal of the top DBR substrate. The height of the patterning was of 8nm . The visible structures on the sample surface are a strong indication that the top DBR takes on the shape of the patterning.

pressure and heat in order to annihilate the residual interface.

We supervised a master student who was able to realize successful bondings, using a homemade clip for the application of homogeneous pressure, and heating in an oven at 300° [146]. The bonding showed a qualitatively good resistance to shear stress and to temperature shocks (from 300° into liquid nitrogen). The bonding of two DBRs, with 24 $Ga/AlAs$ pairs each, was realized, and a quality factor of $Q = 2300$ was measured on the resulting microcavity. This result is quite promising for a first test.

In parallel to these tests on flat sample surfaces, we tried to anticipate a major issue: what would be the effect of the cavity spacer patterning on the bonding. Would the bonding take place only on the non-etched parts? In this case the contact surface would be less than 5%, and would be detrimental to the solidity of the bonding. Would the top DBR take on the shape of the patterning? If yes, how

would this impact the quality of the optical cavity?

In order to answer these questions, we had the opportunity to make a wafer bonding test in collaboration with the Laboratory of the Physics of Nanostructures (LPN) of Prof. Kapon. They provided us with two MOCVD grown DBRs, and we patterned $8nm$ height structures on one of them using the new mask. The two DBRs were then fused together in the bonding machine of the LPN (usually used for bonding VCSEL structures), forming thus a λ cavity. A remarkable result is that after removal of the substrate of the top DBR, microscope images (Fig. 9.4) revealed the patterning on the surface of the sample. This is a strong indication that the top DBR takes on the shape of the patterning. This effect was however not observed on the central part of the sample, but only from half of its radius to the edge. This may be due to the thickness wedge of the sample (10% from the center to the edge), or to a non-homogeneous pressure applied during the bonding. Beside this, the optical properties were not very encouraging, as we measured a cavity mode linewidth of more than $2meV$, and were not able to detect any resonance shift resulting from the patterning [147]. This might be due to the negative impact of the bonding interface (situated in this configuration at the antinode of the cavity field) on the quality of the optical cavity.²

Due to the recurrent technical problems of the second-hand MBE, we did not have the occasion to make further tests. However, we imagined a different sample design that would allow to get round the issue of the low percentage of contact surface. This design has never been practically implemented (and may not work). Nevertheless, I will briefly describe it in the last paragraph, as it may serve one day.

New sample design for wafer bonding It is based on the following idea: instead of confining the cavity modes in a local extension of the cavity spacer, let us confine them in a locally deeply etched region, so deep that the local cavity mode $(n\lambda)_{etched}$ would catch up the $(n+1/2)\lambda$ mode of the surrounding non-etched region. A slightly smaller etching depth provides a lower resonance energy for the etched region than for the surrounding region, providing an effective confinement potential. The main advantage of this design is that, since the confining structure is the etched region, the contact surface would reach more than 95% (we would need to use a reversible epoxy resin - such as AZ5214 - in order to “revert” the mask). The scheme of the design and bonding process is shown in Fig. 9.5 for a $5\lambda/2$ confined mode.

Figure 9.6 shows transfer matrix simulations of this configuration (without QWs) for a resonance at $\lambda = 835nm$, where we have assumed that the etched region would be filled with air (or a refractive index equal to 1). In the bottom panel, the red curve is for the 3λ mode without etching, the blue curve for an etching depth of $175nm$ (bringing the $5\lambda/2$ mode of the etched region in resonance with the surrounding 3λ mode), and the cyan curve for a etching depth of $168nm$ (red-shifting the $\lambda/2$ mode of the etched region with respect to the surrounding 3λ mode, providing an effective confinement potential). Other etching depths would allow to

²In fact, looking at these spectra now, I have the impression that I was measuring a DBR mode instead of the cavity mode. It should be charged to the lack of experience during my first year of PhD... It would thus be worth examining this sample one more time.

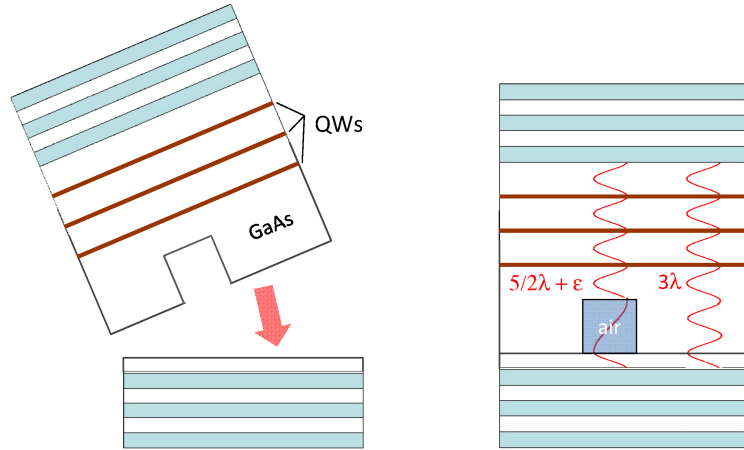


Figure 9.5: **New design for wafer bonding.** *Left:* Scheme of the bonding of the etched half cavity on the bottom DBR. *Right:* Sketch of the cavity modes in the etched and non-etched regions. Tuning the depth of the etching allows to tune the resonance of the etched region. The major advantage of this design is the large percentage of contact surface.

tune the depth of the confining potential (which could be chosen to be attractive or repulsive). In first approximation, for a $5\lambda/2$ resonance, a difference of $1nm$ in the etching depth would shift the resonance of $\frac{2}{5}(n_{GaAs} - n_{air}) \cong 1nm$. This precision in the etching is within the reach thanks to the use of etch stops. The simulation also shows that the bonding interface is located in a node of the cavity field, where this latter is the less sensitive to imperfections, advantageously. Eventually, let us mention that, in case of strong coupling, provided that the effective cavity length would be lower for the etched region, we would have to consider a renormalization of the Rabi splitting, according to eq. 1.14. The Rabi splitting would get larger for the modes in the etched region than for the surrounding continuum. Beside this, the practical realization of this design also contains unknowns. Would the $175nm$ deep etched region really be filled by air, or would the top DBR take on the shape of the patterning? In the second case, the depth of the etching would need to be $\sim 120nm$. We do not know either how regular would be the selective wet etching on such a deep etch.

We did not carry on investigating this wafer bonding technique, as the new MBE that is getting installed now has the possibility of *in-situ* plasma cleaning, lowering the interest into the alternative. Nevertheless, it can have an interest for the future, as it allows the half cavity and the top DBR (which can be small pieces of sample, not only wafers) to be characterized separately before being bonded together.

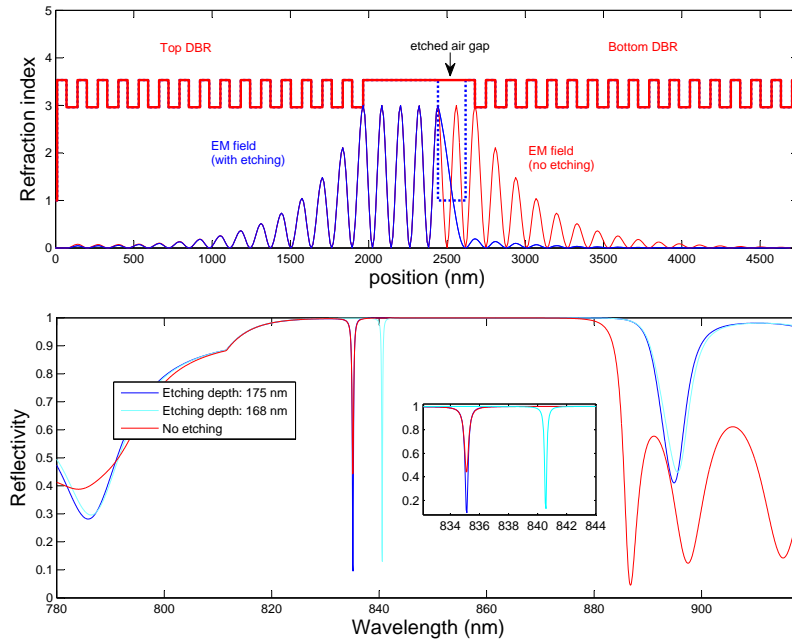


Figure 9.6: **New design for wafer bonding: transfer matrix simulations** The effect of the etching is simulated for a $5\lambda/2$ resonance at $\lambda = 835\text{nm}$. *Upper panel:* The thick red line is the non-etched structure. The thin red line shows the electromagnetic field intensity of the 3λ resonance. The dotted thick blue line shows the depth of the etched part, assumed to be filled with air (refractive index = 1). The thin blue line shows the calculated field intensity in the presence of the etching. This field corresponds to the $5\lambda/2$ resonance. For positions from 0 to 2400nm , red and blue curves are superimposed. *Lower panel:* The red curve is for the 3λ mode without etching. The blue curve is for a etching depth of 175nm (bringing the $5\lambda/2$ mode of the etched region in resonance with the surrounding 3λ mode), and the cyan curve for an etching depth of 168nm (red-shifting the $\lambda/2$ mode of the etched region with respect to the surrounding 3λ mode). Inset: zoom on the cavity modes.

Conclusion

We have presented in this thesis several original experimental results on the spectroscopy, imaging and manipulation of light-matter quasi-particles called exciton polaritons. These composite bosons can be manipulated and detected by optical means, and exhibit at the same time a dramatic non-linear response. They are therefore of great interest for the richness of their physics, as well as for future applications in the field of all-optical information processing. The sample under scrutiny was a GaAs-based patterned microcavity containing high quality polariton traps of various sizes.

- Chapter 3 was mainly dedicated to the spatially resolved spectroscopy of confined polariton states. We demonstrated a method allowing to retrieve the probability densities of the confined states at all energies. This tomographic method can be used to characterize any confinement geometry.
- In chapter 4, we probed the eigenstates of nearly circular polariton traps, by tuning the driving laser field to the eigenstate energy. We imaged the eigenstates with phase resolution and evidenced the effects of the trap ellipticity on the wavefunction geometry. These results constitute the first phase-resolved imaging of the eigenmodes of an elliptical resonator.
- In chapter 5, we showed how the excitation conditions can be tuned to control the emission pattern of confined polariton. In particular, we were also able to generate polariton states carrying an integer orbital angular momentum (or polariton vortices). These states, which are normally the eigenstates of cylindrically symmetric resonators, were obtained by exciting superpositions of eigenstates of the elliptical traps. We demonstrated that the topological charge of polariton vortices can be controlled by tuning the excitation spot position and incidence angle.
- In chapter 6, we carried on studying superpositions of confined polariton states, with a picosecond pulsed excitation. Adding a time resolution to our phase-resolved imaging setup, we were able to image the free evolution of a coherent superposition. Rabi oscillations between vortex and anti-vortex states were observed. This phenomenon was identified to the rotation of the state vector in the Poincaré sphere representation of orbital angular momentum states.
- The physics of quantum fluids was addressed in chapter 7. We studied the scattering of a polariton wavepacket on a structural defect, and reported on the nucleation of polariton vortices in the wake of the defect. We were able to

follow the motion of vortices in the microcavity plane. Phase-resolved images of the nucleation mechanism allowed to analyze the nucleation conditions in terms of local fluid velocity and density. These results, successfully reproduced by numerical simulations based on the resolution of the Gross-Pitaevskii equation, demonstrate the potential of semiconductor microcavities for the study of quantum turbulence.

- Eventually, in chapters 8 and 9, we have outlined possible follow-ups to this work, and mentioned some technical issues concerning the fabrication of a new patterned microcavity sample.

I hope that the reader has been convinced of the richness of exciton polariton physics. Since the demonstration of polariton BEC in 2006 [9], the number of publications in the field has literally exploded. Different complementary research axes are now explored by several groups in the field, both on the theoretical and the experimental side.

1. Following the work of Kasprzak *et al.* [9], several groups are investigating the mechanism of the condensation, in order to understand how spontaneous coherence and long range order can be established within the polariton gas [51, 108, 109, 148, 149, 150].
2. Triggered by the recent demonstration of polariton superfluidity [16, 129], the use of polaritons for addressing the physics of quantum fluids is just at its start. I am strongly convinced that the interest in this research field will keep growing. The ongoing works in this new field (including the one presented in the chapter 7 of this thesis) contributes to establish semiconductor microcavities as a incredibly accessible laboratory for studying the dynamics of non-equilibrium quantum fluids [96, 131, 132], complementary to ultra-cold atomic gases.
3. Eventually, device oriented research is also emerging in the polariton community, triggered by very interesting proposals for polaritonic logical devices [19, 20, 151] or single photon emission [17, 18]. The exploitation of polaritonic non-linearities along with their polarization degree of freedom offers indeed very promising perspectives, which are coming closer to reality with the demonstration of spin switching [139] and spin multistability [24]. This latter is a required building block for the realization of polariton-based all-optical memories (currently under investigation in our laboratory), and for the optical circuits and logic gates proposed by Liew *et al* [19]. We actually possess all the tools to implement the “polariton neurons” proposed in this paper, or the single photon emitter proposed by Verger *et al* [17], the only missing step being the fabrication of a new patterned microcavity.

The work presented in this thesis is a contribution mainly to the two last research axes (quantum fluid dynamics and polaritonic devices). We brought new elements to the understanding of the physics of polaritonic confinement in patterned microcavities, whose potential for subsequent breakthrough discoveries is enormous.

The tomographic technique and phase-resolve imaging are versatile tools that will certainly prove to be useful for the characterization of future polaritonic devices. Eventually, the phase resolved imaging of polariton dynamics allowed to bring new insights in the physics of quantum turbulence, and may also be used to demonstrate the working principle of future polaritonic circuits. As for more perspectives, I will simply refer to the chapter 8 of this thesis, where numerous experiments have been proposed, all of them within the reach for the coming years.

To conclude, I have to say that it was a great pleasure to work within this very enthusiastic research group led by Prof. Benoît Deveaud-Plédran. The very positive team-spirit existing in this lab is definitely for something in the impressive scientific output of these last years. Considering the new sample source that is getting installed, and the very talented young people that are taking over, I have very good reasons to bet on the future of polariton physics at EPFL, and more generally, on the emerging field of “polaritronics” [152].

Bibliography

- [1] Weisbuch, C., Nishioka, M., Ishikawa, A. & Arakawa, Y. Observation of the coupled exciton-photon mode splitting in a semiconductor quantum microcavity. *Physical Review Letters* **69**, 3314 (1992).
- [2] Savona, V., Piermarocchi, C., Quattropani, A., Schwendimann, P. & Tassone, F. Optical properties of microcavity polaritons. *Phase Transitions* **68**, 169–279 (1999).
- [3] Ciuti, C., Schwendimann, P., Deveaud, B. & Quattropani, A. Theory of the angle-resonant polariton amplifier. *Physical Review B* **62**, R4825 (2000).
- [4] Savvidis, P. G. *et al.* Angle-Resonant stimulated polariton amplifier. *Physical Review Letters* **84**, 1547 (2000).
- [5] Saba, M. *et al.* High-temperature ultrafast polariton parametric amplification in semiconductor microcavities. *Nature* **414**, 731–735 (2001).
- [6] Baas, A., Karr, J., Eleuch, H. & Giacobino, E. Optical bistability in semiconductor microcavities. *Physical Review A* **69** (2004).
- [7] Dang, L. S., Heger, D., André, R., Boeuf, F. & Romestain, R. Stimulation of polariton photoluminescence in semiconductor microcavity. *Physical Review Letters* **81**, 3920 (1998).
- [8] Senellart, P. & Bloch, J. Nonlinear emission of microcavity polaritons in the low density regime. *Physical Review Letters* **82**, 1233 (1999).
- [9] Kasprzak, J. *et al.* Bose-Einstein condensation of exciton polaritons. *Nature* **443**, 409–414 (2006).
- [10] Lagoudakis, K. G. *et al.* Quantized vortices in an exciton-polariton condensate. *Nature Physics* **4**, 706–710 (2008).
- [11] Lagoudakis, K. G. *et al.* Observation of Half-Quantum vortices in an Exciton-Polariton condensate. *Science* **326**, 974–976 (2009).
- [12] Lagoudakis, K. G., Pietka, B., Wouters, M., André, R. & Deveaud-Plédran, B. Coherent oscillations in an Exciton-Polariton josephson junction. *Physical Review Letters* **105**, 120403 (2010).

- [13] Baas, A., Karr, J. P., Romanelli, M., Bramati, A. & Giacobino, E. Quantum degeneracy of microcavity polaritons. *Physical Review Letters* **96**, 176401 (2006).
- [14] Ciuti, C. & Carusotto, I. Quantum fluid effects and parametric instabilities in microcavities. *Physica status solidi (b)* **242**, 2224–2245 (2005).
- [15] Carusotto, I. & Ciuti, C. Probing microcavity polariton superfluidity through resonant rayleigh scattering. *Physical Review Letters* **93** (2004).
- [16] Amo, A. *et al.* Superfluidity of polaritons in semiconductor microcavities. *Nature Physics* **5**, 805–810 (2009).
- [17] Verger, A., Ciuti, C. & Carusotto, I. Polariton quantum blockade in a photonic dot. *Physical Review B* **73**, 193306 (2006).
- [18] Liew, T. C. H. & Savona, V. Single photons from coupled quantum modes. *Physical Review Letters* **104**, 183601 (2010).
- [19] Liew, T. C. H., Kavokin, A. V. & Shelykh, I. A. Optical circuits based on polariton neurons in semiconductor microcavities. *Physical Review Letters* **101**, 016402 (2008).
- [20] Johne, R., Shelykh, I. A., Solnyshkov, D. D. & Malpuech, G. Polaritonic analogue of Datta and Das spin transistor. *Physical Review B* **81**, 125327 (2010).
- [21] Bloch, J. *et al.* Strong-coupling regime in pillar semiconductor microcavities. *Superlattices and Microstructures* **22**, 371–374 (1997).
- [22] Bajoni, D. *et al.* Polariton laser using single micropillar GaAs-GaAlAs semiconductor cavities. *Physical Review Letters* **100** (2008).
- [23] El Daïf, O. *et al.* Polariton quantum boxes in semiconductor microcavities. *Applied Physics Letters* **88**, 061105 (2006).
- [24] Paraïso, T. K., Wouters, M., Léger, Y., Morier-Genoud, F. & Deveaud-Plédran, B. Multistability of a coherent spin ensemble in a semiconductor microcavity. *Nature Materials* **9**, 655–660 (2010).
- [25] Maan, J. C., Belle, G., Fasolino, A., Altarelli, M. & Ploog, K. Magneto-optical determination of exciton binding energy in $GaAs - Ga_{1-x}Al_xAs$ quantum wells. *Physical Review B* **30**, 2253 (1984).
- [26] Porras, D., Ciuti, C., Baumberg, J. J. & Tejedor, C. Polariton dynamics and Bose-Einstein condensation in semiconductor microcavities. *Physical Review B* **66**, 085304 (2002).
- [27] Christmann, G., Butté, R., Feltin, E., Carlin, J. & Grandjean, N. Room temperature polariton lasing in a GaN/AlGaN multiple quantum well microcavity. *Applied Physics Letters* **93**, 051102 (2008).

- [28] Shimada, R., Xie, J., Avrutin, V., Özgür, U. & Morkoç, H. Cavity polaritons in ZnO-based hybrid microcavities. *Applied Physics Letters* **92**, 011127–011127–3 (2008).
- [29] Kawase, T., Komura, S., Miyazaki, K., Kim, D. & Nakayama, M. Characteristics of exciton polaritons in a ZnO microcavity. *Physica E: Low-dimensional Systems and Nanostructures* **42**, 2567 – 2570 (2010). 14th International Conference on Modulated Semiconductor Structures.
- [30] Lidzey, D. G. *et al.* Strong exciton-photon coupling in an organic semiconductor microcavity. *Nature* **395**, 53–55 (1998).
- [31] Rocca, G. C. L. Organic photonics: Polariton lasing. *Nature Photonics* **4**, 343–345 (2010).
- [32] Tsintzos, S. I., Pelekanos, N. T., Konstantinidis, G., Hatzopoulos, Z. & Savvidis, P. G. A GaAs polariton light-emitting diode operating near room temperature. *Nature* **453**, 372–375 (2008).
- [33] Bajoni, D. *et al.* Polariton light-emitting diode in a GaAs-based microcavity. *Physical Review B* **77**, 113303 (2008).
- [34] Bajoni, D. *et al.* Optical bistability in a GaAs-Based polariton diode. *Physical Review Letters* **101** (2008).
- [35] Chow, W. W., Koch, S. W. & Sargent III, M. *Semiconductor-laser physics* (Springer-Verlag, Berlin, New York, 1994).
- [36] Bastard, G., Mendez, E. E., Chang, L. L. & Esaki, L. Exciton binding energy in quantum wells. *Physical Review B* **26**, 1974 (1982).
- [37] Mathieu, H., Lefebvre, P. & Christol, P. Simple analytical method for calculating exciton binding energies in semiconductor quantum wells. *Physical Review B* **46**, 4092 (1992).
- [38] Andreani, L. C., Tassone, F. & Bassani, F. Radiative lifetime of free excitons in quantum wells. *Solid State Communications* **77**, 641–645 (1991).
- [39] Stanley, R. P., Houdré, R., Oesterle, U., Ilegems, M. & Weisbuch, C. Impurity modes in one-dimensional periodic systems: The transition from photonic band gaps to microcavities. *Physical Review A* **48**, 2246 (1993).
- [40] Gurioli, M. *et al.* Experimental study of disorder in a semiconductor microcavity. *Physical Review B* **64**, 165309 (2001).
- [41] Houdré, R. *et al.* Measurement of Cavity-Polariton dispersion curve from Angle-Resolved photoluminescence experiments. *Physical Review Letters* **73**, 2043 (1994).
- [42] Hopfield, J. J. Theory of the contribution of excitons to the complex dielectric constant of crystals. *Physical Review* **112**, 1555 (1958).

- [43] Yamamoto, Y., Tassone, F. & Cao, H. *Semiconductor cavity quantum electrodynamics* (Springer, Berlin, New York, 2000).
- [44] Ciuti, C., Savona, V., Piermarocchi, C., Quattropani, A. & Schwendimann, P. Role of the exchange of carriers in elastic exciton-exciton scattering in quantum wells. *Physical Review B* **58**, 7926 (1998).
- [45] Ciuti, C. *Nonlinear dynamics of excitons and photons in semiconductor planar structures*. Ph.D. thesis, EPFL, Lausanne (2001).
- [46] Houdré, R. *et al.* Saturation of the strong-coupling regime in a semiconductor microcavity: Free-carrier bleaching of cavity polaritons. *Physical Review B* **52**, 7810 (1995).
- [47] Rochat, G. *et al.* Excitonic bloch equations for a two-dimensional system of interacting excitons. *Physical Review B* **61**, 13856 (2000).
- [48] Ciuti, C., Schwendimann, P. & Quattropani, A. Theory of polariton parametric interactions in semiconductor microcavities. *Semiconductor Science and Technology* **18**, S279 (2003).
- [49] Vladimirova, M. *et al.* Polariton-polariton interaction constants in microcavities. *Physical Review B* **82**, 075301 (2010).
- [50] Deveaud, B. (ed.) *The physics of semiconductor microcavities: from fundamentals to nanoscale devices* (Wiley-VCH, 2007).
- [51] Baas, A. *et al.* Synchronized and desynchronized phases of Exciton-Polariton condensates in the presence of disorder. *Physical Review Letters* **100**, 170401 (2008).
- [52] Krizhanovskii, D. N. *et al.* Coexisting nonequilibrium condensates with long-range spatial coherence in semiconductor microcavities. *Physical Review B* **80**, 045317 (2009).
- [53] Balili, R., Hartwell, V., Snoke, D., Pfeiffer, L. & West, K. Bose-einstein condensation of microcavity polaritons in a trap. *Science* **316**, 1007–1010 (2007).
- [54] Lai, C. *et al.* Coherent zero-state and p-state in an exciton-polariton condensate array. *Nature* **450**, 529 (2007).
- [55] Sarchi, D., Carusotto, I., Wouters, M. & Savona, V. Coherent dynamics and parametric instabilities of microcavity polaritons in double-well systems. *Physical Review B* **77**, 125324 (2008).
- [56] Carusotto, I. *et al.* Fermionized photons in an array of driven dissipative nonlinear cavities. *Physical Review Letters* **103** (2009).
- [57] Wertz, E. *et al.* Spontaneous formation and optical manipulation of extended polariton condensates. *Nature Physics* **6**, 860–864 (2010).

- [58] Portolan, S., Hauke, P. & Savona, V. Parametric photoluminescence of spatially confined polaritons in patterned microcavities. *Physica status solidi (b)* **245**, 1089–1092 (2008).
- [59] El Daif, O., Baas, A., Deveaud-Plédran, B. & Morier-Genoud, F. *Micro optical parametric oscillator for use in e.g. quantum cryptography applications, has semiconductor microcavity configured to spatially localize polariton and quantized polariton levels to effect optical parametric oscillation*. US patent: US2007177253-A1 (2007).
- [60] Ciuti, C., Morier-Genoud, F. & Deveaud-Plédran, B. *Micro-cavity for optical telecommunication device, comprises two Bragg reflectors separated by at least one semiconductor layer*. US patent: US2007007507-A1 (2007).
- [61] Sanvitto, D. *et al.* Observation of ultrahigh quality factor in a semiconductor microcavity. *Applied Physics Letters* **86**, 191109 (2005).
- [62] Dasbach, G., Schwab, M., Bayer, M. & Forchel, A. Parametric polariton scattering in microresonators with three-dimensional optical confinement. *Physical Review B* **64**, 201309 (2001).
- [63] Ferrier, L. *et al.* Polariton parametric oscillation in a single micropillar cavity. *Applied Physics Letters* **97**, 031105 (2010).
- [64] Kim, N. *et al.* GaAs microcavity exciton-polaritons in a trap. *Physica status solidi (b)* **245**, 1076–1080 (2008).
- [65] Balili, R., Snoke, D., Pfeiffer, L. & West, K. Actively tuned and spatially trapped polaritons. *Applied Physics Letters* **88** (2006).
- [66] Cerda-Méndez, E. A. *et al.* Polariton condensation in dynamic acoustic lattices. *Physical Review Letters* **105**, 116402 (2010).
- [67] El Daïf, O. *0D microcavity polaritons*. Ph.D. thesis, EPFL, Lausanne (2007).
- [68] Baas, A. *et al.* Zero dimensional exciton-polaritons. *Physica Status Solidi (b)* **243**, 2311–2316 (2006).
- [69] Kaitouni, R. I. *et al.* Engineering the spatial confinement of exciton polaritons in semiconductors. *Physical Review B* **74**, 155311 (2006).
- [70] Lugan, P., Sarchi, D. & Savona, V. Theory of trapped polaritons in patterned microcavities. *Physica status solidi (c)* **3**, 2428–2431 (2006).
- [71] El Daïf, O. *et al.* Nonlinear relaxation of zero-dimension-trapped microcavity polaritons. *Applied Physics Letters* **92**, 081910 (2008).
- [72] Nardin, G. *et al.* Resonant nonlinear studies of trapped 0D-microcavity polaritons. *Physica status solidi (c)* **5**, 2437–2440 (2008).
- [73] Paraïso, T. K. *et al.* Enhancement of microcavity polariton relaxation under confinement. *Physical Review B* **79**, 045319 (2009).

- [74] Marzin, J.-Y. & Gérard, J.-M. Experimental probing of quantum-well eigenstates. *Physical Review Letters* **62**, 2172 (1989).
- [75] Pechtl, G. *et al.* Zeeman mapping of probability densities in square quantum wells using magnetic probes. *Physical Review B* **61**, 15617 (2000).
- [76] Crommie, M. F., Lutz, C. P. & Eigler, D. M. Confinement of electrons to quantum corrals on a metal surface. *Science* **262**, 218–220 (1993).
- [77] Bürgi, L., Jeandupeux, O., Hirstein, A., Brune, H. & Kern, K. Confinement of surface state electrons in Fabry-Pérot resonators. *Physical Review Letters* **81**, 5370 (1998).
- [78] Nardin, G. *et al.* Probability density optical tomography of confined quasiparticles in a semiconductor microcavity. *Applied Physics Letters* **94**, 181103 (2009).
- [79] Nardin, G. *et al.* Probability density tomography of microcavity polaritons confined in cylindrical traps of various sizes. *Superlattices and Microstructures* **47**, 207–212 (2010).
- [80] Leyronas, X. & Combescot, M. Quantum wells, wires and dots with finite barrier: analytical expressions for the bound states. *Solid State Communications* **119**, 631–635 (2001).
- [81] Gutiérrez-Vega, J. C., Iturbe-Castillo, M. D. & Chávez-Cerda, S. Alternative formulation for invariant optical fields: Mathieu beams. *Optics Letters* **25**, 1493–1495 (2000).
- [82] Gutiérrez-Vega, J. *et al.* Experimental demonstration of optical Mathieu beams. *Optics Communications* **195**, 35–40 (2001).
- [83] Bandres, M. A. & Gutiérrez-Vega, J. Ince Gaussian beams. *Optics Letters* **29**, 144–146 (2004).
- [84] Schwarz, U. T., Bandres, M. A. & Gutiérrez-Vega, J. C. Observation of Ince-Gaussian modes in stable resonators. *Optics Letters* **29**, 1870–1872 (2004).
- [85] Nardin, G., Léger, Y., Pietka, B., Morier-Genoud, F. & Deveaud-Plédran, B. Phase-resolved imaging of confined exciton-polariton wave functions in elliptical traps. *Physical Review B* **82**, 045304 (2010).
- [86] Cerna, R. *et al.* Coherent optical control of the wave function of zero-dimensional exciton polaritons. *Physical Review B* **80**, 121309(R) (2009).
- [87] Kreis, T. *Handbook of holographic interferometry : optical and digital methods* (Wiley-VCH, 2004).
- [88] Mathieu, E. Mémoire sur le mouvement vibratoire d’une membrane de forme elliptique. *Journal de Mathématiques Pures et Appliquées* **13**, 137–203 (1868).

- [89] Chen, G., Morris, P. J. & Zhou, J. Visualization of special eigenmode shapes of a vibrating elliptical membrane. *SIAM Review* **36**, 453 (1994).
- [90] Gutiérrez-Vega, J., Chávez-Cerda, S. & Rodríguez-Dagnino, R. Free oscillations in an elliptic membrane. *Revista Mexicana de Física* **45**, 613–622 (1999).
- [91] Gutiérrez-Vega, J. C., Rodríguez-Dagnino, R. M., Meneses-Nava, M. A. & Chávez-Cerda, S. Mathieu functions, a visual approach. *American Journal of Physics* **71**, 233 (2003).
- [92] Liew, T. C. H., Rubo, Y. G. & Kavokin, A. V. Generation and dynamics of vortex lattices in coherent Exciton-Polariton fields. *Physical Review Letters* **101**, 187401 (2008).
- [93] Fraser, M., Roumpos, G. & Yamamoto, Y. Vortex-antivortex pair dynamics in an exciton-polariton condensate. *New Journal of Physics* **11** (2009).
- [94] Krizhanovskii, D. *et al.* Effect of interactions on vortices in a nonequilibrium polariton condensate. *Physical Review Letters* **104** (2010).
- [95] Gorbach, A. V., Hartley, R. & Skryabin, D. V. Vortex lattices in coherently pumped polariton microcavities. *Physical Review Letters* **104**, 213903 (2010).
- [96] Sanvitto, D. *et al.* Persistent currents and quantized vortices in a polariton superfluid. *Nature Physics* **6**, 527–533 (2010).
- [97] Roumpos, G. *et al.* Single vortex-antivortex pair in an exciton-polariton condensate. *Nature Physics* (**advance online publication**) (2010).
- [98] Nardin, G. *et al.* Selective photoexcitation of confined exciton-polariton vortices. *Physical Review B* **82**, 073303 (2010).
- [99] Brambilla, M. *et al.* Transverse laser patterns. I. Phase singularity crystals. *Physical Review A* **43**, 5090 (1991).
- [100] Chen, Y. F. & Lan, Y. P. Transverse pattern formation of optical vortices in a microchip laser with a large fresnel number. *Physical Review A* **65**, 013802 (2001).
- [101] De Colstoun, F. B. *et al.* Transverse modes, vortices and vertical-cavity surface-emitting lasers. *Chaos, Solitons & Fractals* **4**, 1575–1596 (1994).
- [102] Epler, J. E. *et al.* Mode behavior and high resolution spectra of circularly-symmetric GaAs-AlGaAs air-post vertical cavity surface emitting lasers. *Applied Physics Letters* **69**, 722 (1996).
- [103] Degen, C., Elsässer, W. & Fischer, I. Transverse modes in oxide confined VCSELs: influence of pump profile, spatial hole burning, and thermal effects. *Optics Express* **5**, 38–47 (1999).
- [104] Padgett, M. An experiment to observe the intensity and phase structure of Laguerre-Gaussian laser modes. *American Journal of Physics* **64**, 77 (1996).

- [105] Padgett, M. J. & Courtial, J. Poincaré-sphere equivalent for light beams containing orbital angular momentum. *Optics Letters* **24**, 430–432 (1999).
- [106] Langbein, W. *et al.* Polarization beats in ballistic propagation of exciton-polaritons in microcavities. *Physical Review B* **75**, 075323 (2007).
- [107] Cerna, R. *et al.* Spatial dynamics of confined semiconductor microcavity polaritons. *Physical Review B* **81**, 113306 (2010).
- [108] Nardin, G. *et al.* Dynamics of long-range ordering in an exciton-polariton condensate. *Phys. Rev. Lett.* **103**, 256402 (2009).
- [109] Lagoudakis, K. G. *et al.* Formation and migration of vortices in polariton condensates. *arXiv:1009.5907* (2010).
- [110] Frisch, T., Pomeau, Y. & Rica, S. Transition to dissipation in a model of superflow. *Physical Review Letters* **69**, 1644 (1992).
- [111] Winiecki, T., McCann, J. F. & Adams, C. S. Pressure drag in linear and nonlinear quantum fluids. *Physical Review Letters* **82**, 5186 (1999).
- [112] Winiecki, T., Jackson, B., McCann, J. & Adams, C. Vortex shedding and drag in dilute Bose-Einstein condensates. *Journal of Physics B-Atomic Molecular and Optical Physics* **33**, 4069–4078 (2000).
- [113] Barenghi, C., Donnelly, R. & Vinen, W. (eds.) *Quantized vortex dynamics and superfluid turbulence* (Springer, Berlin, New York, 2001).
- [114] Aftalion, A., Du, Q. & Pomeau, Y. Dissipative flow and vortex shedding in the painlevé boundary layer of a Bose-Einstein condensate. *Physical Review Letters* **91**, 090407 (2003).
- [115] Sasaki, K., Suzuki, N. & Saito, H. Bénard-von Kármán vortex street in a Bose-Einstein condensate. *Physical Review Letters* **104**, 150404 (2010).
- [116] Mironov, V. A., Smirnov, A. I. & Smirnov, L. A. Structure of vortex shedding past potential barriers moving in a Bose-Einstein condensate. *Journal of Experimental and Theoretical Physics* **110**, 877–889 (2010).
- [117] Inouye, S. *et al.* Observation of vortex phase singularities in Bose-Einstein condensates. *Physical Review Letters* **87**, 080402 (2001).
- [118] Raman, C., Abo-Shaeer, J. R., Vogels, J. M., Xu, K. & Ketterle, W. Vortex nucleation in a stirred Bose-Einstein condensate. *Physical Review Letters* **87**, 210402 (2001).
- [119] Neely, T. W., Samson, E. C., Bradley, A. S., Davis, M. J. & Anderson, B. P. Observation of vortex dipoles in an oblate Bose-Einstein condensate. *Physical Review Letters* **104**, 160401 (2010).
- [120] Bergé, P., Pomeau, Y. & Vidal, C. *Order within Chaos : Towards a Deterministic Approach to Turbulence* (John Wiley, New York, 1984).

- [121] Ruchonnet, N. *Multiscale Computational Methodology Applied to Hydroacoustic Resonance in Cavitating Pipe Flow*. Ph.D. thesis, EPFL, Lausanne (2010).
- [122] Donnelly, R. *Quantized Vortices in Helium II* (Cambridge Univ. Press, Cambridge, 1991).
- [123] Pitaevskii, L. & Stringari, S. *Bose-Einstein condensation* (Clarendon Press, Oxford, New York, 2003).
- [124] Raman, C. *et al.* Evidence for a critical velocity in a Bose-Einstein condensed gas. *Physical Review Letters* **83**, 2502 (1999).
- [125] Onofrio, R. *et al.* Observation of superfluid flow in a Bose-Einstein condensed gas. *Physical Review Letters* **85**, 2228 (2000).
- [126] Carusotto, I., Hu, S. X., Collins, L. A. & Smerzi, A. Bogoliubov-Čerenkov radiation in a Bose-Einstein condensate flowing against an obstacle. *Physical Review Letters* **97**, 260403 (2006).
- [127] Madison, K. W., Chevy, F., Wohlleben, W. & Dalibard, J. Vortex formation in a stirred Bose-Einstein condensate. *Physical Review Letters* **84**, 806 (2000).
- [128] Landau, L. Theory of the superfluidity of helium II. *Physical Review* **60**, 356 (1941).
- [129] Amo, A. *et al.* Collective fluid dynamics of a polariton condensate in a semiconductor microcavity. *Nature* **457**, 291–295 (2009).
- [130] Bolda, E. L., Chiao, R. Y. & Zurek, W. H. Dissipative optical flow in a nonlinear Fabry-Pérot cavity. *Physical Review Letters* **86**, 416 (2001).
- [131] Pigeon, S., Carusotto, I. & Ciuti, C. Hydrodynamic nucleation of vortices and solitons in a resonantly excited polariton superfluid. *arXiv:1006.4755* (2010).
- [132] Amo, A. *et al.* Light engineering of the polariton landscape in semiconductor microcavities. *Physical Review B* **82**, 081301 (2010).
- [133] Sermage, B., Malpuech, G., Kavokin, A. V. & Thierry-Mieg, V. Polariton acceleration in a microcavity wedge. *Physical Review B* **64**, 081303 (2001).
- [134] Karr, J. P., Baas, A., Houdré, R. & Jacobino, E. Squeezing in semiconductor microcavities in the strong-coupling regime. *Physical Review A* **69**, 031802 (2004).
- [135] Bamba, M., Pigeon, S. & Ciuti, C. Quantum squeezing generation versus photon localization in a disordered planar microcavity. *Physical Review Letters* **104**, 213604 (2010).
- [136] Hartmann, M. J., Brandao, F. G. S. L. & Plenio, M. B. Strongly interacting polaritons in coupled arrays of cavities. *Nature Physics* **2**, 849–855 (2006).

- [137] Greiner, M., Mandel, O., Esslinger, T., Hansch, T. W. & Bloch, I. Quantum phase transition from a superfluid to a Mott insulator in a gas of ultracold atoms. *Nature* **415**, 39–44 (2002).
- [138] Small, E., Pugatch, R. & Silberberg, Y. Berezinskii-Kosterlitz-Thouless crossover in a photonic lattice. *Physical Review A* **83**, 013806 (2011).
- [139] Amo A. *et al.* Exciton-polariton spin switches. *Nature Photonics* **4**, 361–366 (2010).
- [140] Wertz, E. *et al.* Spontaneous formation of a polariton condensate in a planar GaAs microcavity. *Applied Physics Letters* **95**, 051108 (2009).
- [141] Zollner, S. Optical constants and critical-point parameters of GaAs from 0.73 to 6.60 eV. *Journal of Applied Physics* **90**, 515–517 (2001).
- [142] Paraïso, T. *Dynamics of Interactions of Confined Microcavity Polaritons*. Ph.D. thesis, EPFL, Lausanne (2010).
- [143] Iakovlev, V. *et al.* High-performance single-mode vcsels in the 1310-nm waveband. *Photonics Technology Letters, IEEE* **17**, 947–949 (2005).
- [144] Katsuaki, T., Fontcuberta i Morral, A., Atwater, H. A., Aiken, D. & Wanlass, M. Direct-bonded GaAs/InGaAs tandem solar cell. *Applied Physics Letters* **89**, 102106–102106–3 (2006).
- [145] Akatsu, T., Plössl, A., Stenzel, H. & Gösele, U. GaAs wafer bonding by atomic hydrogen surface cleaning. *Journal of Applied Physics* **86**, 7146–7150 (1999).
- [146] Caire-Remonnay, B. *Polaritons de microcavités semiconductrices - Rapport de stage*. Master’s thesis, EPFL, Lausanne (2009).
- [147] Nardin, G. Report on the first test for wafer bonding of a λ cavity at 850nm with etched patterns (2007). (available in the ring binder on sample characterizations in the office cupboard).
- [148] Wouters, M. & Carusotto, I. Excitations in a nonequilibrium Bose-Einstein condensate of exciton polaritons. *Physical Review Letters* **99**, 140402 (2007).
- [149] Sarchi, D. & Savona, V. Long-range order in the Bose-Einstein condensation of polaritons. *Physical Review B* **75**, 115326 (2007).
- [150] del Valle, E. *et al.* Dynamics of the formation and decay of coherence in a polariton condensate. *Physical Review Letters* **103**, 096404 (2009).
- [151] Shelykh, I. A., Pavlovic, G., Solnyshkov, D. D. & Malpuech, G. Proposal for a mesoscopic optical Berry-Phase interferometer. *Physical Review Letters* **102**, 046407 (2009).
- [152] Deveaud-Plédran, B. Solid-state physics: Polaritronics in view. *Nature* **453**, 297–298 (2008).

Remerciements

Je remercie chaleureusement toutes les personnes qui m'ont encadré et soutenu durant ces 4 années de thèse. À commencer par mon directeur de thèse, Benoît Deveaud-Plédran, dont les compétences, le soutien sans faille et l'enthousiasme contagieux m'ont permis de mener à bien ce travail. Un grand merci à Ounsi El Daïf, avec qui j'ai eu le plaisir d'apprendre les rudiments de l'optique expérimentale, et qui a aussi grandement contribué à la fabrication de l'échantillon exceptionnel sur lequel j'ai réalisé les expériences de cette thèse. Merci aussi bien sûr à François Morier-Genoud, qui est non seulement le croisseur de cet échantillon, mais qui m'a aussi soutenu de ses précieux conseils tout au long de ces années. Je remercie aussi Maxime Richard et Augustin Baas, qui ont encadré mon travail pendant les premières années de cette thèse, et m'ont inculqué les bases de l'optique quantique. Un merci spécial à Yoan Léger et Barbara Pietka, qui m'ont encadré pendant une grande partie de ce travail, et m'ont soutenu au quotidien, répondant inlassablement à mes innombrables questions, relisant mes manuscrits. Sans leur soutien, leur expertise et leurs idées novatrices, ce travail de thèse ne serait pas devenu ce qu'il est devenu. Je remercie aussi chaleureusement tous mes collègues doctorants et amis du groupe: Konstantinos Lagoudakis, Taofiq Paraïso, Roland Cerna, Verena Kohnle, Francesco Manni et Gabriele Grosso, qui ont tous contribué de près ou de loin à cette thèse, de par les nombreuses discussions scientifiques et inestimables coups de main au labo, et plus généralement à l'exceptionnelle ambiance de travail qui règne au LOEQ. Un grand merci aussi aux théoriciens de l'ITP: Vincenzo Savona, Davide Sarchi, Michiel Wouters et Tim Liew, qui ont su de par leurs idées et leurs modèles stimuler la créativité expérimentale de notre groupe. Merci à Marcia Portella-Oberli, ainsi qu'à Marc-André Dupertuis, Romuald Houdré et Raphaël Butté, avec qui j'ai pu avoir de nombreuses discussions fructueuses. Je suis aussi reconnaissant envers les étudiants dont j'ai eu le plaisir d'encadrer ou de co-encadrer les projets: Benjamin Gallinet, Karin Söderström et Boris Caire-Remonnay. Interagir avec eux m'a beaucoup appris. Merci au staff administratif et technique de l'institut: Claire-Lyse Rouiller, Nicolas Leiser, Yoan et Damien Trolliet, Maxime Marendaz, et Roger Rochat, pour leur efficacité et leur disponibilité. Je remercie grandement les membres de mon jury de thèse: les professeurs Cristiano Ciuti, Steven Cundiff, Jérôme Faist et Olivier Martin, pour avoir accepté de juger mon travail, pour leur lecture attentive et leurs commentaires fructueux. Je remercie profondément toute ma famille, qui m'a toujours soutenu sans réserve dans tout ce que j'ai entrepris. Merci aussi à tous mes amis, avec qui j'ai passé de très bons moments pendant toutes ces années. Finalement, un énorme merci à Vanessa pour avoir toujours été à mes côtés et vécu avec moi au jour le jour les événements riches

en émotions qui rythment la vie d'un doctorant.

Gaël Nardin

Beauregard 3
CH-2400 Le Locle
Switzerland

born on May 17th 1983
Swiss

gael.nardin@gmail.com

++41 79 512 53 44

WORK EXPERIENCE

January 2007 to present

Swiss Institute of Technology (EPFL)

Lausanne, Switzerland

PhD student in the Lab of Quantum Optoelectronics

In the scope of my PhD thesis, I am carrying out experimental research in the field of semiconductor microcavities, with a focus on the phase-resolved imaging of exciton-polariton dynamics.

I have supervised the work of one master student and two semester students.

I am also a teaching assistant for Bachelor and Master classes in Engineering and Physics (30 students)

July - October 2006 (internship)

Laser Zentrum Hannover e.V.

Hannover, Germany

R&D intern

During this internship, I took part in the design, fabrication and testing of an industrial setup for nanostructuring photosensitive polymers.

October 2004

Nouvelle Planète (Swiss NGO)

Burkina Faso

Volunteer

In collaboration with local workers and technicians, I took part in the fabrication of solar water heaters, and in their distribution to remote villages maternity hospitals.

August - September 2004 (internship)

Ismeca Europe Semiconductor SA

La Chaux-de-Fonds, Switzerland

R&D Intern

During this internship, I realized the optical design of a new generation scanner for the quality control of semiconductor devices in a production line.

ACADEMICS

April 2011

PhD in Science – Photonics

Swiss Institute of Technology - Lausanne (EPFL)

✓ Attended a project management course

- 2006 **MSc in Physics**
 Swiss Institute of Technology - Lausanne (EPFL)
 ✓ *Including an exchange year*
 (BTech Eng. Physics, IIT - Indian Institute of Technology,
 New Delhi)
- 2001 **Baccalauréat ès Sciences (Swiss Maturity)**
 Gymnase Cantonal de La Chaux-de-Fonds
 ✓ *Honors*
 ✓ *Maths & Physics student award (Prix Etienne Gilliard 2001)*

SKILLS

- ✓ Working knowledge with
 - Optics: lasers (cw and pulsed), polarization optics, spectroscopy, time-resolved measurements, interferometry
 - Clean room facilities: photolithography, wet etching
 - Vacuum & cryogenics: liquid He and N
- ✓ Scientific writing, oral presentations
- ✓ IT skills:
 - Programming (Matlab, c++, Fortran 90, VB.NET)
 - Data acquisition and processing (Labview, Igor Pro)
 - Results presentation (Latex, Adobe Illustrator, Blender)
- ✓ Contacts with suppliers for purchasing scientific equipments

LANGUAGES

English : Fluent (working language, exchange year in New Delhi, India)
French : Mother tongue // **German** : Good (internship in Hannover, Germany)

HOBBIES

Judo : Black belt - 1st dan, experience of team competition (Swiss B league) and coaching
Traveling, meeting different cultures (more than 30 countries visited so far)

REFERENCE

Prof. Benoît Deveaud-Plédran
Director, Laboratory of Quantum Optoelectronics
EPFL, Switzerland
benoit.deveaud-pledran@epfl.ch
++41 21 693 54 96
++41 21 693 33 55

Publications

Quantum turbulence in a polariton fluid

G. Nardin, G. Grosso, Y. Léger, B. Pietka, F. Morier-Genoud, and B. Deveaud-Plédran

Submitted to *Nature Physics*

Selective photoexcitation of confined exciton-polariton vortices

G. Nardin, K.G. Lagoudakis, B. Pietka, F. Morier-Genoud, Y. Léger, and B. Deveaud-Plédran

Physical Review B, **82**, 073303 (2010).

Phase-resolved imaging of confined exciton-polariton wave functions in elliptical traps

G. Nardin, Y. Léger, B. Pietka, F. Morier-Genoud, and B. Deveaud-Plédran

Physical Review B, **82**, 045304 (2010).

Probability density tomography of microcavity polaritons confined in cylindrical traps of various sizes

G. Nardin, R. Cerna, T. K. Paraïso, B. Pietka, Y. Léger, O. El Daif, F. Morier-Genoud, and B. Deveaud-Plédran

Superlattices and Microstructures, **47**, 207-212 (2010).

Dynamics of Long-Range Ordering in an Exciton-Polariton Condensate

G. Nardin, K. G. Lagoudakis, M. Wouters, M. Richard, A. Baas, R. André, Le Si Dang, B. Pietka, and B. Deveaud-Plédran

Physical Review Letters, **103**, 256402 (2009).

Coherent optical control of the wave function of zero dimensional exciton polaritons

R. Cerna, D. Sarchi, T. K. Paraïso, G. Nardin, Y. Léger, M. Richard, B. Pietka, O. El Daif, F. Morier-Genoud, V. Savona, M. T. Portella-Oberli, and B. Deveaud-Plédran

Physical Review B, **80**, 121309(R) (2009).

Probability density optical tomography of confined quasiparticles in a semiconductor microcavity

G. Nardin, T. K. Paraïso, R. Cerna, B. Pietka, Y. Léger, O. El Daif, F. Morier-Genoud, and B. Deveaud-Plédran

Applied Physics Letters, **94**, 181103 (2009).

Enhancement of microcavity polariton relaxation under confinement

T.K. Paraïso, D. Sarchi, G. Nardin, R. Cerna, Y. Leger, B. Pietka, M. Richard, O. El Daïf, F. Morier-Genoud, V. Savona, and B. Deveaud-Plédran

Physical Review B, **79**, 045319 (2009).

Resonant nonlinear studies of trapped 0D-microcavity polaritons

G. Nardin, O. El Daïf, T.K. Paraïso, A. Baas, M. Richard, F. Morier-Genoud, and B. Deveaud

Physica status solidi (c), **5**, 2437-2440 (2008).

Nonlinear relaxation of zero-dimension-trapped microcavity polaritons

O. El Daif, G. Nardin, T.K. Paraïso, A. Baas, M. Richard, J.-P. Brantut, T. Guillet, F. Morier-Genoud, and B. Deveaud-Plédran

Applied Physics Letters, **92**, 0819101-0819103 (2008).

Zero dimensional exciton-polaritons

A. Baas, O. El Daïf, M. Richard, J.-P. Brantut, G. Nardin, R.I. Kaitouni, T. Guillet, V. Savona, J.L. Staehli, F. Morier-Genoud, B. Deveaun

Physica status solidi (b), **243**, 2311-2316 (2006).

Oral presentations

"Quantum turbulence in a polariton fluid"

5th International Conference on Spontaneous Coherence in Excitonic Systems (ICSCE-5)

Lausanne, Switzerland, February 7-11, 2011.

"Quantum turbulence in semiconductor microcavities"

Ultrafast Phenomena in Semiconductors and Nanostructure Materials XV – SPIE Photonics West 2011

San Francisco, USA, January 22-27, 2010.

"Selective photoexcitation of quantized exciton-polariton vortices in a patterned GaAs microcavity"

30th International Conference on the Physics of Semiconductors (ICPS 2010)

Seoul, Korea, July 25-30, 2010.

"Selective photoexcitation of quantized exciton-polariton vortices"

16th International Conference on Superlattices, Nanostructures and Nanodevices (ICSNN-2010)

Beijing, China, July 18-23, 2010.

"Probability density tomography of confined exciton-polaritons"

Joint Swiss-Austrian Physical Societies Meeting

Innsbruck, Austria, September 2-4, 2009.